

Design optimization of splitter blades for rocket engine turbopump

Torre, Francesco; Konno, Shinichi; Pini, Matteo; Kawata, Y.; Lettieri, Claudio

DOI

[10.1115/GT2018-75192](https://doi.org/10.1115/GT2018-75192)

Publication date

2018

Document Version

Final published version

Published in

ASME 2018 Turbo Expo Turbomachinery Technical Conference & Exposition

Citation (APA)

Torre, F., Konno, S., Pini, M., Kawata, Y., & Lettieri, C. (2018). Design optimization of splitter blades for rocket engine turbopump. In *ASME 2018 Turbo Expo Turbomachinery Technical Conference & Exposition: June 11-15, 2018, Oslo, Norway* Article GT2018-75192 <https://doi.org/10.1115/GT2018-75192>

Important note

To cite this publication, please use the final published version (if applicable).
Please check the document version above.

Copyright

Other than for strictly personal use, it is not permitted to download, forward or distribute the text or part of it, without the consent of the author(s) and/or copyright holder(s), unless the work is under an open content license such as Creative Commons.

Takedown policy

Please contact us and provide details if you believe this document breaches copyrights.
We will remove access to the work immediately and investigate your claim.

Green Open Access added to TU Delft Institutional Repository

'You share, we take care!' - Taverne project

<https://www.openaccess.nl/en/you-share-we-take-care>

Otherwise as indicated in the copyright section: the publisher is the copyright holder of this work and the author uses the Dutch legislation to make this work public.

F. Torre

DESIGN OPTIMIZATION OF SPLITTER BLADES FOR ROCKET ENGINE TURBOPUMP

DESIGN OPTIMIZATION OF SPLITTER BLADES FOR ROCKET ENGINE TURBOPUMP

By

Francesco Torre

in partial fulfilment of the requirements for the degree of

Master of Science
in Aerospace Engineering

at the Delft University of Technology,
to be defended publicly on Thursday February 1, 2018 at 9:30 AM.

Supervisor:

Dr. C. Lettieri
Dr. M. Pini

Thesis committee:

Prof. dr. ir. P. Colonna
Dr. P. Cervone

An electronic version of this thesis is available at <http://repository.tudelft.nl/>.

Acknowledgements

The last twelve months have been an amazing period for me, above every expectation from many points of view. I deepened my knowledge on CFD simulations, cavitation, rocket engines and turbopumps. I had the chance to conduct experiments, I was able to discover an astonishing culture and a wonderful country and to make new friends. The three months spent in Osaka really enriched me both professionally and personally, making this thesis experience the best way to end a tough but exciting and full of learning two years period in Delft.

There are many people I have to thank for this invaluable experience. First my supervisors. Prof. Lettieri not only gave me this opportunity but has always been a source of learning, advices, support and motivation. Prof. Pini constantly helped and supported me throughout the project with precious suggestions. Thank you very much indeed to you both, I will always be grateful.

I would also like to thank Prof. Kawata, who treated me so well during my stay in Japan and was always available to discuss about the project. To all the members of the Fluidmachinery Laboratory of the Osaka Institute of Technology, in particular to Konno-San and Hayashi-San, for the tremendous help they gave me during the experiments and the great memories. *ありがとうございます!*

To Giacomo, my friend and best companion possible during this unforgettable journey, thank you!

To my dear friends in Delft, in particular Marco, Marco, Cristiano, Giorgio and Henrique, in memory of the uncountable days spent in the Library (and its cafeteria), the nights in Rotterdam and The Hague, the trip to Paris and all the other activities not strictly linked to earning ECTS. You enlightened the journey, thank you!

I could not have succeeded without the constant support of my girlfriend Daniela and of my friends from Milan and Siena, always by my side despite the distance.

Lastly, I would like to thank my parents Marco and Giovanna, my sister Chicca and my grandmothers Maria and Sandra for their love and support. The commitment and passion you put in everything you do represent to me a source of inspiration. The only reason why I am here today is because of your example and education.

*Francesco Torre
Delft, January 2018*

Abstract

Turbopumps are used in large-scale liquid rockets to inject the cryogenic propellants into the combustor. The turbopumps operate at high rotational speed, which in turn leads to cavitation at the inlet of the impeller. Cavitation can cause performance issues, instabilities and mechanical damage of the blades.

This thesis presents and validates a shape optimization framework for the design of splitter blades that extends the operative range under cavitation while maintaining the wetted performance. For a target turbopump application, the optimization framework allows for independent changes to the blade angle distributions across the span and to the pitchwise position of the splitter blades while preserving the thickness distributions.

The optimization is conducted with a surrogate-based gradient method. The geometry is optimized at a fixed cavitation number corresponding to a 5% head coefficient drop-off, while constraints are imposed on the wet pump performance. It is found that this approach, coupled with the optimal design points distribution provided by the Design of Experiment method, reduces the computational cost of the optimization process by minimizing the number of multiphase calculations.

The numerical results show that the optimized splitter blades successfully increase the pump operative range by 2.2% and increase the head coefficient by 5.3% compared to the baseline case with non-optimized splitters. These results are corroborated by experiments conducted in a closed-loop water test facility. Several pump geometries are tested through rapid prototyping using additive manufacturing. The experimental data validate the optimization framework, demonstrating a 4.7% increase of pump operative range and a 7.6% increase in head coefficient. The calculations are used to gain insight in the physical mechanisms for the performance improvement. The analysis of the results indicates that the improved performance is due to the optimized position and shape of the splitter blades which increase the pump slip factor.

Contents

Acknowledgements	i
Abstract	iii
Contents	v
List of Figures	vii
List of Tables	x
List of Symbols and Abbreviations	xii
1 Introduction	1
1.1 Background	1
1.2 Research Questions and Goals	2
1.3 Originality of the Work.....	2
1.4 Outline of the Thesis	3
2 Theoretical background	4
2.1 Overview of Turbopump Performance.....	6
2.1.1 Wet Performance.....	6
2.1.2 Theoretical Head and Euler’s Turbine Equation	8
2.1.3 Velocity Triangles.....	9
2.1.4 Cavitation Description	10
2.1.5 Cavitating Performance	11
2.2 Cavitation Mitigation Techniques.....	13
2.2.1 Casing Treatment	13
2.2.2 Leading Edge Shaping.....	13
2.2.3 Inducer	15
2.2.4 Splitter blades.....	15
3 Characterization of the Baseline Geometry	20
4 Optimization Framework	23
4.1 Framework Overview	23
4.1.1 Parametric CAD.....	23
4.1.2 Adaptive Mesher.....	25
4.1.3 Numerical Solver	27
4.1.4 Optimizer	28
4.2 Framework Setup	29
4.2.1 Selection of Design Parameters.....	29
4.2.2 Optimizer Setup.....	31
4.3 Optimization Objectives and Strategy	33
5 Optimized Design Assessment	36
5.1 Optimal Splitter Blade Shape	36
5.2 Experimental Validation.....	38
5.2.1 Test Rig.....	38
5.2.2 Pump Manufacturing.....	39
5.2.3 Validation Results	42
6 Characterization of the Performance Gain	45
6.1 Cavitation analysis	45
6.2 Flow field analysis.....	46
6.3 Influence of the blade outlet angle	54

7	Conclusions and Recommendations	56
7.1	Conclusions	56
7.2	Recommendations for Future Works.....	57
APPENDIX – A	59
Bibliography	69

List of Figures

Figure 2.1: Cutaway of the oxidizer turbopump of the Vulcain 2 engine equipped in the first stage of the Ariane 5 five. The fuel used is LH2, liquid-hydrogen, while LOX, liquid-oxygen, is employed as oxidizer. Courtesy of Avio.	4
Figure 2.2: Simplified flow diagram of SSME (Courtesy Rocketdyne).	5
Figure 2.3: Generic wet performance curve for a pump. [2].....	7
Figure 2.4: Typical example of losses contributions leading from the theoretical head curve, H_{th} , to the real one, H . Plot adapted from [3], where ZLa and ZLe indicate, respectively, the contributions of impeller and the diffuser.	7
Figure 2.5: Velocity triangle at the impeller outlet.	9
Figure 2.6: Types of cavitation occurring in pumps.	10
Figure 2.7: Blade cavity showing the increased blockage at the inlet. Image from [2].....	10
Figure 2.8: Leading edge separation due to off-design flow rates. This condition can be used to explain the detrimental effect of cavity bubbles on performance. In red the throat areas are indicated. [3]	11
Figure 2.9: Qualitative cavitating performance curve of a generic pump. The most important cavitation parameters are indicated.....	12
Figure 2.10: Example of casing treatment extending in the blade tip region. Picture from [4]	13
Figure 2.11: Impact of inducer leading edge on hydraulic performance. Figures from [2]. ...	14
Figure 2.12: CFD results showing the importance of the leading edge shape on cavity size.	14
Figure 2.13: SSME low pressure LOX turbopump inducer. Figure from [2].....	15
Figure 2.14: Inlet area comparison at a given span location. The extension up to the inlet of the middle full-length blade causes a reduced inlet area due to increased blade blockage for the full blades configuration.....	16
Figure 2.15: Contours of vapour fraction and relative velocity streamlines at midspan for the three different cases. Image taken from [8].	17
Figure 2.16: Improvement of cavitating performance as found by Yang in [9]. Conventional here refers to the impeller having only full-length blades whereas compound indicates the pump with splitter blades.....	17
Figure 2.17: Image taken from [17]. Contours of relative velocity and indication of the incidence angle at 144% of design flow rate (on the left side) and at 68% (on the right side). Comparison between impellers with full-length blades (top) and splitters (bottom).	18
Figure 3.1: Exploded view of the pump's components.....	20
Figure 3.2: Pump meridional plane, with the inducer and impeller blades colored in dark grey.	21
Figure 3.3: Comparison between the simplified outlet section, a), and the complete volute, b).	21
Figure 3.4: Sketches of the volute used in the simulations. On the left meridional plane view, to underline the absence of the leakage flow, on the right the complete volute as seen from the -z axis direction.	22
Figure 3.5: Cavitating performance of the full-length blade impeller (Case 1) and the splattered one (Case 2, the baseline of this thesis) from the OIT research. Figure from [21].	22
Figure 4.1: Block diagram of the optimization framework. Courtesy of Giacomo Mingardo..	23
Figure 4.2: BladeGen window after the pump blades have been specified, showing beta angle and thickness distributions.	24
Figure 4.3: Comparison of the reconstructed blade profiles against the baseline ones. The maximum discrepancy happens at splitter blade leading edge's hub.....	24
Figure 4.4: Details of the inducer tip gap mesh (in red) for one blade created with ICEM. ...	25

Figure 4.5: Topology and mesh at midspan as created by TurboGrid for the baseline pump.	26
Figure 4.6: Mesh convergence study indicates 2.5 million elements are sufficient to capture pump performance	27
Figure 4.7: Illustration of the Bezier curves parametrization. The blade angle distribution is parametrized with three control points of the Bezier curves.....	29
Figure 4.8: The circumferential or pitch position parameter determines the proximity of the splitter to the suction side ($p=1$) or to the pressure side ($p=0$) of the main blade.....	30
Figure 4.9: Example of how the LHS and OSFM differs when creating the design points. The plots show the distribution of design points having two input parameters.....	31
Figure 4.10: Response surface for two parameters of the optimization and the Head coefficient with cavitation. The squares represent the computed output of each design point.	33
Figure 4.11: The optimization of the cavitating performance is done simulating at baseline 5% drop-off σ . The head coefficient is maximized in that condition. It is hypothesized that to increased ψ correspond lower drop-off points (red curve).	34
Figure 4.12: Example of a typical head-capacity curve characterizing the wet performance of a centrifugal impeller.	34
Figure 5.1: Comparison of the hub and shroud profiles of the baseline and optimized splitter blades.	37
Figure 5.2: Scheme of the closed-loop test facility of the OIT.	38
Figure 5.3: Optimized pump as reconstructed by 3D printing at the Osaka Institute of Technology.....	39
Figure 5.4: Definition of the inducer measured dimensions. View a) illustrates the inducer from the inlet, view b) the trailing edge thickness and view c) the hub outlet radius. In place of the radius $R3$ the diameter, $Diam3$, is actually measured.....	40
Figure 5.5: Definition of the dimensions measured in the baseline and optimized impellers. View a) shows the impeller from a side highlighting the outlet section (T2 and T1) whereas b) is a view from the upstream section of the pump.....	41
Figure 5.6: Wet performance comparison between experiments and computations. A constant offset is present between the baseline and optimized design, validating the optimization framework.	42
Figure 5.7: Cavitating performance comparison between experiments and computations. Experimental measurements indicate a larger improvement of operating range than computations.	43
Figure 5.8: Simulated cavitating performance, comparison between optimized and baseline pumps. The head coefficient increase (blue arrow) at the optimized cavitation number generates an extension of the operative range (green arrow).	44
Figure 6.1: Comparison of 1% vapour volume fraction isosurface between baseline and optimized designs.	45
Figure 6.2: Explanation of the circumferential average by mass performed by CFX Inlet to Outlet Turbo Chart. Image from [22].....	46
Figure 6.3: The optimized impeller starts to outperform the baseline impeller starting approximately from the splitter LE.....	47
Figure 6.4: Total pressure distribution along a streamline close to hub. The trend is similar to the streamwise averaged of Figure 5.3.	47
Figure 6.5: Total pressure distribution along a streamline close to shroud. The optimized impeller performs as the baseline one almost throughout the entire passage.	48
Figure 6.6: View from the impeller inlet of the baseline case. Streamlines departing from the leading edge separate from the wall after few fractions of the main blade meridional length.	48
Figure 6.7: View from the impeller inlet of the optimized case. Streamlines departing from the leading edge, smoothly follow the main blade pressure surface.....	49
Figure 6.8: Body forces acting on a particle of fluid at a given point along a streamline. Figure from [3].....	49

Figure 6.9: Secondary flow trajectory in a rotating channel, from [3].	50
Figure 6.10: Streamlines of relative velocity at <i>midspan</i> . Between main blade pressure and splitter suction side, the reduction in flow turning is appreciable.	51
Figure 6.11: Streamlines of relative velocity at <i>20% span</i> . Separation on the pressure side of the main blade is caused by the collapse of the cavity generating from main blade suction side.	51
Figure 6.12: Example of velocity triangle at the impeller outlet, from [3].	52
Figure 6.13: Deviation of streamlines of relative flow from the blade geometry just downstream of the throat (red line). Blade-congruent path is dashed. Figure from [3].	53
Figure 6.14: Spanwise distribution of the averaged circumferential component of the absolute velocity at the impeller trailing edge.	53
Figure 6.15: Reference configuration used for the 1D analysis.	54
Figure 6.16: Spanwise distribution of the circumferential component of the absolute velocity. Comparison between the CFD and the 1D analysis results.	55
Figure 6.17: Schematic representation of the weights of the two contributions to the performance improvement	55

List of Tables

Table 3-1: Overview of the main parameters of the baseline pump impeller.	20
Table 4-1: Parameters variation to obtain the optimal shape	36
Table 4-2: Inducer measurements	40
Table 4-3: Baseline impeller measurements	41
Table 4-4: Optimized impeller measurements	41

List of Symbols and Abbreviations

Symbols

A : cross-sectional area, [m²]

c : absolute velocity, [m/s]

H : head, [m]

M_T : friction moment due to shear stresses, [Nm]

M : external torque, [Nm]

p : static pressure, [Pa]

P : circumferential position parameter

Q : volumetric flow rate, [m³/s]

r : radius, [m]

u : circumferential velocity, [m/s]

w : relative velocity, [m/s]

Y_{th} : theoretical flow conditions specific work

β : blade metal angle, [°]

δ : deviation angle, [°]

φ : flow coefficient

γ : slip factor

ψ : head coefficient

ρ : density, [kg/m³]

σ : cavitation number

ϑ : angular coordinate measured from the rotation axis using the right-hand rule, [°]

ω : pump angular velocity, [1/s]

Abbreviations

LE: Leading Edge

LOX: Liquid Oxygen

NLPQL: Nonlinear Programming by Quadratic Lagrangian

OIT: Osaka Institute of Technology

OSFM: Optimal Space-Filling Method

TE: Trailing Edge

Subscripts/Superscripts

cav: cavitating condition

in: pump inlet

m: meridional component

out: pump outlet

s: static

t: total

tip: inducer tip

vap: vapour

wet: wet condition

u: circumferential component

1: impeller inlet

2: impeller outlet

∞ : vane congruent flow conditions

1 Introduction

1.1 Background

Liquid rocket engines are employed in the majority of the launches of nowadays space industry. All the most important commercial launch vehicles, the European Ariane 5, the Americans Falcon 9 from SpaceX and Atlas V from United Launch Alliance, the Chinese Long March 7 as well as the Russian Soyuz, currently used to carry astronauts to the International Space Station (ISS), make use of liquid rocket engines, alone or in combination with solid boosters.

Liquid propelled vehicles are widely employed because of their efficiency and versatility. The former is usually expressed as Specific Impulse (I_{sp}) which mathematically represents the ratio of the produced thrust to the weight flow of the propellant:

$$I_{sp} = \frac{F}{\dot{m}g_0}$$

It is, therefore, a measure of how effectively a rocket is using the propellant to generate thrust. The versatility of liquid propelled rockets, instead, lies into the possibility to regulate the thrust by controlling the amount of fuel and oxidizer flowing into the combustion chamber. This possibility does not exist for solid-propellant rockets where, after the ignition, the combustion cannot be stopped.

For these reasons, often solid boosters are employed in the first phase of the mission, to provide the initial acceleration and then liquid rockets are ignited to complete the ascent to orbit exploiting their throttling capability.

Many types of liquid rocket engines exist, using different configurations for the feeding system and even employing different propellants but all of them have in common one component which is needed in order to provide the required pressure and flow rates: the turbopump.

Turbopumps are driven by turbines, which expand exhaust gases, and they pump cryogenic propellant at high rotational speeds. This working condition can lead to the formation of cavities at the impeller inlet potentially leading to mission failures.

The present work aims at investigating the design of one of the countermeasures found to limit cavitation detrimental effects on liquid rocket engines performance: the splitter blade.

1.2 Research Questions and Goals

The main goal of this thesis is to develop an optimization framework for the design of splitter blades which can improve the cavitating performance of the baseline pump. The framework is validated through comparison with experimental measurements. By developing the framework, analyzing the optimal geometry and carrying the experimental tests the following research questions can be answered:

- What is the gain of performance of the pump achievable with a splitter shape optimization, in terms of operative range under cavitation?
- What are the most important parameters for splitter design?
- Is the optimization framework a valuable means for splitter design?

The successful achievement of the project goal and the complete answer to the research questions allows to reach other objectives:

- Understand the physical mechanisms underlying the performance improvement deriving from the application of splitter blades;
- Define guidelines to design splitter blades of improved effectiveness

1.3 Originality of the Work

The literature review, presented in the following sections, highlights the need for a further research on the topic of splitter blades design for pump cavitation. The number of studies conducted on the subject is relatively contained but, most important, the use of nowadays common optimization strategies, such as those using surrogate-based models, are missing. The novelty introduced by this research, therefore, lies in:

- The application of CFD-based optimization to improve cavitating performance in turbopumps
- The validation of the numerical framework by testing the optimized turbopump geometry manufactured via 3D printing

The splitter design parameters that are retained to be the most relevant and the most widely investigated in literature can be studied in a more complete way. Given the automatic creation of various splitter shapes, the optimization framework allows to consider into the design process the mutual influence over performance of the different parameters.

The Design of Experiments and the Response Surface Optimization included within the framework open to new possibilities. The surrogate-model, for example, makes it possible to predict the performance of several splitter blade shapes without running any extra-simulation or without the need of multiple experiments.

1.4 Outline of the Thesis

The present thesis report summarizes the most important aspects of the research work. The intent is to give a clear representation of the optimization framework creation, of the content of the framework itself and, in the end, of the outcome of the optimization. The following structure is employed:

- Chapter 2: deals with the theoretical concepts necessary to understand the context where the project collocates. The first part is a short presentation about turbopumps and their basic working principles and parameters.
- Chapter 3: introduces the baseline pump geometry.
- Chapter 4: describes the technical approach used for the project. Therefore, the optimization framework is discussed in details.
- Chapter 5: presents the optimized shape and the experimental validation.
- Chapter 6: the flow field is analysed to understand the impact of the optimal splitter blade shape on the pump performance.
- Chapter 7: the conclusions and recommendations for further studies are presented.

2 Theoretical background

A turbopump is generally composed by two main elements: a turbine, driven by hot exhaust gases, and the actual pump, driven by the turbine.

The pump is usually divided into three main components: the inducer, the impeller and the volute.

A cutaway of the oxidizer turbopump from the Vulcain 2 rocket engine, currently used in the European launcher Ariane 5 is presented in Figure 2.1.

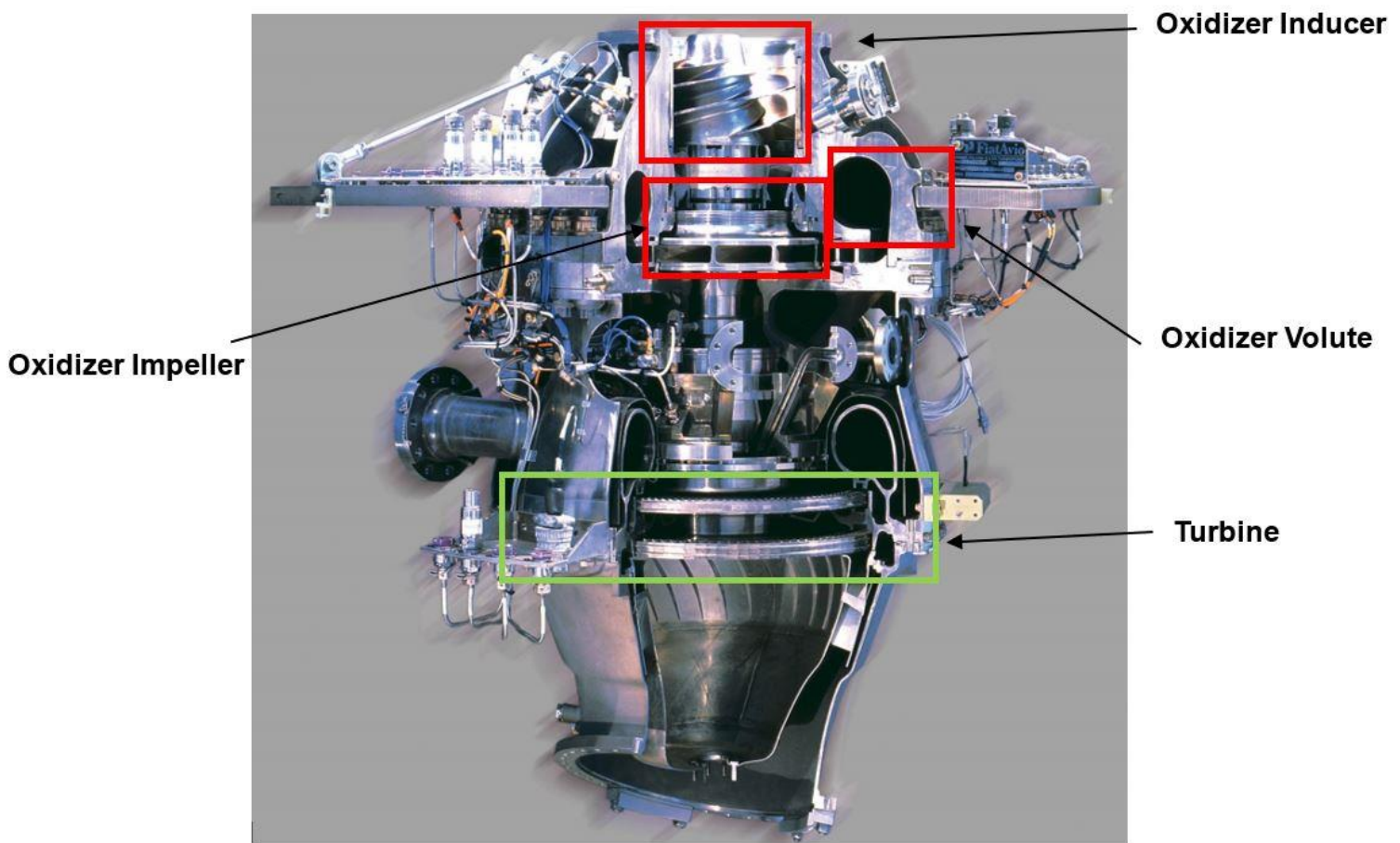


Figure 2.1: Cutaway of the oxidizer turbopump of the Vulcain 2 engine equipped in the first stage of the Ariane 5 five. The fuel used is LH2, liquid-hydrogen, while LOX, liquid-oxygen, is employed as oxidizer. Courtesy of Avio.

Extremely high rotational speeds, up to 35800 rpm for the liquid hydrogen turbopump of the Vulcain 2 engine [1], allow a minimization of volume and mass, justifying the increase of system complexity. As an example of the complexity of a turbopump-fed rocket, Figure 2.2 shows a simplified view of the Space Shuttle Main Engine flow diagram where the turbopumps can be recognized. In this specific case the rocket uses four turbopumps to serve the high and low-pressure feed lines of both the fuel (liquid hydrogen) and the oxidizer (liquid oxygen).

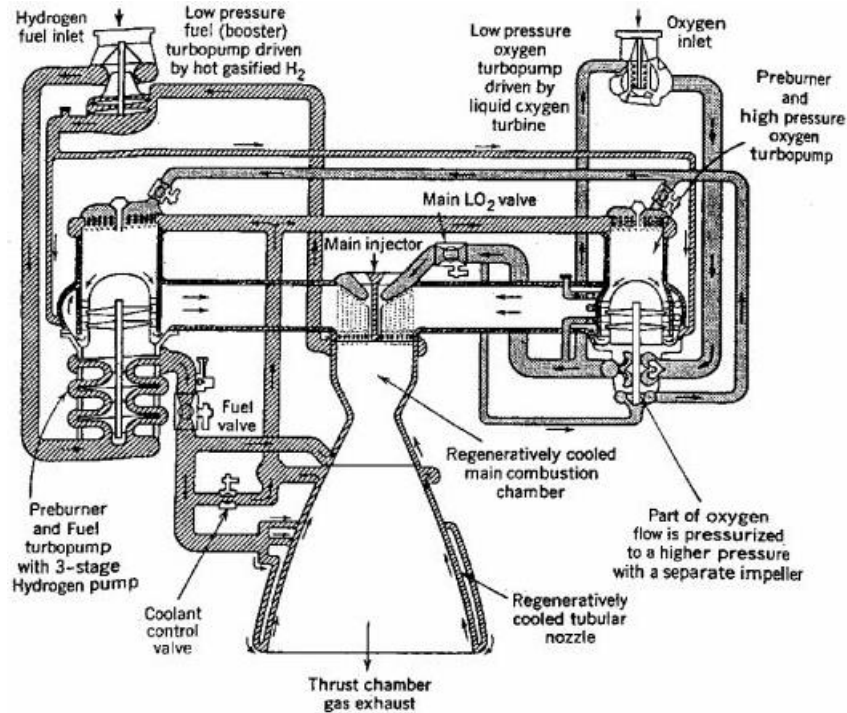


Figure 2.2: Simplified flow diagram of SSME (Courtesy Rocketdyne).

The challenges imposed by modern space launch industry to reduce costs, determines a continuous research of improved performance which most of the times translates, for a liquid-propelled rocket engines, into more stringent requirements towards the turbopumps. The need is for improved performance and reduced weight and size. The solution to reach the goals is to increase the rotational speeds even more.

High rotational speeds determine operating conditions where cavitation can occur within the turbopump. When cavities appear, they cause blockage in the blade passage determining performance loss, instabilities and mechanical damages. In particular, unsteady cavitation phenomena can determine blade loading oscillations and vibrations which in some cases eventually led to mission failure as in the case of the Japanese H-II rocket where the cavitation-induced vibrations on the inducer of the LE-7 engine determined a structural damage to the turbopump. Therefore, the role of cavitation in turbopumps is of primary importance for space propulsion today. In the present chapter, a theoretical background will be presented dealing with cavitation and the main performance parameter of a pump.

2.1 Overview of Turbopump Performance

2.1.1 Wet Performance

The core of the present project is to study the impact of cavitation on turbopump performance. Therefore, an introduction on the typical pump performance is necessary.

All kind of pumps, not only turbopumps for space launchers, are described by few parameters, the most important of them being the pressure rise and the volumetric and mass flow rates.

The pressure rise is typically expressed with *the head* which is defined as the height of the column of liquid exerting, at its base, the same static pressure as the pressure rise across the of pump:

$$H_s = \frac{p_2 - p_1}{\rho g}$$

where g is the gravitational acceleration, ρ the density of the flow and H_s indicates the static head. In the same way it can be defined the total head H_t which is calculated using the total pressure rise. These parameters are conveniently nondimensionalized. For the present work the following formulation applies. The static head coefficient is defined as:

$$\psi = \frac{p_{out} - p_{in}}{\rho u_2^2}$$

where p_{out} and p_{in} refer, respectively, to the static pressure at the outlet and the static pressure at the inlet of the pump and u_2 is the circumferential velocity at the impeller outlet. The flow coefficient is written as:

$$\varphi = \frac{c_{m,in}}{u_{tip}}$$

where $c_{m,in}$ indicates the meridional component of the absolute velocity at the inlet and u_{tip} is the circumferential velocity at the inducer tip.

The flow coefficient is defined at the inlet of the pump because, in case of cavitation, which first happens at the pump's inducer, it is a more sensible parameter [2].

The head-capacity curve of the pump consists of the head coefficient as a function of the flow coefficient, independently from the rotational speed. It is, therefore, the relation between the pressure rise imparted to the fluid by a specific pump for a given volume, or mass flow, at constant rotational speed. This curve is also denoted as *wet performance curve* because it does not consider the cavitation effect.

An example of a typical wet performance curve is given below:

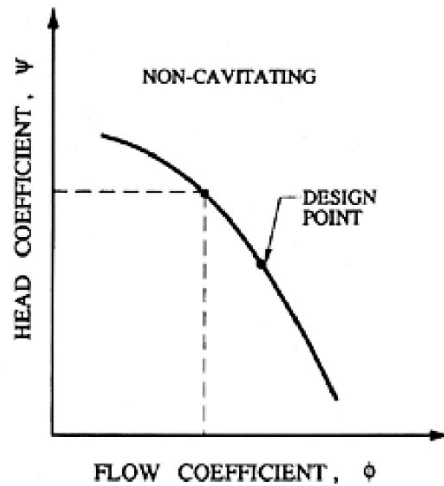


Figure 2.3: Generic wet performance curve for a pump. [2]

The wet performance curve is generally obtained by deducting all the hydraulic losses caused by friction and vortex dissipation from the ideal relation between ψ and ϕ . **Error! Reference source not found.** shows a qualitative example on how the losses are distributed for different flow rates. The friction losses are commonly retained to grow with the square of the flow rate.

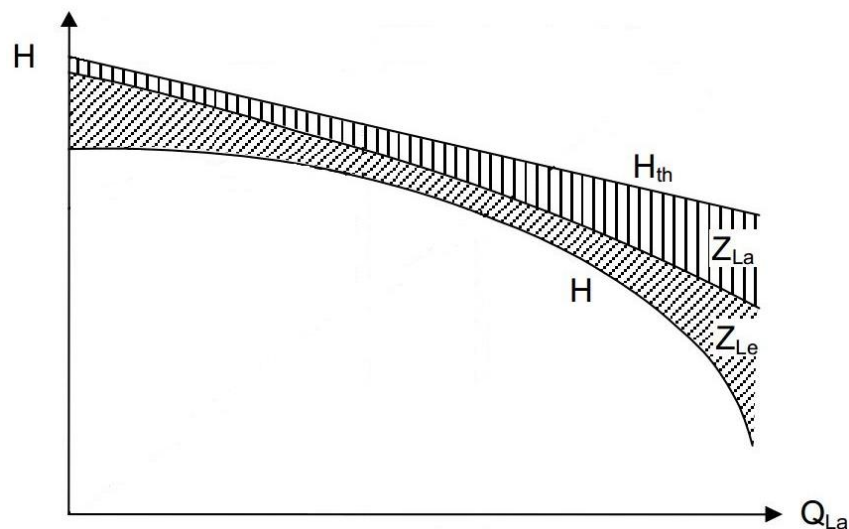


Figure 2.4: Typical example of losses contributions leading from the theoretical head curve, H_{th} , to the real one, H . Plot adapted from [3], where Z_{La} and Z_{Le} indicate, respectively, the contributions of impeller and the diffuser.

Losses due to vortex dissipation are generated by nonuniform flow distributions. Nonuniformities mainly derive from part-load recirculation, flow separation and incorrect approach flow and the loss mechanism is the exchange of momentum between low energy flow and through-flow.

In particular, an incorrect approaching flow at the impeller inlet generates the so called “incidence losses”. This type of losses is minimum at design flow coefficient because the geometry of the impeller is devised based on optimal incidence at design condition, but at different flow rates they can represent one of the major contribution to performance degradation. The main consequence is a region of separated flow at the impeller blades’ leading edge. This mechanism can be also used to understand the effects of cavitation on the cavitating performance and it will be further illustrated in sec.2.1.4.

2.1.2 Theoretical Head and Euler's Turbine Equation

Figure 2.4 presented the so called *theoretical head*. The theoretical head is an important first-attempt estimation of the performance of a pump. Its derivation is very simple but effective in better understanding the working principles.

Assuming an incompressible and inviscid flow, Brennen [2] illustrates the relation between head and flow coefficients applying Bernoulli equation for a rotating system:

$$\frac{2p_1}{\rho} + w_1^2 - r_1^2\omega^2 = \frac{2p_2}{\rho} + w_2^2 - r_2^2\omega^2$$

where r is the radial coordinate and the terms $\frac{2p}{\rho} + w^2$ on both sides indicates the total pressures, with the static and dynamic contributions.

By making explicit the total pressures and the absolute velocities, using the conversion formula $c^2 = w^2 - u^2 + 2uc_u$, Bernoulli can be written as:

$$p_2^t - p_1^t = p_2 - p_1 + \frac{\rho}{2}(c_2^2 - c_1^2) = \rho\omega(c_{2u}r_2 - c_{1u}r_1)$$

and, considering the head and flow coefficient as defined in [2]:

$$\psi = \frac{p_2^t - p_1^t}{\rho r_2^2 \omega^2}, \quad \varphi = Q/A_2 r_2 \omega$$

and the contribution of the inlet swirl $c_{1u} = 0$, the final relation between ψ and φ is found to be as:

$$\psi = 1 - \varphi \cot \beta_2$$

The same expression can also be determined by making use of the conservation of angular momentum and the conservation of energy.

As a consequence of Newton 2nd law of mechanics, the angular momentum must be preserved. Therefore, any change of the angular momentum within a machine equals the sum of the external moments.

The expression of the angular momentum at the inlet and outlet of a generic control volume can be expressed in the following way:

$$\rho Q r c_u$$

where c_u is the circumferential projection of the absolute velocity.

Assuming the flow to be inviscid, only an external torque, M is applied. Considering no pressure contributions in the circumferential direction, the formula of the conservation of angular momentum becomes:

$$\rho Q (c_{2u}r_2 - c_{1u}r_1) = M$$

which is known as the Euler's turbine equation. The formula states that the energy imparted to the flow translates, in the ideal case of no losses, into a total pressure rise by a variation of momentum between the inlet and the outlet of the pump.

By multiplying both sides by the angular velocity, ω , it is possible to obtain the driving power, P_{th} , and then the pump specific work, Y_{th} :

$$P_{th} = M\omega = \rho Q (c_{2u}u_2 - c_{1u}u_1)$$

$$Y_{th} = \frac{P_{th}}{\rho Q} = c_{2u}u_2 - c_{1u}u_1$$

In the end the theoretical head, H_{th} , is found as:

$$H_{th} = \frac{Y_{th}}{g} = \frac{c_{2u}u_2 - c_{1u}u_1}{g}$$

Being the flow incompressible, the conservation of energy and momentum are simultaneously satisfied. From the former, the following expression for the moment applied to the fluid can be obtained:

$$\rho Q(p_2^t - p_1^t) = M\omega$$

By equating this last formula with the expression for P_{th} , the Bernoulli equation $p_2^t - p_1^t = \rho\omega(c_{2u}r_2 - c_{1u}r_1)$ is found.

2.1.3 Velocity Triangles

The head coefficient is dependent on a velocity difference between inlet and outlet, as found in the previous equations. Considering the circumferential projection of the absolute velocity to be zero at the inlet, the outlet velocity triangle reveals to be the key parameter of the pump performance. In particular, since u_2 is retained to be a fixed pump characteristic, c_{2u} determines the pressure rise.

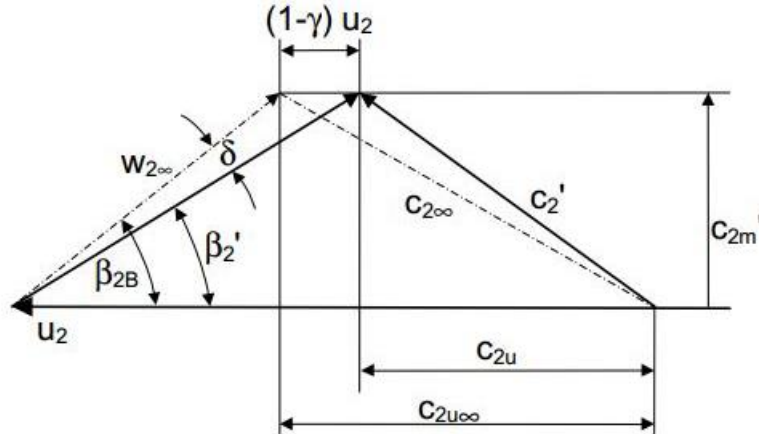


Figure 2.5: Velocity triangle at the impeller outlet.

Figure 2.5 illustrates the real case velocity triangle at the outlet of the impeller. The slip factor, γ is introduced to model the deviation of the real flow from the ideal case. Indeed, several factors influence the flow so that at the trailing edge it does not precisely follows the blade outlet angle but exits with a *deviation angle*, δ . Among others, velocity differences between pressure and suction sides of the blades, Coriolis acceleration and the difference in pressure downstream of the trailing edge. The ideal case flow is called *blade congruent flow*. For a fixed flow coefficient, the slip factor determines a c_{2u} that is lower than the ideal circumferential projection of the absolute velocity, $c_{2\infty u}$, leading to a lower pressure rise. The equation relating the ideal and actual velocity to the slip is the following:

$$c_{2\infty u} - c_{2u} = (1 - \gamma)u_2$$

therefore, blade congruent flow is found for $\gamma = 1$.

2.1.4 Cavitation Description

Cavitation is a pressure-driven phase change which happens in region of the flow where the static pressure locally drops to the vapor pressure of the liquid. A cavity filled with vapor generates so that a two-phase flow is created in a small domain of the flow field. Streamlines deviation leads to uneven blade loading, hence vibrations and mechanical stresses. Instabilities due to unsteadiness of cavitation mainly occur at the inducer, being the component most subjected to cavitation.

Several types of cavitation can be possible. Figure 2.6 from [2], shows the variety of cavities that can occur in a pump.

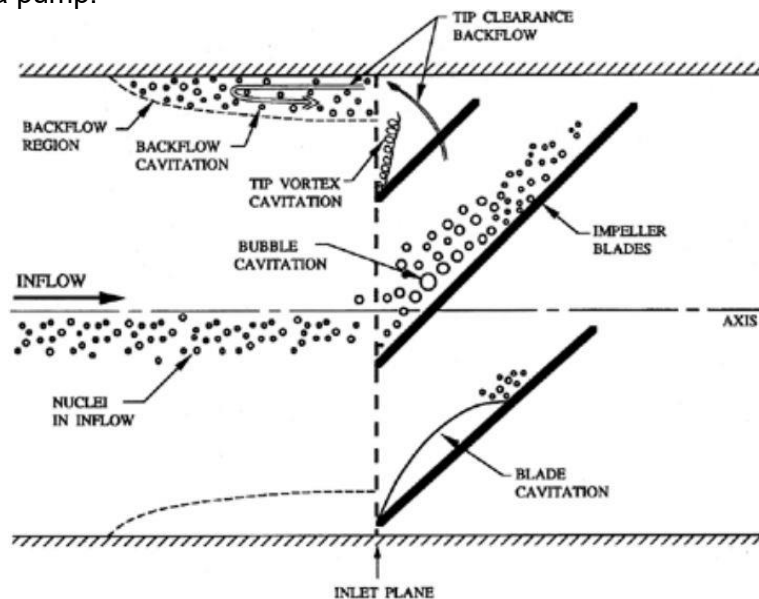


Figure 2.6: Types of cavitation occurring in pumps.

Backflow cavitation and tip vortex cavitation are typically found in inducers. In this work, the cavitation type to be studied is the blade cavitation at the impeller.

Blade cavitation is typically created on the suction side of the blade in the proximity of the leading edge and acts as an extra-blockage, in addition to that caused by the blade thickness. When the flow is decelerated further aft, the pressure increases and the vapor bubbles implode. Figure 2.7 schematically shows this type of cavitation.

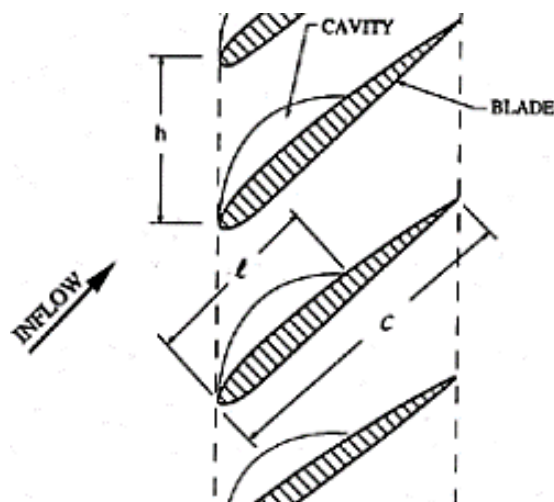


Figure 2.7: Blade cavity showing the increased blockage at the inlet. Image from [2].

The main detrimental effect of blade cavitation is the increased hydrodynamic losses caused at the impeller inlet which diminish the delivered pressure rise. To explain the mechanism leading to the deterioration of performance, let us look at Figure 2.8 from [3].

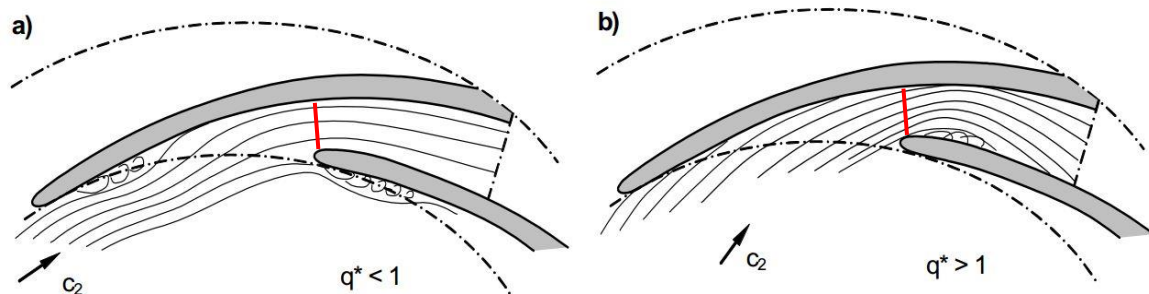


Figure 2.8: Leading edge separation due to off-design flow rates. This condition can be used to explain the detrimental effect of cavity bubbles on performance. In red the throat areas are indicated. [3]

Gülich describes the leading edge separation happening at off-design flow rates. The regions of stalled fluid cause hydrodynamic losses due to exchange in momentum with the core flow. If those separation zones are filled with vapour cavities, the conditions are similar. Therefore, similarly to separated flow, blade cavitation determines a reduction of the pressure rise due to increased hydrodynamic losses caused by the exchange of momentum with the through-flow.

Moreover, Figure 2.8a shows the situation at part loads, when the incidence angle is positive hence determining a region of separated flow on the blades suction side. On the contrary, separation happens on the pressure side when the incidence is negative, at high flow rates (Figure 2.8b).

The latter case determines the worst scenario because it diminishes the throat region of the blade passage. The flow is then overaccelerated and the losses increase.

Referring these observations to the analogy with cavitation, the cavity size and location play an important role. The formation of vapour bubbles on the pressure side will have an immediate negative impact on performance. On the other hand, suction side cavities, while increasing the pressure losses within the impeller, will become extremely detrimental to performance only when their extension will become considerable, to the point that the blade passage throat is altered.

2.1.5 Cavitating Performance

To describe the cavitating performance of a pump, the head coefficient is related with the cavitation number, defined as:

$$\sigma = \frac{p_{in} - p_{vap}}{0.5\rho U_{tip}^2}$$

The cavitation number represents the most used parameter for evaluating the potential for cavitation [2].

During a cavitation ramp test the pressure of the system is reduced slowly and continuously, decreasing the cavitation number while maintaining fixed flow coefficient. As the pressure is reduced cavitation in the turbopump increases, causing head drop and ultimately leading to cavitation surge. The head drop-off point is often defined as the point for which the head coefficient is 3% lower than the head coefficient without cavitation. The drop-off signifies the

loss of performance due to cavitation and the limit of the stable range of operation of the turbopump.

To indicate the different regimes of cavitation encountered during a ramp test, special cavitation numbers are defined.

The cavitation inception number, σ_i , is described by the standard formula of σ where in place of p_{in} it is inserted the value of the particular pressure at which cavitation first occurs. The critical cavitation number, σ_a is defined using the inlet pressure at which the head coefficient falls of 3% from the wet value. Lastly, the breakdown cavitation number, σ_b , represents the condition where cavitation has led to a major deterioration of performance.

The typical cavitating performance of a turbopump is presented in the form of the so-called "knee-curve" in Figure 2.9.

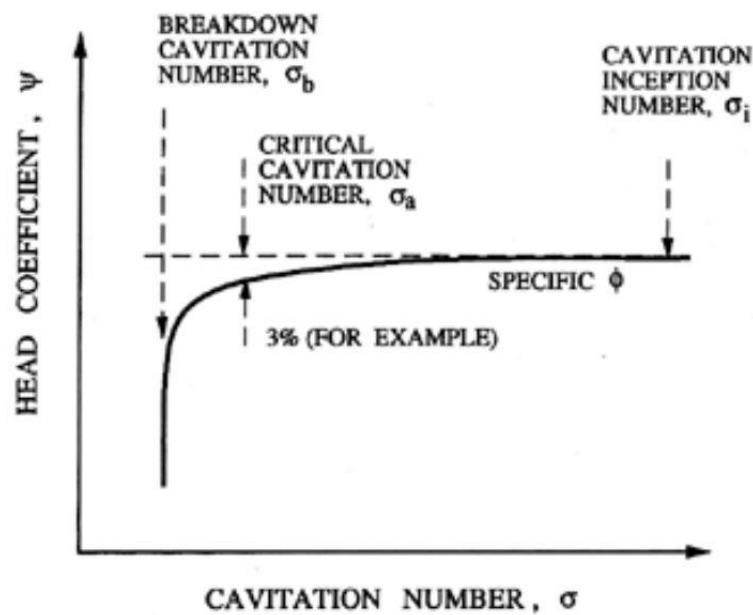


Figure 2.9: Qualitative cavitating performance curve of a generic pump. The most important cavitation parameters are indicated.

2.2 Cavitation Mitigation Techniques

Because of the importance of having stable operations several countermeasures to cavitation were studied in the past and are currently investigated. In the following, the most relevant solutions will be presented and, in particular, the splitter blades, will be covered in sec. 2.2.4.

2.2.1 Casing Treatment

Casing treatment has demonstrated to be useful in influencing stall inception point and eventually to increase the stable operating range in compressors and pumps. With casing treatment, a vast number of artefacts is indicated. In axial compressors, for instance, slots or honey combs are applied whereas in pumps axial grooves are machined in the casing [3]. Figure 2.10 gives an example for an axial compressor.

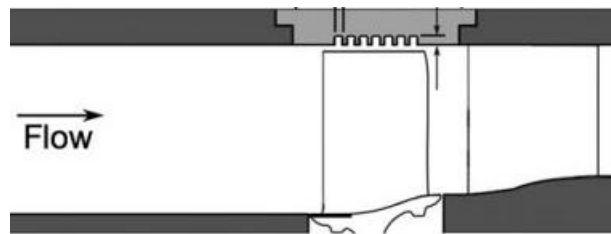


Figure 2.10: Example of casing treatment extending in the blade tip region. Picture from [4]

The geometry of centrifugal pumps determines interactions between hub and shroud, blade pressure and suction sides and impeller inlet and blade passage. Therefore, complex 3D flow patterns develop. Backflow ahead of the impeller is one example that can lead to instabilities and can contain cavities. It generates usually at low flow coefficients at it consists of fluid flowing from the inducer back to the inlet of the pump through the tip gap, driven by the pressure differential between the blade passage of the inducer and the upstream region before it.

Grooves aim to straighten the flow approaching the inlet of the pump. Their number, dimensions, shape and location have to be set based on the specific application. The mechanism underneath the positive impact on performance of this type of casing treatment, is essentially based on an exchange of momentum between the approaching flow upstream of the impeller, usually swirling, and the liquid contained in the grooves which cause a reduction of the tangential velocity.

2.2.2 Leading Edge Shaping

Leading edge shaping has a significant effect on both cavitating and non-cavitating performance of a pump [2]. In general, it is possible to say that the sharper the leading edge the better the hydraulic performance as Brennen illustrates in [2]. The results presented below, Figure 2.11, refer to the leading edge of an inducer, being this component the most critical for cavitation.

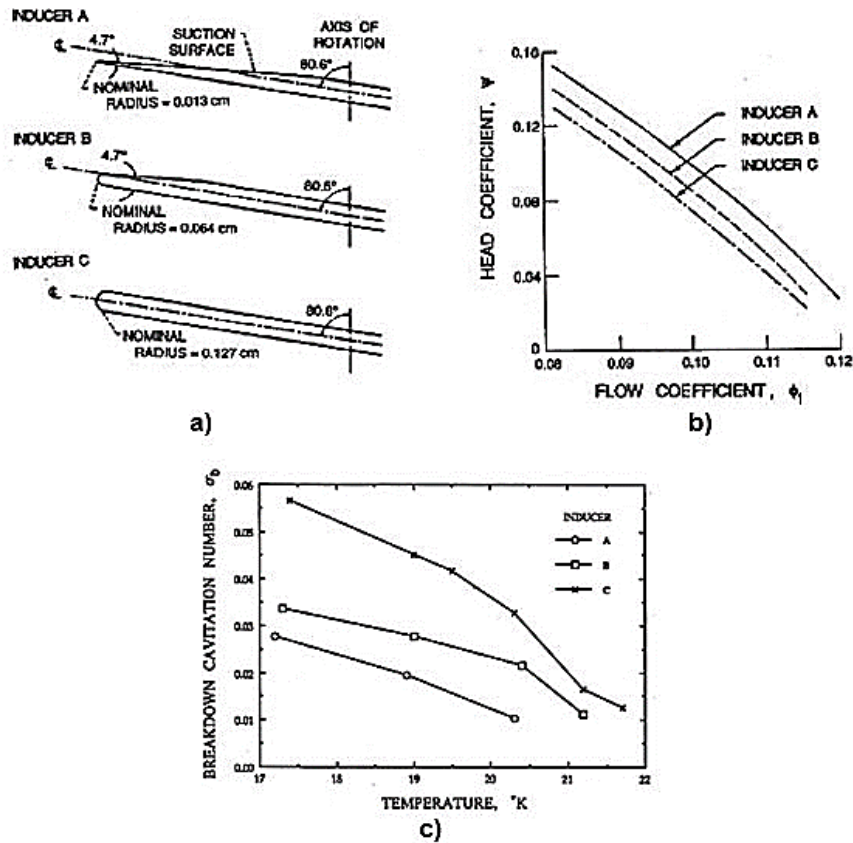


Figure 2.11: Impact of inducer leading edge on hydraulic performance. Figures from [2].

The impact of the leading edge shape is also found within this thesis project, with simulations showing a dramatic reduction of cavity size on the inducer when going from a cut-off to a round leading edge,

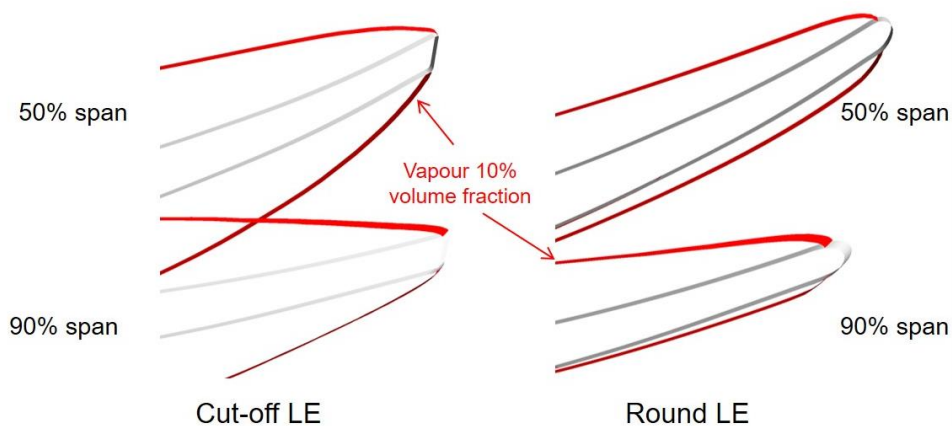


Figure 2.12: CFD results showing the importance of the leading edge shape on cavity size.

A cut-off solution determines higher velocities at the leading edge, which, create an enlarged low pressure area, compared to a round configuration where the flow is less accelerated, as it is clearly visible from Figure 2.12.

2.2.3 Inducer

The inducer is the most employed cavitation countermeasure for liquid propellant rocket engine turbopumps. It is used in both fuel and oxidizer turbopumps and its scope is quite simple: to raise the static pressure in order to avoid or reduce cavitation on the highly loaded impeller blades.

Using an inducer allows an extension of the stable operative range of the turbopump or an increase of the rotational speed of the machine, thus leading to a reduction of dimensions and weight. Typically, inducers consist of an axial flow stage having sharp leading edge and thin blades, designed to work at little incidence angles in order to minimize the production of cavitation [2]. Working with an incidence angle of few degrees makes cavitation formation happen on the suction side of the blades, avoiding the alteration of the pressure side, being the most critical one as discussed before, or dangerous oscillations between the two. Figure 2.13 presents the inducer used in the low-pressure LOX turbopump of the Space Shuttle Main Engine (SSME).

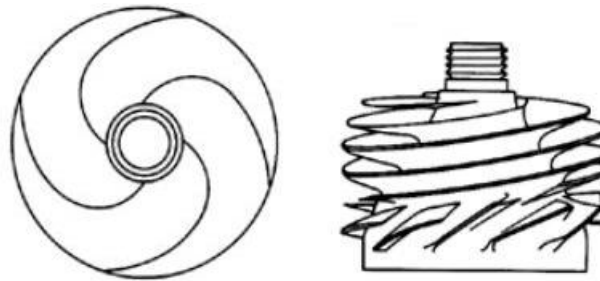


Figure 2.13: SSME low pressure LOX turbopump inducer. Figure from [2].

2.2.4 Splitter blades

The concept of splitter is simple, being a blade of reduced length with the leading edge shifted downstream of the impeller inlet. The most evident and immediate effect is to reduce the blade blockage at the inlet. Reduced blockage translates into lower velocities, hence higher pressures and reduced cavitation development compared to an impeller with only full-length blades. This is confirmed by Japkise [5] and Furst [6] who report that splitter blades enable higher mass flow through the impeller because of the reduction of cavity blockage in the turbopump.

Figure 2.14 presents a sketch, for a given span location, explaining the effect of replacing a full-length blade with a splitter one. It is possible to notice that the area occupied by the blades thickness (blue lines) is reduced at the inlet as if the number of blades were reduced from three to two. A lower number of blades, though, would implied an increases deviation of the flow from the blade geometry at the outlet, hence reducing the head rise of the pump. That is because less blades for the same energy transfer implies higher loads on each blade, hence an increased pressures and velocities difference between pressure and suction sides, one of the cause of the slip, as discussed in sec 2.1.3.

However, using splitter blades the load distribution remains more uniform and at the same time the leading edge region has reduced blockage. Therefore, splitter blades allow to take the advantage of a reduced inlet blockage as if some blades were removed, without increasing the flow deviation at the trailing edge.

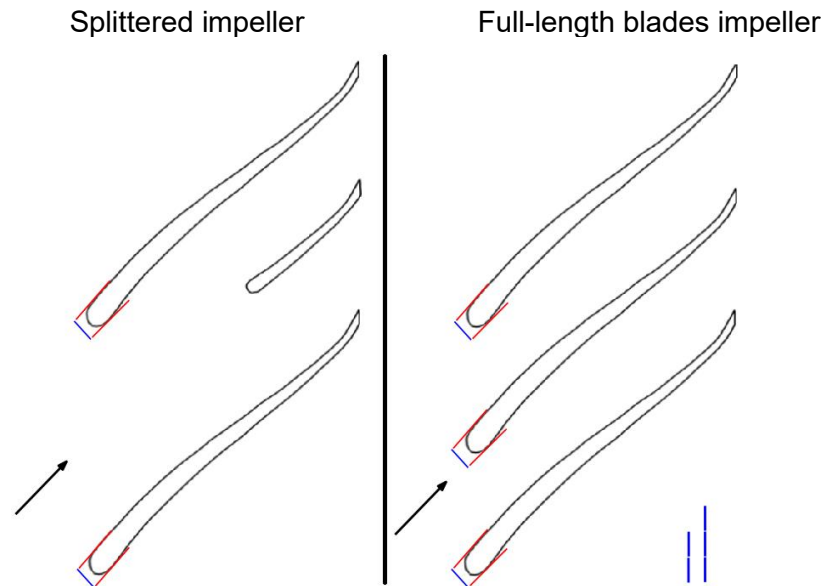


Figure 2.14: Inlet area comparison at a given span location. The extension up to the inlet of the middle full-length blade causes a reduced inlet area due to increased blade blockage for the full blades configuration.

The fundamental mechanism lying behind the positive impact of a splattered impeller solution has been explained, however, detailed studies on their overall effect on the flow field are few. In particular, there is a limited amount of research on the design methodology and the topic of splitter blades optimization for cavitation performance has not been thoroughly explored.

Onoue et al. [7] proved that splitter blades can be applied in conjunction with inducers to improve the pump cavitating performance and to delay the onset of cavitation drop-off. They found that an increased inlet area at the impeller reduces the amount of cavitation but also that the inducer had the most relevant role in the performance improvement.

Zhang et al. [8] investigated three different impeller geometries to assess the impact of splitter blades on the pump performance. In particular, they added splitter blades in the middle of the blade passage of the reference impeller having four full-length blades. The two splattered configurations differs because of the splitter leading edge position in the streamwise direction, hence because of the length. The addition of splitter blades leads to an appreciable increase of the delivered head and efficiency most probably due to the flow being more aligned to the blades in the outlet section because of the additional guidance given by the splitter blades. The two splitter configurations present also a reduced amount of cavitation which extends the operational range. However, the reason behind the cavitating performance improvement in this case cannot be attributed to the reduction of the blade blockage at the inlet because in this research the splitter blades have just been added in-between the main blades. Looking at the contours of vapour fraction, Figure 2.15, it appears that the splitter leading edge determines an earlier termination of the main cavity bubble developing from main blade suction side. At the same time the interaction of the leading edge position and the bubble modifies the flow field at the splitter suction side. The combination of the two effects results in the third design being the most effective, case c) in Figure 2.15. It is the one having shorter splitter blades with the leading edge position that delays cavitation and flow separation on the splitter suction side.

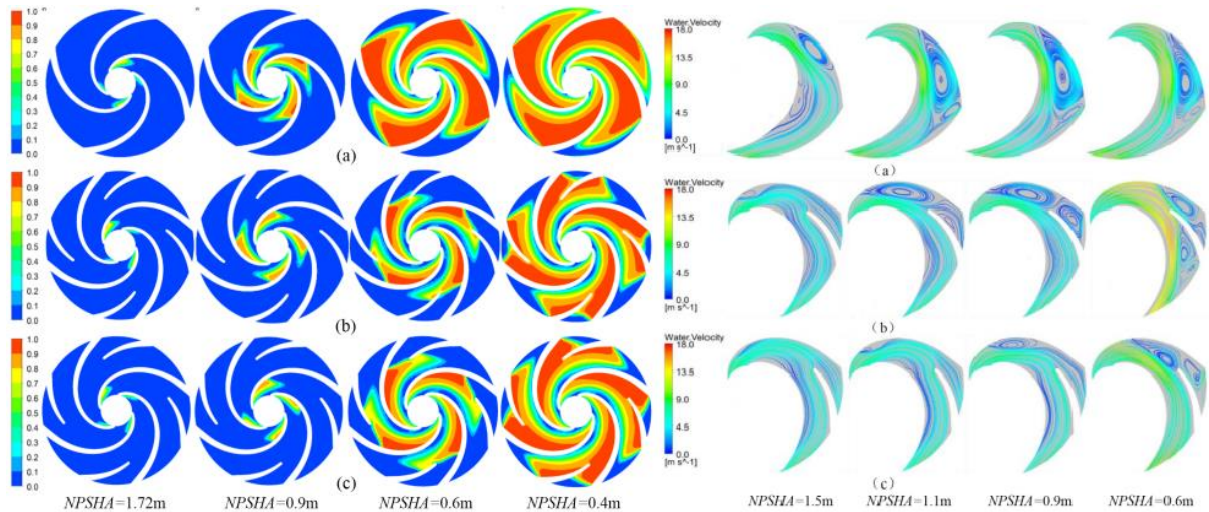


Figure 2.15: Contours of vapour fraction and relative velocity streamlines at midspan for the three different cases. Image taken from [8].

Yang et al. [9] compared the cavitating performance of two impellers, the baseline one having six full-length blades and the other designed with four splitter blades and four full-length blades. The splitted impeller maintains the same meridional geometry of the baseline one and the blades have the same shape. Numerical simulations and experiments reveal an improved efficiency and an extended operational range under cavitation for the impeller with splitters. The beneficial effects are found at all the flow rates tested, ranging from 75% to 135% of the design one, but appeared to be maximum at high 130% of the design level. In this condition, the drop-off cavitation number was 32.5% lower than the case with all full-length blades. Numerical results, Figure 2.16, shows similar trend, in agreement with the experiments.

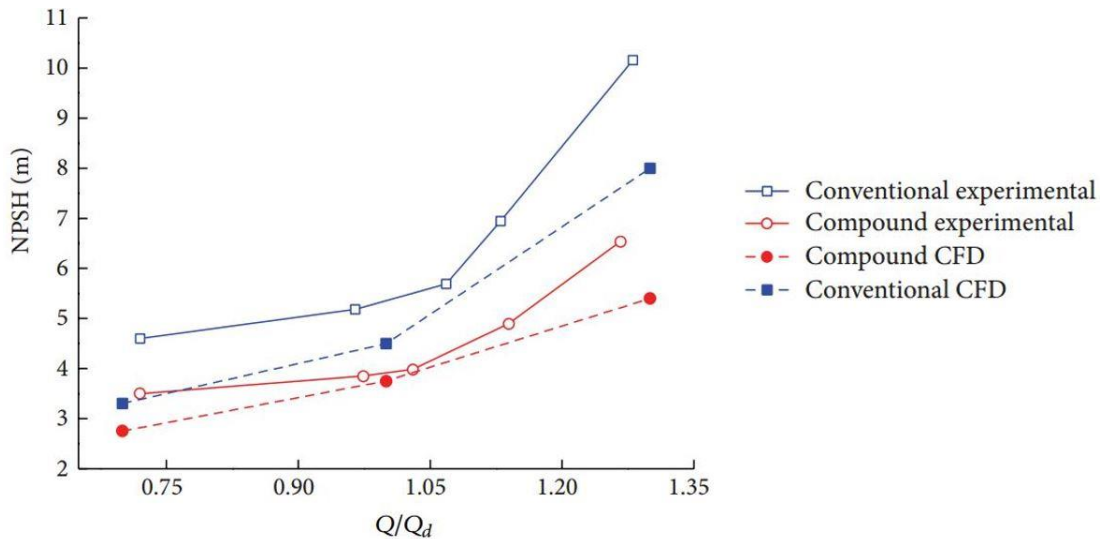


Figure 2.16: Improvement of cavitating performance as found by Yang in [9]. Conventional here refers to the impeller having only full-length blades whereas compound indicates the pump with splitter blades.

The analysis of the flow field shows that lower velocities are present at the main blades leading edge of the splitted impeller compared to the baseline one. From the pressure distributions it can be seen that reduced velocities lead to increased pressures especially at

the suction side of the main blades leading edge. The cause for this improvement is attributed to the augmented inlet area for the impeller with splitters which then reduces the amount of cavitation and delays its break-down.

Other works in literature [10, 11, 12, 13, 14, 15, 16] found improvements partially caused by a reduction of flow separation within the blade passage and partially to an increase in the average flow angle at the trailing edge.

Besides beneficial effects, also drawbacks of the application of splitter blades have been found. This indicates that solely the addition of splitter blades is not sufficient to bring improvement but that some design parameters are more relevant than others and their correct selection determines the improvement.

Cavazzini et al. [17] suggest that the performance improvement is often limited to high flow coefficients, being splitters beneficial impact limited mainly to a change in the incidence angle caused by a modified thickness-blockage of the main blades. At partial flow rates a decrease of the average incidence angle is expected while for large flow rates the angle increases. As a consequence, the suction performance improvement should be found just in the latter case. Indeed, the cavitation performance of an impeller is determined mainly by the size of the cavity bubble shedding from the main blade leading edge and the incidence angle plays a crucial role in the cavitation inception and extension. In their research, they found confirmation of this idea finding improved cavitating performance with the splintered impeller just for large flow rates. At part load, the splintered impeller was underperforming the baseline pump having all full-length blades.

From the analysis of the flow field it becomes clear the role played by the modified inlet area and its influence on the incidence angle. An enlarged incidence angle determined reduced cavity blockage at 144% of design flow rate whereas a decreased incidence led to increased super-velocities and lower pressures, hence more extended cavities, on the main blades suction side at 68% of design flow rate.

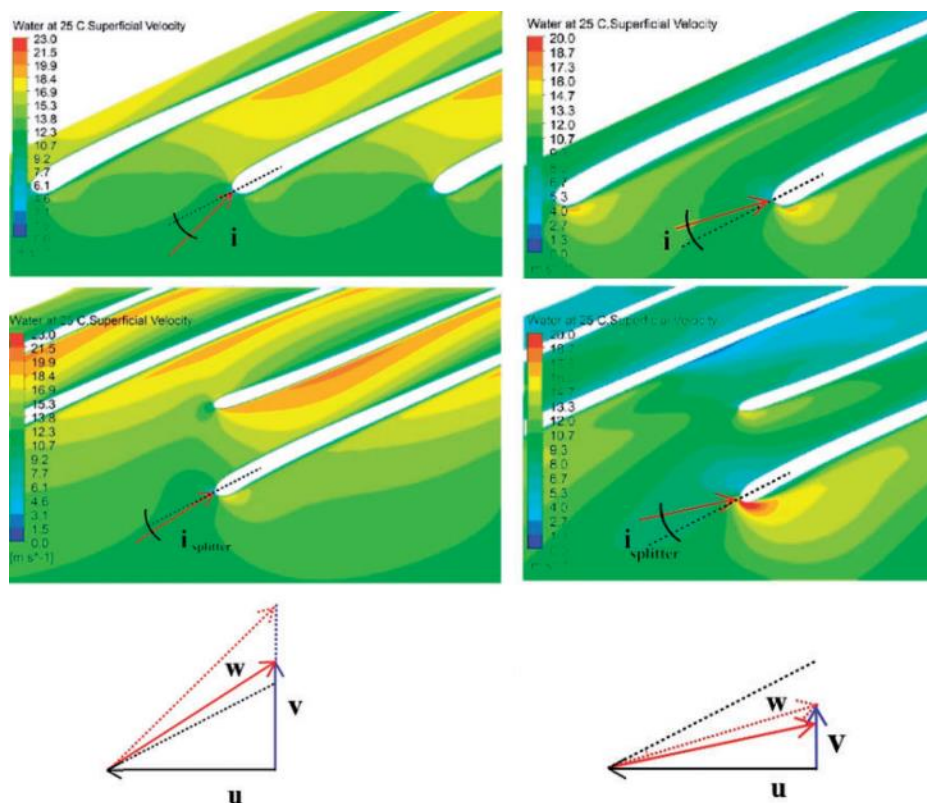


Figure 2.17: Image taken from [17]. Contours of relative velocity and indication of the incidence angle at 144% of design flow rate (on the left side) and at 68% (on the right side). Comparison between impellers with full-length blades (top) and splitters (bottom).

The identification of splitter designs which were not positively contributing to the suction performance improvement started a research of the most influencing parameters. Design guidelines have been proposed by Gülich [3], Cavazzini et al. [17] and Japikse [5], including indications on how to select the total number of blades, the meridional position of splitters and the impeller design. Several works in literature [10, 11, 12, 13, 14, 15, 16] indicate that the circumferential position, the length and the blade angle distributions are the most critical design parameters for splitter blades.

The number of blades, in particular, plays an important role and especially in [10] it is found that adding splitter blades to impeller having five or more full-length blades, causes extra-blockage and the augmented overall surface increases the skin friction losses nullifying all the positive effects on performance.

Moreover, Miyamoto et al. [18] reported that centrifugal impellers with splitter blades yield reduced blade loading and increased absolute circumferential velocity and total pressure at the outlet with the circumferential position of splitters being one of the driving parameters for the improvement. With the ultimate goal of finding the most critical parameters, several works [13, 16, 19] conducted parametric studies based on the number and length of splitter blades, but shape optimization is rarely applied in rocket turbopumps due to the challenges associated with the multiphase flow, in particular being the numerical costs.

Nevertheless, gradient-free and gradient-based shape optimization methods have seen increased application to splitter blades/vanes design in recent years. Clark et al. [20], for example, used multi-objective optimization to the design of splitters for low aspect ratio vanes of turbines. The analysis led to the identification of the critical flow feature and proposed design recommendations for vane rows employing splitters.

In conclusion, a large body of work exists on the effect of splitter blades on wet and cavitating pump performance [7, 8, 9, 12], but a study conducting an optimization of the most important design parameters for splitter blades with the objective of extending the operational range under cavitation has not been performed. Splitter blades are often designed by simply adding short blades with the same shape as the main blades, greatly limiting their effectiveness and modifying the blade loading distribution and the head-capacity curve, as Cavazzini points out [17]. Many previous works used to compare impellers with different number of blades leading to uncertainty on the outcomes. The results is a situation where, today, there is no clear indication on how to select the best design for splitter blades and the physical mechanisms responsible for the performance improvement is not completely understood [3] [16] [17].

3 Characterization of the Baseline Geometry

The baseline pump is characterized by three components. A three-bladed unshrouded inducer (with a 2% of the span tip gap), a three-bladed shrouded impeller and a volute. The details of the geometric characteristics of the pump are presented in Table 3-1.

Table 3-1: Overview of the main parameters of the baseline pump impeller.

Details of Baseline Pump Impeller	
Design flow coefficient	0.207
Blades	3+3 splitter
Tip radius	66.6 mm
Inlet hub to tip ratio	0.405
Outlet hub to tip ratio	1
Inlet tip angle	18.3°
Outlet tip angle	14°
Rotational speed	3600 rpm
Blade thickness	3 mm

An exploded view of the four main components of the pump is given in Figure 3.1. Items number 2 and 4 are the inducer and the impeller, respectively, whereas item 1 is the inlet cone, which houses the screw that maintain together the four pieces during the tests, and item 3 is the cylinder which is needed to separate the impeller from the inducer and to have it positioned in the transparent acrylic casing of the test-rig to observe cavitation.

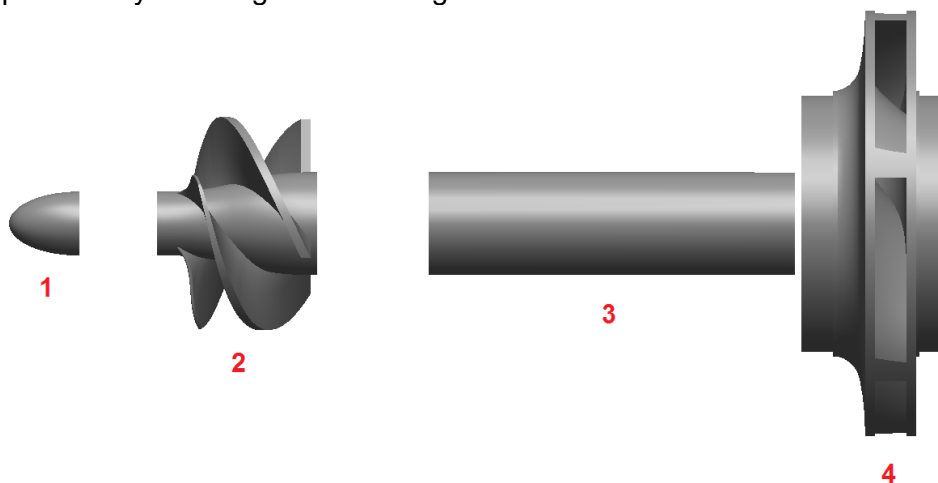


Figure 3.1: Exploded view of the pump's components.

Figure 3.2 shows a meridional view of the pump, where the splitter blade leading edge can be identified in the impeller passage. The inducer is located 2 diameters upstream of the impeller to avoid any coupling between the components.

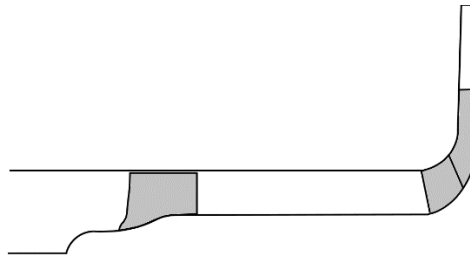


Figure 3.2: Pump meridional plane, with the inducer and impeller blades colored in dark grey.

The only parametrized parts are the splitters and, consequently the pump component where they are housed, the impeller, has been rebuilt within a parametric CAD software to accommodate their shape variation, as explained in the following Sections. Instead, for what regards the other parts of the pump, the inlet and outlet pipes, the volute and the inducer, they are reconstructed in another way. Both pipes and the inducer are directly recreated as a mesh domain, while the volute is modified from the baseline shape to a simplified one presented in Figure 3.3. The change is done to reduce the computational costs of the optimization by removing the otherwise necessary extra-fine mesh in the sealing between impeller and casing. The shape and dimensions of the simplified outlet section are selected in order to avoid convergence issues during the simulations.

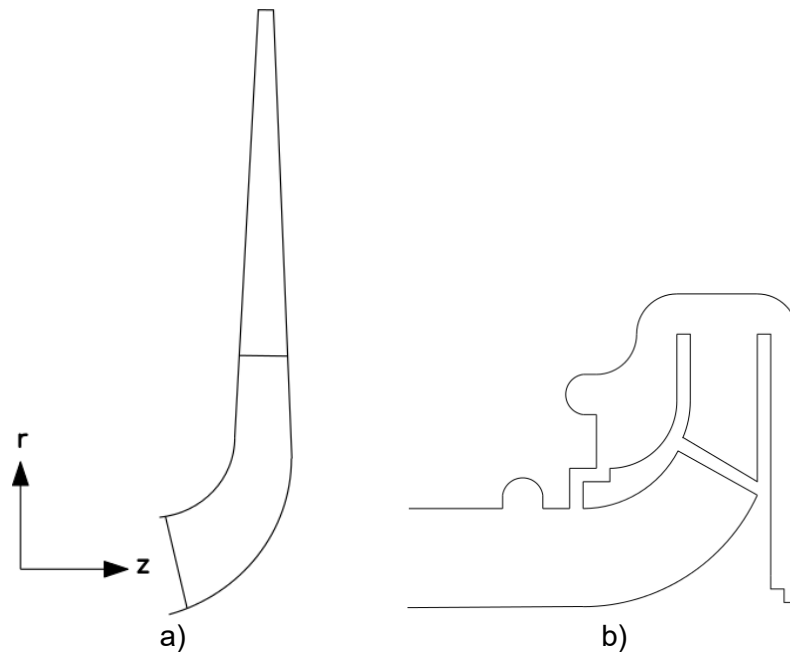


Figure 3.3: Comparison between the simplified outlet section, a), and the complete volute, b).

Nevertheless, it is important to understand the effects that this simplification brings to the pump characteristics. Therefore, a volute is recreated to run few simulations, outside the optimization loop, to be able to assess the differences. The volute used derives from the one of Figure 3.3b but without the flow leakage passage, as shown in Figure 3.4. The outlet of the pump is then placed further downstream, in the same position as the measurements are taken in the experiments, with the addition of an outlet pipe.



Figure 3.4: Sketches of the volute used in the simulations. On the left meridional plane view, to underline the absence of the leakage flow, on the right the complete volute as seen from the -z axis direction.

The baseline geometry already contains splitter blades because the impeller design has been devised from a previous study at the Osaka Institute of Technology (OIT). There, a full-length blades impeller has been substituted with a splitted version and the addition of the inducer. However, the splitter blades have not been optimized.

Within that research, [7], it is found that the design used as baseline for this thesis is the most performing one leading to a significant improvement of suction performance by lowering the drop-off cavitation number by 70%, Figure 3.5.

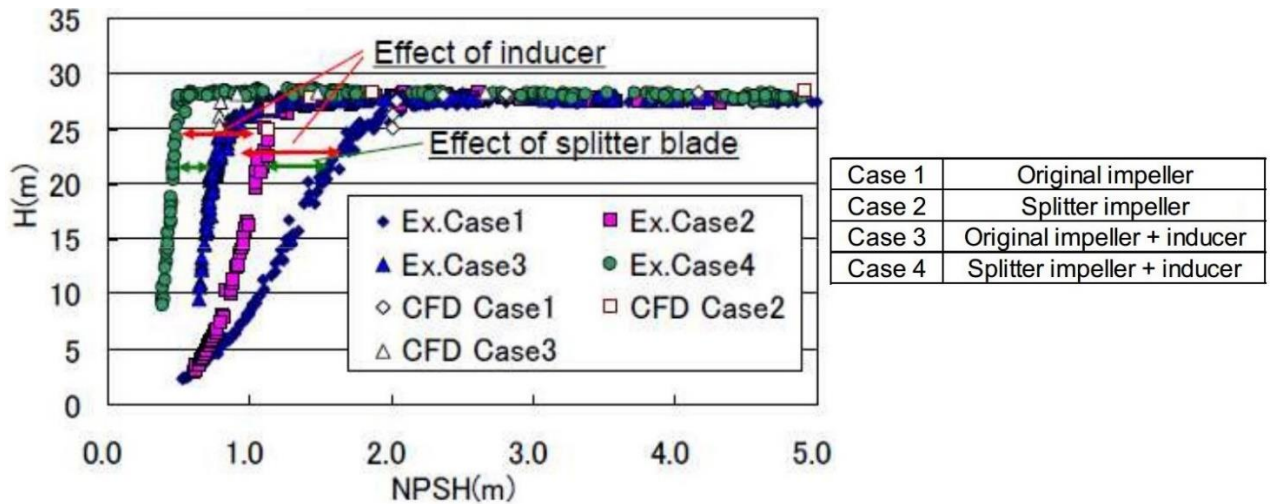


Figure 3.5: Cavitating performance of the full-length blade impeller (Case 1) and the splitted one (Case 2, the baseline of this thesis) from the OIT research. Figure from [21].

From Figure 3.5 the inducer appears to have the primary role on the performance improvement, even if the splitter blades give a noticeable contribute. In particular, Case 3 and 4 show that once the inducer is installed, hence at lower values of σ , the splitter blades positive effect is reduced.

4 Optimization Framework

4.1 Framework Overview

The optimization framework is developed using Workbench Ansys 17.1 and it consists of a multiple-steps process where the steps are the blocks shown in Figure 4.1. In the following section, their role will be explained, first giving a general overview of their content and subsequently illustrating the algorithm used for the correct execution of the optimization.

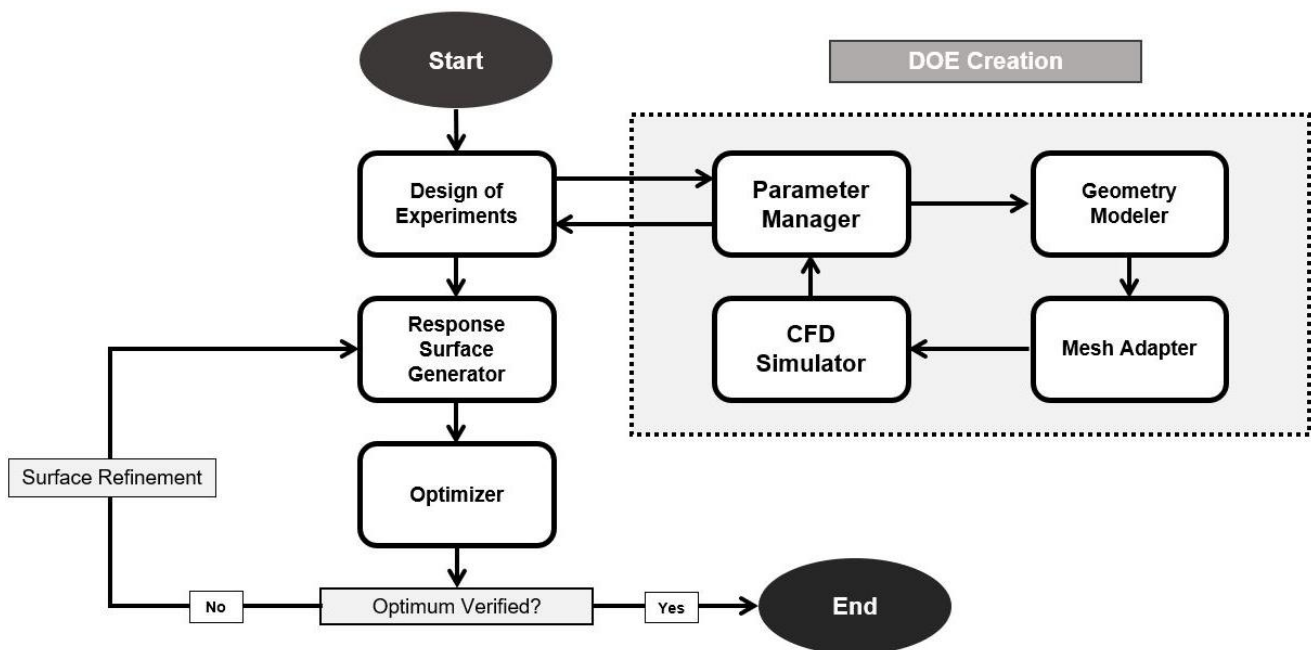


Figure 4.1: Block diagram of the optimization framework. Courtesy of Giacomo Mingardo.

4.1.1 Parametric CAD

The “Parametric CAD” block essentially refers to the parametric CAD software Design Modeler. The role of Design Modeler is to take the geometric input parameters from the Parameters Manager and to create the different impeller geometries accordingly.

In the case of this thesis, the most important aspect is the accuracy of the reconstruction of the baseline pump. To this end, Workbench contains a tool called BladeGen. BladeGen is used to model and turbomachinery components and it can be linked to Design Modeler in order to obtain CAD.

Through the “Import Wizard” function of BladeGen, a blade can be recreated by specifying hub and shroud profiles using .txt files containing coordinates.

Therefore, the baseline impeller is reconstructed by first extracting the coordinate points from the given stp files at hub and shroud for both main and splitter blades which then allows the reconstruction of the 3D shapes. The pump meridional plane is specified with .txt files containing its coordinate points, including the blade inlet and outlet. The result is represented in Figure 4.2 where the thickness and blade angle distributions can be seen on the bottom-left side of the figure and are automatically identified by BladeGen.

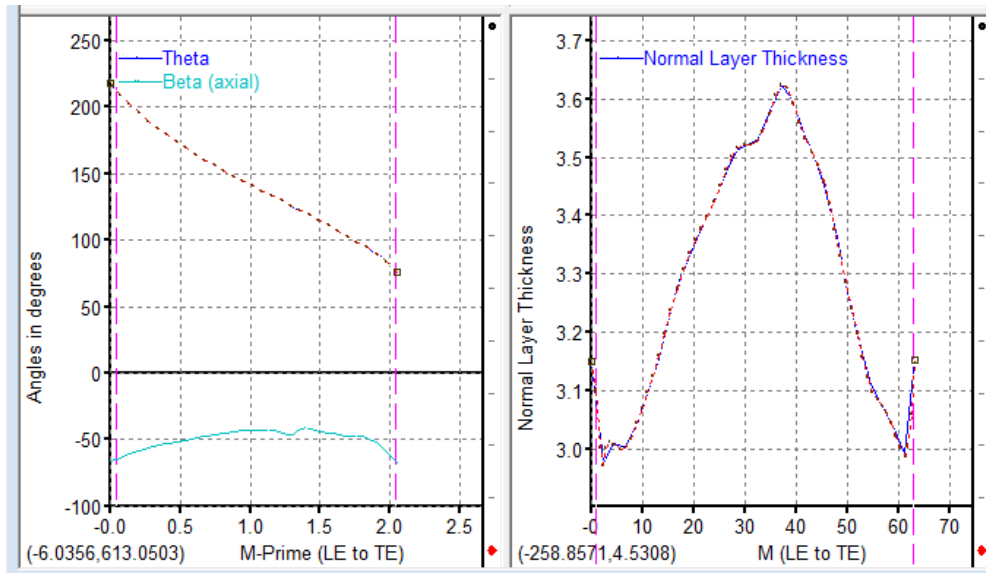


Figure 4.2: BladeGen window after the pump blades have been specified, showing beta angle and thickness distributions.

The accuracy of the model is verified against the baseline geometry file inside Design Modeler. in Figure 4.3 shows a perfect match between the models apart from a region at the splitter leading edge having a maximum error of 0.5 mm, which, however, is not influent.

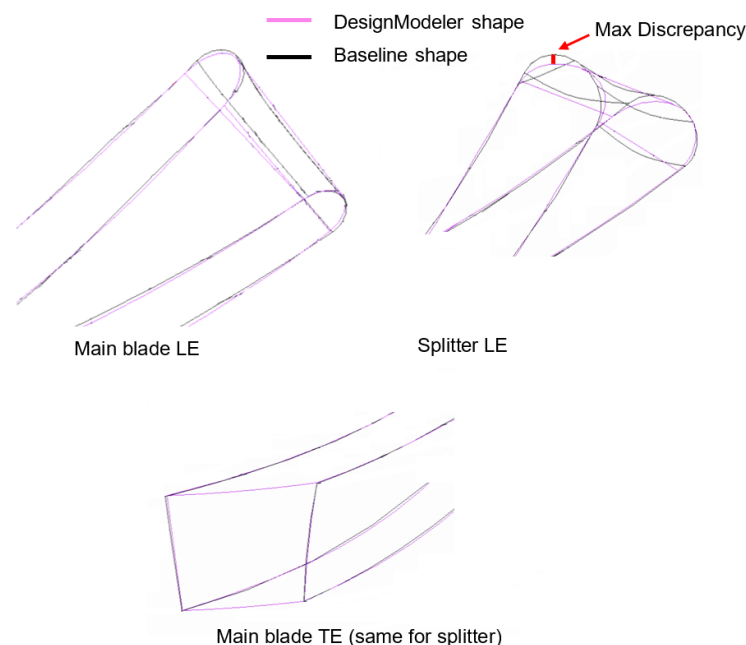


Figure 4.3: Comparison of the reconstructed blade profiles against the baseline ones. The maximum discrepancy happens at splitter blade leading edge's hub.

Design Modeler is also the software used to create the parameters which drive the optimization. Design Modeler's algorithm is able to read from the input files the different parts forming the pump impeller. Therefore, main blades and splitters are read as two different items, their profiles at several span locations can be extracted and also the meridional section of the pump is recreated. This ability from the software makes easier and faster to create parameters which can control the splitter blades shape and justifies the extra-passages through BladeGen illustrated before. Nevertheless, Design Modeler is not the most powerful CAD software, hence the freedom over parameters creation is limited compared to other tools not available within Workbench.

The input parameters, presented in Section 4.2.1, are adapted from the analysis of the geometry given by Design Modeler and, in some cases, are created by the user with the options available within the software.

4.1.2 Adaptive Mesher

Following the optimization sequence, the geometry is passed from the parametric CAD block to the mesh one to create the computational domain of the pump, which is divided into three parts: an inlet section, containing the inlet pipe and the inducer, the impeller, and the outlet section, containing the simplified volute or the complete one with the outlet pipe. In every case, only one third of the geometry is used, to reduce the computational costs of the simulations.

For the inlet, inducer and simplified outlet the software ICEM is used. It is already included within the Workbench framework and, starting from the fluid domain geometry, it allows to create structured and unstructured mesh of the desired accuracy. A structured mesh is built for the abovementioned parts given their simple geometry. To reduce as much as possible the number of cells, the inlet mesh is coarser at the beginning and it is refined as it comes closer to the inducer whereas the contrary happens in the simplified outlet part. An extra-fine mesh, Figure 4.4, is placed at the inducer tip gap to capture the flow features in that important area and all the walls are treated with a refinement to maintain the y^+ value below 10.

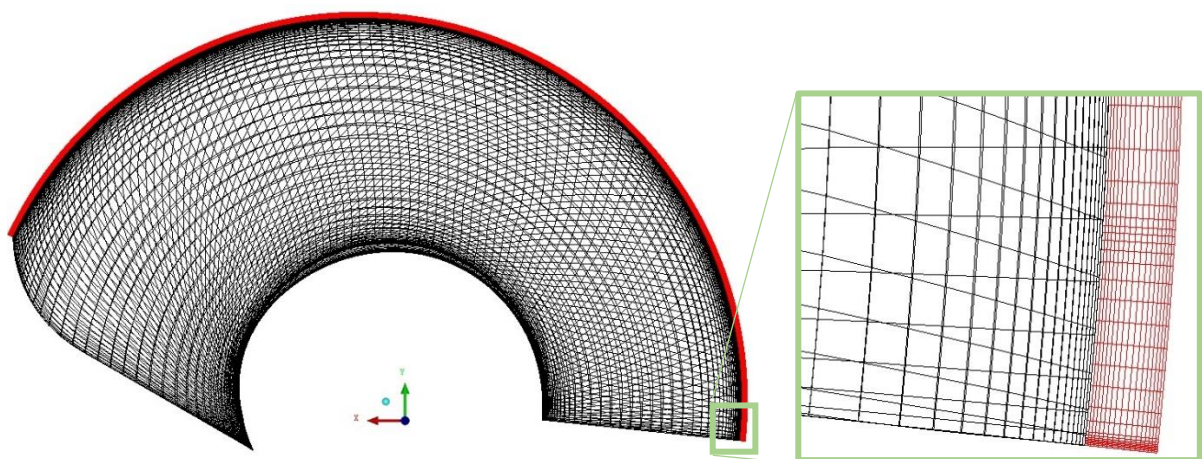


Figure 4.4: Details of the inducer tip gap mesh (in red) for one blade created with ICEM.

The computational domain of the volute shown in Figure 3.4, instead, is created using Ansys Meshing a software which automatically generates unstructured mesh from a geometry file. Even in Meshing is possible to specify an inflation layer, that is to say a wall treatment. The

use of an unstructured mesh is needed in this case because of the complex shape of the component. The outlet pipe is meshed in ICEM as an extrusion of the volute outlet plane. As for the inlet pipe, the number of cells is reduced by making an increasingly coarser mesh from the volute outlet to the actual pump outlet.

All the computational domains described above are built only once and then used for every simulation whereas, in order to adapt to the different splitter shapes, the impeller mesh is created multiple times during the optimization. To have the possibility to do so automatically during the optimization, Design Modeler is linked to TurboGrid which is capable of reading main turbomachinery features such as blades (full-length and splitter), hub and shroud profiles and to change the mesh topology accordingly. TurboGrid reveals to be a valid and flexible tool but checks over its reliability close to the design space boundaries shows that some extreme shapes are not possible to be meshed. TurboGrid automatically discards the geometry that cannot be meshed hence that are not of interest for the current work, hence making the software completely reliable for all the relevant design points.

TurboGrid adapts to the different geometries but at the same time it preserves the settings decided at the beginning. For this reason, all the meshes created have the desired quality, assessed in the initial phase of the research work through a mesh convergence analysis. The value of y^+ value, for instance, remains below 30 in the entire impeller in each case.

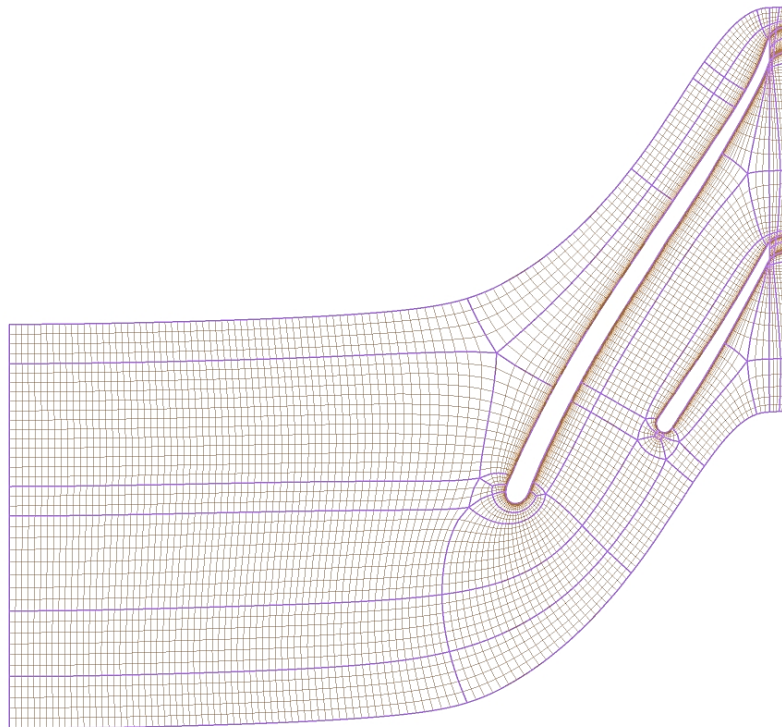


Figure 4.5: Topology and mesh at midspan as created by TurboGrid for the baseline pump.

Figure 4.5 shows the mesh at midspan as created by TurboGrid for the baseline pump. The topology set used by TurboGrid is called “ATM optimized” and it consists of a series of topologies selected by the algorithm depending on the characteristics of the geometry such as the presence of splitter blades, rounded or cut-off trailing and leading edges. For further investigation on the subject, please refer to [22].

4.1.3 Numerical Solver

All the computational domains discussed above are finally assembled together inside the numerical solver block. As explained in the previous Section, the impeller mesh is connected to the loop, hence it is automatically updated and loaded while all the other components remain unaltered from a simulation to the other, hence their meshes are kept fixed in the numerical solver block.

ANSYS CFX 17.1 is the software used for the simulations. It is made up by three parts: CFX-Pre, where the computational domains are loaded and the boundary conditions set, the actual solver and the CFX-Post, where the analysis of the results is carried on, including the creation of the optimization output parameters.

The simulation run are steady state and single passage Reynolds Average Navier-Stokes (RANS) calculations. A detailed description of the solver can be found in [22]. The computational approach is based on a finite-volume method using an implicit incompressible formulation with a second order spatial discretization. RANS calculations are closed through the two-equation $k-\omega$ shear stress transport turbulence model. The total pressure boundary condition is selected at the inlet and the mass flow rate is defined at the outlet. As it will be illustrated in more details in Section **Error! Reference source not found.4.3**, the optimization strategy includes two simulations per each design point, one in wet conditions and one with cavitation, hence, in the former case the “mass transfer” setting is disabled whereas in the latter the “cavitation” option is selected.

The multiphase flow simulations are conducted with an Eulerian formulation using a homogenous mixture of water and vapor. The mass transfer rate due to cavitation is evaluated with the Rayleigh-Plesset equation [22].

The computational domain is solved in the relative frame and comprises of three regions: inlet, impeller and outlet/volute. The upstream influence of the volute on the impeller is carefully assessed through comparison of the results of calculations with the volute and those conducted without the volute, using simplified outlet. As already mentioned, the optimizer-based calculations are then conducted without the volute to reduce the computational cost of the simulations.

A mesh convergence study has been conducted to ensure mesh-independent results for the computations. Figure 4.6 shows the static head coefficient versus mesh size. The static head coefficient oscillations are below 1% for the meshes with number of elements above 2 million, indicating mesh convergence. Therefore, a 2.8 million elements mesh is used within the optimization.

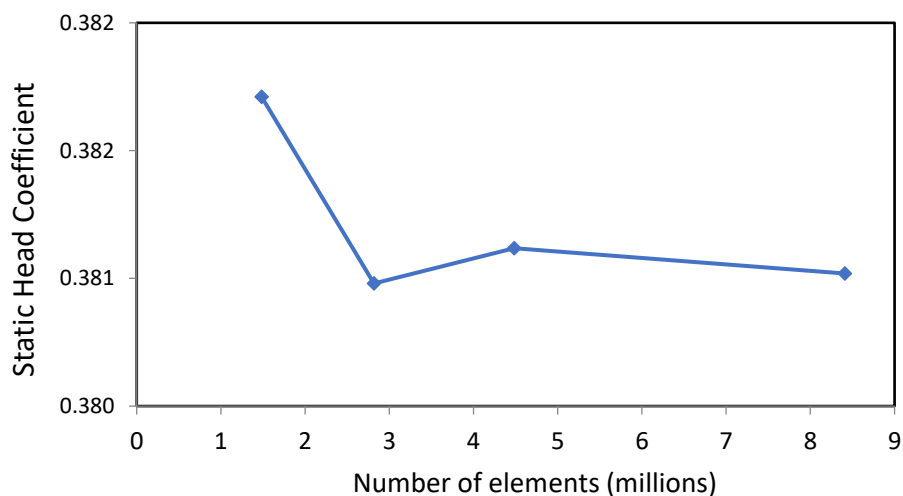


Figure 4.6: Mesh convergence study indicates 2.5 million elements are sufficient to capture pump performance

4.1.4 Optimizer

The final block of the optimization loop contains the tools needed for the actual optimization. Those are the “Design of Experiments”, the “Response Surface” and the “Optimization”. The parameters manager links the outputs of the calculations with the inputs parameters which determine those outputs. These combinations of inputs and outputs for each design point are sent to the optimizer block.

During the Design of Experiments phase the design points are generated.

With “design point” it is indicated an impeller geometry generated from a combination of input parameters. Therefore, the design points basically differ one from the other because of the shape of the splitter and all together they form the design space. During the optimization, each design point has to be numerically simulated. The algorithms available within the Design of Experiments tab allow to select combinations of input parameters which reduces the total number of design points, to save computational costs, while having a well-represented design space. The one used for this thesis will be discussed later on, in Section 4.2.2.

. At the end of all the numerical calculations, instead, the Design of Experiments box is employed to gather the output parameters of all the design points and to send the information to the second part of the optimizer block, the Response Surface.

Within the Response Surface tab, the surrogate model is created. A surrogate model or response surface, is the surface which interpolates at best the outputs from the calculations and constitutes the advantage against a direct optimization. Indeed, the optimization can be conducted, using for example gradient-based methods, on the surface, finding the optimum point without running for every step a CFD simulation. Therefore, the accuracy of the surface has a relevant influence on the optimization outcome, thus it is important to have a reliable surrogate model before trusting the optimum point. The accuracy depends on several factors, two of the most important being the accuracy of the simulations results and the choice of the surface creation algorithm. Within the Response Surface part of the Optimizer, several models are available and the selection can be made based on their characteristics as explained in [22]. The Response Surface used in this work will be illustrated in Section 4.2.2.

The last part of the Optimizer block is the actual optimization. The definition of the optimization goal and the constraints is made here. Several algorithms can be selected but mainly two kinds are to be distinguished. A first set is to be used for a preliminary overview of the design space, in order to locate the region of the global optimum discarding local minima/maxima, thus reducing the area of research of the next optimization steps. A second set can be then applied to finally find the optimum. The candidate optimum point represents a prediction of the optimization algorithm based on the surrogate-model. Therefore, it has to be simulated before it can be considered valid, in order to verify the compliance of the prediction with the actual numerical value.

4.2 Framework Setup

4.2.1 Selection of Design Parameters

During the literature review phase, a selection is done of the parameters considered the most important for splitters to limit cavitation. Circumferential position, number of splitters, their length and the blade angle distribution are all influencing parameters when dealing with cavitating suction performance. Therefore, the parameters used in this thesis derive from the abovementioned selection. Since the number of splitter blades is constrained to three by the impeller configuration, the actual parametrization modifies the splitter circumferential position and the blade angle distributions at hub and shroud.

As explained in Section 4.1.1, major efforts have been focused on creating the pump geometry using the turbomachinery tools available with Workbench.

For each single blade or splitter, at any span position, Design Modeler is able to extract the thickness distribution, the θ -angle distribution and the β -angle distribution. Each of those curves can be modified by using control points. Default points are given but they can be deleted or added and moved manually or automatically if set as input parameters. Moreover, every distribution can be transformed into a spline, a piecewise linear curve or a Bezier curve. The latter is the one chosen for this optimization due to its capability to be adjusted with only few control points, used as input parameters. This property of the Bezier curves perfectly aligns with the need of maintaining as low as possible the computational costs while keeping a satisfactory control over the splitter blade design. The thickness distribution of the splitter blades is maintained fixed to preserve the one of the baseline pump, thus the points that control it are not modified or set as parameters. For what regards the angle distribution, instead, θ and β are depending on each other, therefore the shape is to be decided based on only one of the two. Theta is the angular coordinate measured from the rotation axis using the right-hand rule, [22], while beta is the blade angle and defines the blade camber line from leading edge to trailing edge. Since beta is the most common parameter used in turbomachinery, it is selected as splitter design parameter. Therefore, the blade angle distributions at hub and shroud are parametrized using Bezier curves for the camber line as indicated in Figure 4.7. Five control points define the Bezier curves, of which two control points are at the hub and three control points at the shroud. The additional control point at the shroud defines the position of the leading edge, thus it also partially modifies the blade length. As can be seen in Figure 4.7, the points are distributed on the camber at leading edge (for the shroud camber line), at the middle of the splitter meridional length and at the trailing edge.

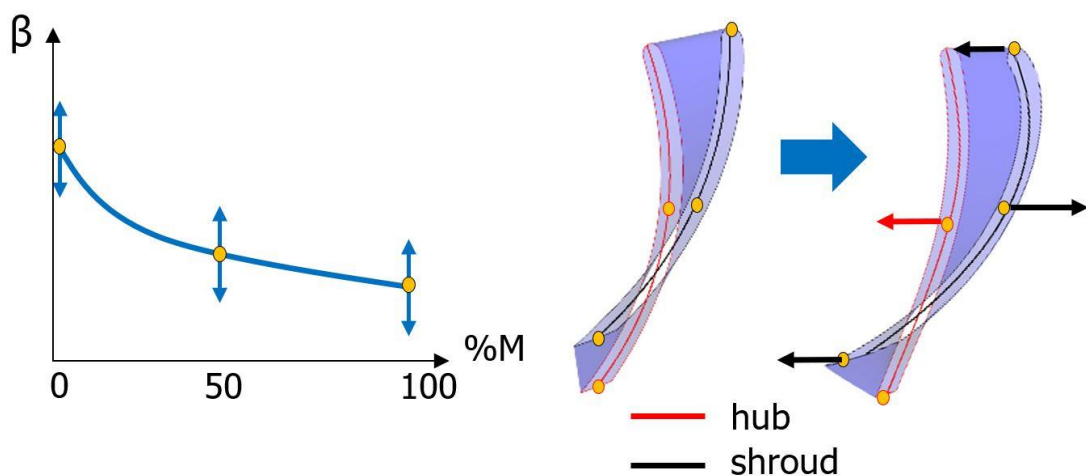


Figure 4.7: Illustration of the Bezier curves parametrization. The blade angle distribution is parametrized with three control points of the Bezier curves.

The circumferential position is the other property being parametrized. It defines the location of the splitter in the region delimited by the suction side of one main blade and the pressure side of the subsequent. The circumferential position is a property that Design Modeler can read from the baseline geometry where the value is 0.5. This means that in the baseline impeller the splitter blades lie exactly in the middle of the blade passage. The number 0.5 indicates that the splitter is 50% away from the main blade pressure side and the other main blade suction side. A percentage equal to 100% means that the splitter coincides with the main blade suction side and vice versa with 0%. Design Modeler automatically set this convention. Figure 4.8, showing, for the baseline impeller, the blade-to-blade plane at mid-span location, helps to understand the meaning of the circumferential position parameter.

Within Design Modeler, the circumferential position can be modified using just one control point located, as already mentioned, at the hub leading edge. What the software does is to determine the circumference where that point is lying and to select the part of it which stays within the blade passage. Then it divides this part into percentages and moves the leading edge depending on the input percentage. The splitter moves rigidly as illustrate by Figure 4.8.

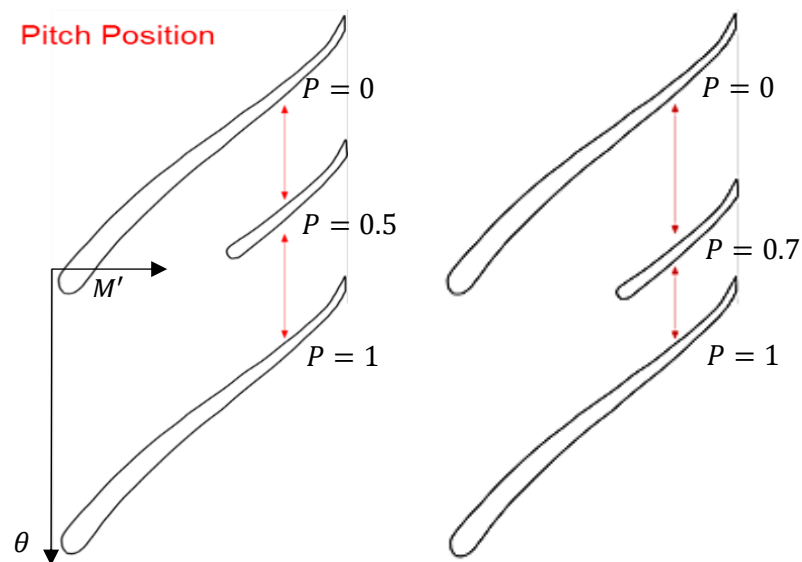


Figure 4.8: The circumferential or pitch position parameter determines the proximity of the splitter to the suction side ($p=1$) or to the pressure side ($p=0$) of the main blade.

To summarize, the six splitter design parameters used in the optimization are:

- Circumferential (or pitch) position
- Bezier control point on β distribution at hub, half of meridional length
- Bezier control point on β distribution at hub, trailing edge
- Bezier control point on β distribution at shroud, leading edge
- Bezier control point on β distribution at shroud, half of meridional length
- Bezier control point on β distribution at shroud, trailing edge

4.2.2 Optimizer Setup

The Optimal Space-Filling Design Method is chosen to create the Design of Experiments. This is a version of the Latin-Hypercube Sampling (LHS) method where iterations maximize the distance between sample points. Given n parameters and s design points, the LHS algorithm divides the range in s^n “boxes”. The points are randomly generated inside a section so that for every one-dimensional projection of the s samples, there is only one sample in each box [23]. To better illustrate the Optimal Space-Filling Method and the difference with a Latin-Hypercube Sampling algorithm, Figure 4.9 shows an example of design points generation starting from two input parameters. It can be noticed that for each parameter, none of the projections of the design points overlaps. While the overlapping is excluded from both methods, the Optimal Space-Filling presents a more homogenous distribution of design points inside the design space area thanks to the iterative optimization of the spacing between them, mentioned above. In this way the variability of the output parameters can be analyzed more precisely for the same number of design points with respect to a Latin-Hypercube Method, hence increasing the accuracy of the optimization while reducing the computational costs.

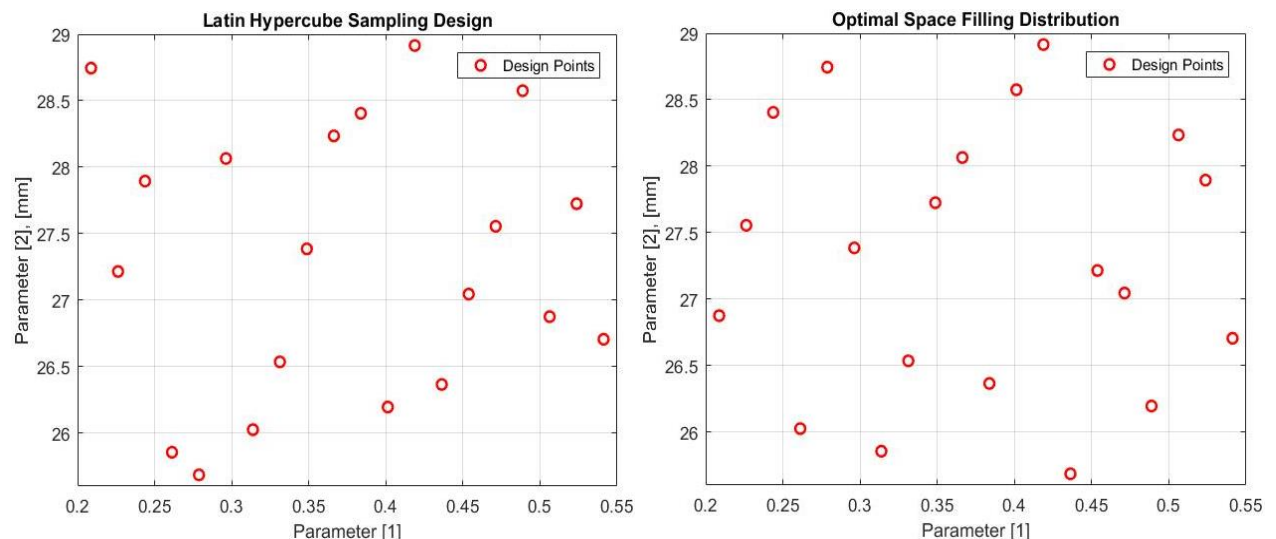


Figure 4.9: Example of how the LHS and OSFM differs when creating the design points. The plots show the distribution of design points having two input parameters.

As an initial guess, 20 design points are created which is more than twice the number of input parameters, which is a rule suggested in [22] in order to have a well-defined design space. Upper and lower bounds for each design parameter are also imposed in the Design of Experiments tab based on geometry and meshing limitations. The limits of the design space are carefully assessed to confirm that points excluded from the optimization represent unsuitable design configurations. This indicates that the limitations imposed by geometry and mesh do not influence the optimization process.

The outputs taken from the results of the CFD simulations are subsequently processed inside the Response Surface tab. Ansys Workbench gives six default response surface algorithms including, among others, standard second-order polynomial, genetic algorithm and natural neural network. Moreover, the Response Surface tab has a “Goodness of Fit” tool which summarizes the quality of the fitting using standard metrics, in order to facilitate the

choice of the method. The metrics used by this tool include the coefficient of determination R^2 , the root mean square, the relative maximum absolute error, defined, respectively, as:

$$1 - \frac{\sum_{i=1}^N (y_i - \hat{y}_i)^2}{\sum_{i=1}^N (y_i - \bar{y})^2}; \quad \sqrt{\frac{1}{N} \sum_{i=1}^N (y_i - \hat{y}_i)^2}; \quad \frac{1}{\sigma_y} \text{Max}_{i=1:N} (\text{Abs}(y_i - \hat{y}_i));$$

where \hat{y}_i is the value of the regression model at the i -th sampling point, y_i is the value of the output parameter at i -th sampling point, \bar{y} is the arithmetic mean of the values y_i , N is the number of sampling points and σ_y is the standard deviation of the values y_i .

By analyzing these metrics it is possible to exclude the algorithms, creating response surfaces that have the less accuracy in predicting the values of the sampling points. In particular, out of this analysis, the Standard Response Surface 2nd-Order Polynomial reveals to have the worst accuracy. This is due to the non-linearities present between inputs and outputs. As reported in [24], the use of parametric methods can have limitations when dealing with peaks, due to the nature of the equation used to approximate the relation between inputs and outputs over the design space. In [25], the authors express the same view stating that nonparametric approaches are typically used because a parametric model do not provide the necessary sensitivity to curvature. In this sense, the use of non-parametric methods allows the effects and interactions between inputs and outputs to vary within the design space, increasing the flexibility and adaptability of the response surface [24]. Indeed, non-parametric algorithms assume a certain amount of smoothness of the curve but do not impose a form for the curvature of the target function [25]. For this project, the Non-Parametric Regression algorithm indeed present the best values of the metrics presented before and consequently is selected as response surface method. Nevertheless, a check over the accuracy of the response surface is made for each optimum candidate point found with the optimization algorithm (discussed in the following). As already mentioned in Section 4.1.4, the control implies a CFD calculation of the candidate point in order to compute the error over the predicted output from the response surface. The latter is considered to be accurate, and its predictions to be trusted, when the error falls below 1%.

The response surface for only two of the six parameters is shown as an example in Figure 4.10.

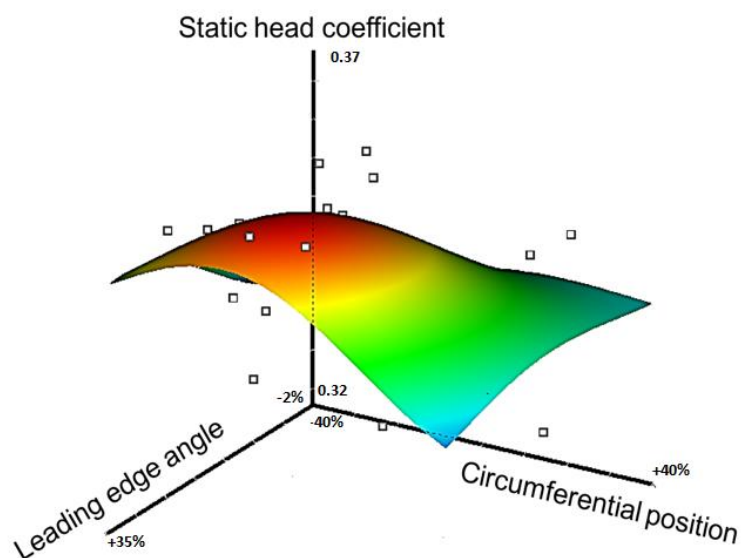


Figure 4.10: Response surface for two parameters of the optimization and the head coefficient with cavitation. The squares represent the computed output of each design point. For the leading edge and the circumferential parameters, the axis scale refers to variation from baseline values.

For the actual optimization, two methods are used. At first, the Screening method is employed over the entire design space to avoid the selection of local maxima from the optimization and to restrict the research area. Indeed, the Screening is a sampling strategy suitable for a global exploration of the domain and can be used for Multi-Objectives optimization as in this case (more details on the optimization strategy will be given in the following Section). As reported in [22], it is a Shifted Hammersley method which creates a quasi-random and uniform distribution of samples on the response surface.

At each run, three optimum candidate points are given which have to be simulated to check the accuracy of the response surface. In case the error between predictions and CFD simulations remains higher than 1%, those points are added into the design space, a new response surface is created and the Screening method is used again. For the present work, three refinement steps are done. After this process, the response surface prediction's error falls below 1%. Moreover, it is found that the region of the design space where the candidate points is found after the first optimization run does not vary throughout the entire refinement process. Therefore, as also suggested by [22], an algorithm suited for a local search of the optimum is used to refine the results in that zone. In particular, the Nonlinear Programming by Quadratic Lagrangian (NLPQL) algorithm is applied to find the global optimum. However, the NLPQL works only with single objective cases therefore in order to employ it, the second objective of the optimization, the wet head coefficient output, has been discarded. Nevertheless, being the design space already restricted to the most promising area, the removal of the goal on the wet performance has not influenced the actual wet head coefficient. Indeed, in the end the best candidate point from the last Screening method step has been confirmed as the global optimum of the optimization.

4.3 Optimization Objectives and Strategy

This work aims at improving the cavitating suction performance of the baseline pump while keeping the wet characteristic, as close as possible to the baseline one in order to obtain a comparison between baseline and optimized which is accurate and coherent, as underlined also by Cavazzini [17]. A simultaneous check over wet and cavitating performance of each design point of the optimization is needed while at the same time the number of simulations has to be maintained as low as possible to reduce the computational costs. The importance of the optimization strategy thus resides within this trade-off.

In sec. 2.1.5 the cavitating performance curve is presented in Figure 2.9. As explained, the curve presents, for a given flow coefficient, the relation between the head rise across the pump and the cavitation number σ . At a certain value of σ , the cavitation bubbles within the blade passage alter the flow field to the point that the head coefficient suddenly drops.

During ramp test, the curve is described from right to left by lowering the inlet pressure, hence from the highest cavitation number to the lowest, where the right-most values indicate a limited presence or complete absence of cavitation bubbles in the impeller. There, the head coefficient values correspond to the head coefficient at that specific flow coefficient on the wet characteristic, or head-capacity curve.

It is thus clear that a complete cavitating performance curve of a pump should be numerically computed by collecting several head coefficients from simulations run at different cavitation numbers until the drop-off is reached. It is clear that within an optimization framework where several pumps are tested, this approach would be very expensive in terms of computational time and resources.

For this thesis it is hypothesized the one simulation is sufficient to characterize the drop-off region of each design point. To satisfy this condition, it is assumed that the drop-off σ of the baseline pump can be used as a fixed simulation point. The hypothesis is made because at the point of the cavitating curve, the cavities are well developed and their interfering effect on the flow field is evident.

To be more conservative, the cavitation number of the baseline pump corresponding to a 5%, not a 3%, head coefficient drop-off is taken as simulation point. The head coefficient of each design point at that specific cavitation number is taken as output parameter. The Response Surface Optimization seeks for its maximum.

It is hypothesized that to the maximized ψ a diminution of the drop-off cavitation number will correspond, which would implicate an extension of the pump operational range under cavitation.

Figure 4.11 shows the cavitating performance assessment strategy as a knee-curve plot.

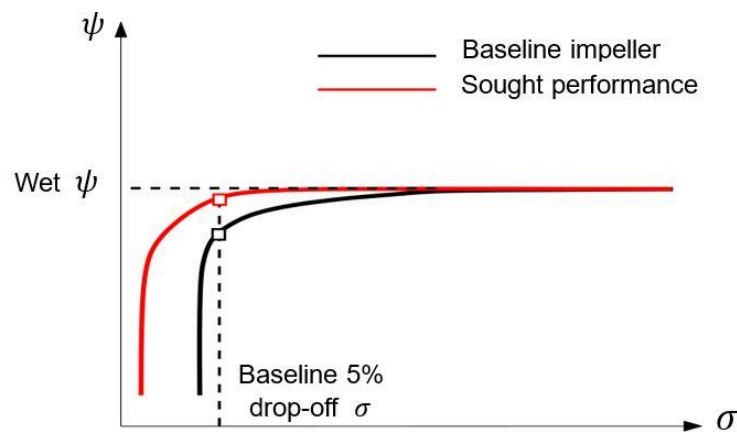


Figure 4.11: The optimization of the cavitating performance is done simulating at baseline 5% drop-off σ . The head coefficient is maximized in that condition. It is hypothesized that to increased ψ correspond lower drop-off points (red curve).

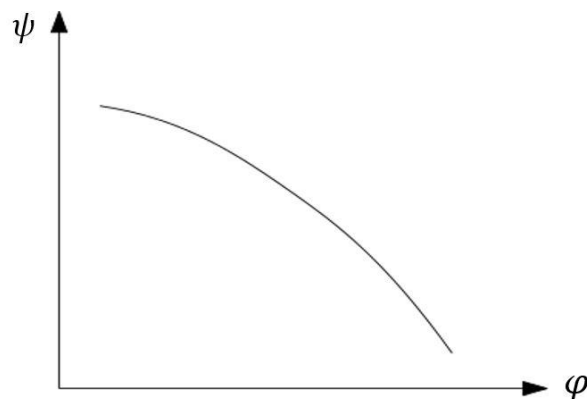


Figure 4.12: Example of a typical head-capacity curve characterizing the wet performance of a centrifugal impeller.

Figure 4.12 presents the typical curve characterizing the wet performance of a centrifugal impeller. To be able to compare two pumps, the baseline and the optimized, they need to have a wet characteristic as much as possible equal, following Cavazzini [17], thus a constraint must be applied on the head-capacity curve of each design point. In the same way as for the cavitation characteristic, it is too much computationally expensive to simulate several flow coefficients to reconstruct the head-capacity curve of each design point.

Consequently, in this project only the 100% baseline design flow coefficient is run for each design point, the same value of the cavitation performance simulations.

Therefore, for each geometry a value of the wet head coefficient is available and, within the Optimization tab, a constraint is posed on it to have ψ equal or 5% greater than the baseline one. The upper margin is chosen in order to not exclude a priori designs with improved cavitating and wet performance.

Using this strategy, the research of the optimum splitter is limited to those shapes which increase the head coefficient in cavitating condition without altering, or at least without lowering, the baseline wet performance. In symbols it can be summarize as follows:

$$\text{maximize } \psi_{cav}(x_1, x_2, \dots, x_n)$$

subject to:

$$\begin{aligned} \psi_{wet}(x_1, x_2, \dots, x_n) &> 99\% \psi_{wet_baseline} \\ \psi_{wet}(x_1, x_2, \dots, x_n) &< 105\% \psi_{wet_baseline} \end{aligned}$$

where n is the number of design parameters.

5 Optimized Design Assessment

The present chapter illustrates the results of the optimization, analyzing the main features of the optimum splitter blade. To find the optimum the screening algorithm is used three times, for a total of 9 optimum candidate points, until the response surface reaches the desired accuracy. When the response surface predictions' error is lower than 1%, the research of the optimum is restricted to the area of the best candidate and the NLPQL is applied. The algorithm confirms the best candidate found with the screening method. Out of nine candidate points, four of them are repeated, therefore the total number of points simulated is equal to 25. The accuracy of the refined response surface at the optimum point is 0.13% for the wet head coefficient and 0.12% for the cavitating head coefficient, corroborating the response surface predictions.

5.1 Optimal Splitter Blade Shape

The percentage variations of each design parameter are presented in Table 5-1. The percentages are calculated relative to the reference values.

Therefore, the circumferential position indicates that the optimized splitter is 5% closer to main blade pressure side, while the control points show the increase or decrease of the blade angles in the optimum configuration compared to the reference geometry, accordingly to sec. 4.2.1.

Table 5-1: Parameters variation to obtain the optimal shape

Parameter	Variation w.r.t. baseline
Circumferential position	-5.1%
Hub	
Control point 1 (midpoint)	+7.68%
Control point 2 (TE)	+65.8%
Shroud	
Control point 1 (LE)	-6%
Control point 2 (midpoint)	+14%
Control point 3 (TE)	+35%

The optimized splitter being located closer to the main blade pressure side compared to the baseline geometry is in contrast with what found in some previous researches, [26], where it is reported that a splitter closer to the suction surface of the main blade improves the pump suction performance. Indeed, within the current optimization it is noticed that splitters located closer to main blade suction side generate higher wet head coefficients compared to the baseline geometry, however, the same geometries are those having the lowest cavitating head coefficients. The contrary is found for splitters positioned closer to the main blade pressure side. Their wet head coefficients are lower compared to the baseline pump, but their cavitating

head coefficients are higher. Therefore, the circumferential position has an opposite influence on the optimization objective function ψ_{cav} and on the parameter subjected to the constraints, ψ_{wet} .

These observations also explain the great variations in relative position of the two blade angles at trailing edge, both increased substantially. Being the relation between the objective function and the constrained parameter conflictual with the variation of the circumferential parameter, the blade angle distributions make possible the trade-off to obtain improved cavitating performance while having satisfied the constraints.

Indeed, the outlet blade angle of a turbomachine is one of the parameters determining the machine work output. The role of the outlet angle in the optimum design will be further analyzed in Section 6.

Figure 5.1 illustrates a visual representation of the splitter blades profiles at hub and shroud, before and after the optimization, where the effects of the variations presented in Table 5-1 can be observed.

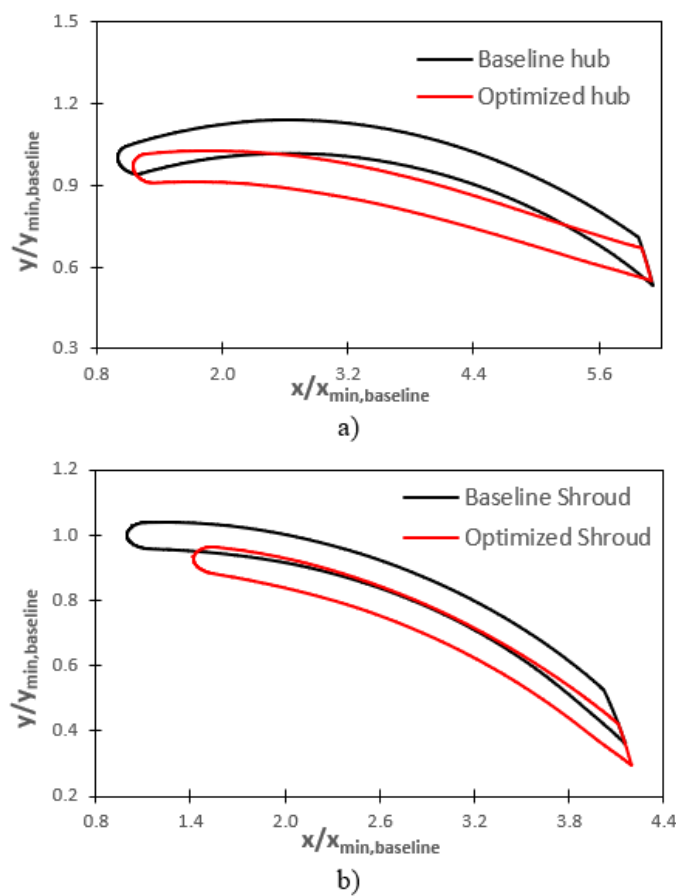


Figure 5.1: Comparison of the hub and shroud profiles of the baseline and optimized splitter blades.

5.2 Experimental Validation

The performance of the optimized design is assessed with numerical calculations and experimental testing.

5.2.1 Test Rig

The experimental data have been obtained at the close-loop test rig of the Fluidmachinery Laboratory of the Osaka Institute of Technology, Figure 5.2.

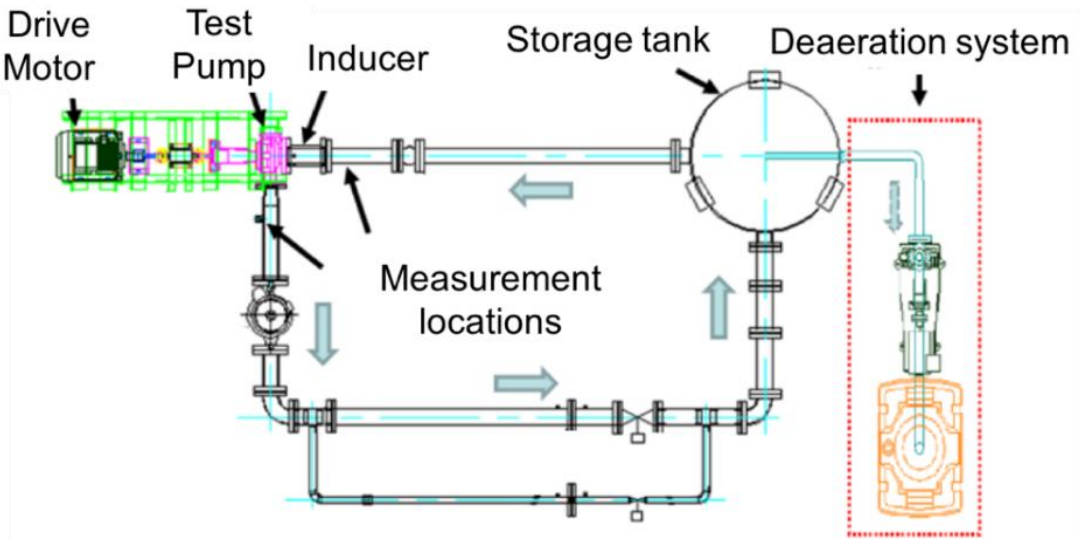


Figure 5.2: Scheme of the closed-loop test facility of the OIT.

The data acquisition system consists of static and dynamic pressure transducers in various locations, one positioned 3 diameters upstream of the pump inlet, and differential pressure transducers measuring at both inlet and 4 diameters downstream of the outlet.

Sampling time can be regulated in order to avoid excessive data dispersion especially in the region of cavitation breakdown.

The flow coefficient is set by means of a throttling valve positioned downstream of the pump.

Referring to Figure 5.2, the wet experiments are conducted by letting the water flow out of the tank into a flow conditioning section, through the test section, and through the throttling valve before returning to the tank. The wet performance curve is obtained, at fixed rpm of the drive motor, by changing the opening area of the throttling valve to span different flow coefficients while registering the pressure rise across with the data acquisition system.

For the cavitation experiments a vacuum pump is used ahead of each test run to deaerate the water and, in order to remove the remaining air nuclei from the test rig, the water is recirculated for one hour before the actual start of the cavitation test.

The experimental cavitating curve is drawn starting from the lowest cavitation number, hence first acquiring the cavitation breakdown condition. Then the inlet pressure is gradually increased until wet conditions are reached.

5.2.2 Pump Manufacturing

The baseline and optimized pump are built through rapid prototyping technology, more specifically using 3D printers for the ABS+ polymer (Figure 5.3). The height of the layers, the density of the supporting structure and the thermal control are selected in order to obtain an acceptable level of surface roughness and dimension tolerance.



Figure 5.3: Optimized pump as reconstructed by 3D printing at the Osaka Institute of Technology.

One of the most important aspect to consider when using polymer 3D printing techniques are the thermal stresses on the component. Indeed, if the printing area is not sufficiently heated, during the cooling phase of the layer, the material will tend to retract causing deformations. The imperfections can be evident, hence determining the elimination of the piece as waste or they can be more difficult to notice but anyway potentially harmful for the experiments. To avoid this problem, every important feature of each component used for the tests is measured multiple times with a caliper to verify the dimensions accuracy and uniformity.

The results are presented in Table 5-2, Table 5-3 and Table 5-4. The dimensions definition is presented in Figure 5.4 and Figure 5.5. For the inducer, the thickness of the trailing edge, Figure 5.4b, the thickness of the leading edge, Figure 5.4d, and the hub diameters are measured as well as the diameter tip-to-tip, Figure 5.4a and c.

For what regards the impeller, the shrouded configuration and the relatively small dimensions, make impossible the measurement of the blade thickness with a caliper. Nevertheless, the length and thickness of the most significant features are measured, Figure 5.5a, together with the external diameters, Figure 5.5b.

Assessing the correct dimensioning of the components is important to make a solid comparison between experimental data and numerical calculations. Being the inducer and impeller geometries the determining factor of the pump performance, before proceeding to the experimental tests it is necessary to verify that the manufacturing process has been successful in reproducing their main features.

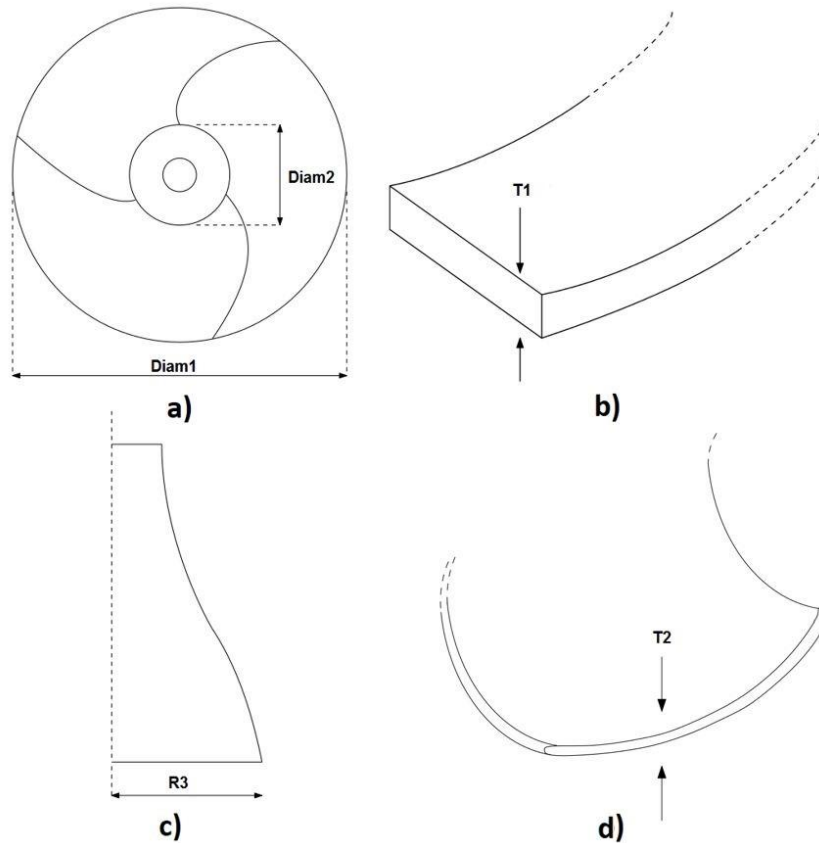


Figure 5.4: Definition of the inducer measured dimensions. View a) illustrates the inducer from the inlet, view b) the trailing edge thickness and view c) the hub outlet radius. In place of the radius R3 the diameter, Diam3, is actually measured.

Table 5-2 presents the results of ten measurements for the five inducer features described in Figure 5.4. The ten measurements refer to different locations of the same feature to check the overall uniformity of the pieces. Data from Table 5-2 are in agreement with the inducer CAD model and it can be also noticed that the components present a high uniformity, highlighted by the values of the standard deviation.

Table 5-2: Inducer measurements

n°	$Diam1[mm]$	$Diam2[mm]$	$Diam3[mm]$	$Tick1[mm]$	$Tick2[mm]$
	66.65	19.65	31.9	2.75	1.4
	66.4	19.8	31.75	2.75	1.4
	66.5	19.85	32	2.75	1.4
	66.5	19.9	31.8	2.75	1.4
	66.5	19.7	31.8	2.75	1.35
	66.6	20	31.9	2.75	1.4
	66.5	19.75	31.85	2.75	1.4
	66.55	20	31.8	2.75	1.45
	66.45	19.7	31.8	2.75	1.45
	66.5	19.9	31.9	2.75	1.45
<i>average</i>	66.515	19.825	31.85	2.75	1.41
<i>std. dev.</i>	0.0673	0.1188	0.0707	0	0.03

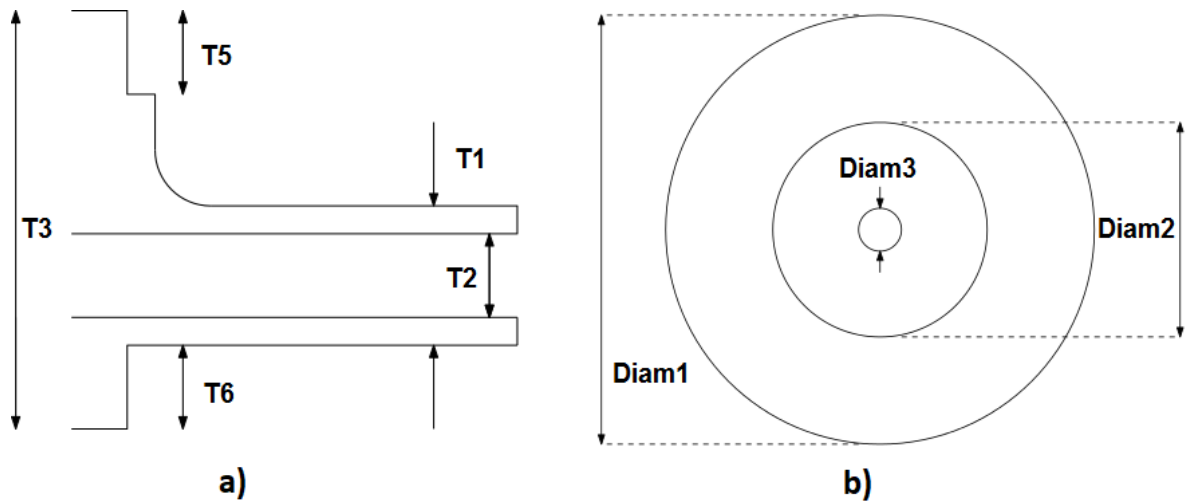


Figure 5.5: Definition of the dimensions measured in the baseline and optimized impellers. View a) shows the impeller from a side highlighting the outlet section (T2 and T1) whereas b) is a view from the upstream section of the pump.

Table 5-3: Baseline impeller measurements

n°	$Diam1[mm]$	$Diam2[mm]$	$Diam3[mm]$	$Tick1[mm]$	$Tick2[mm]$	$Tick3[mm]$	$Tick5[mm]$	$Tick6[mm]$	$Diam3[mm]$
133.2	80	80	32.4	15.8	9.55	45.75	9.4	9.05	79.95
133.1	80	80	32.45	15.75	9.6	45.5	9.55	9.1	79.95
133.2	80.1	80.1	32.25	16.05	9.6	45.5	9.5	9	80
133	80.05	80.05	32.5	15.75	9.6	45.75	9.55	8.95	80
133	80.05	80.05	32.1	15.85	9.5	45.6	9.65	9	79.9
133.2	80	80	32.35	15.8	9.45	45.55	9.5	9.1	79.9
133.1	79.95	79.95	32.2	15.85	9.65	45.5	9.55	8.95	79.95
133.05	80.05	80.05	32.15	15.8	9.55	45.7	9.5	9.05	79.9
133.05	80	80	32.2	15.95	9.45	45.55	9.6	9.05	79.9
133.1	80.1	80.1	32.4	15.85	9.6	45.75	9.7	9.1	79.9
<i>average</i>	133.1	80.03	32.3	15.845	9.555	45.615	9.55	9.035	79.935
<i>std. dev.</i>	0.07416	0.0458	0.1304	0.08789	0.065	0.105	0.0806	0.055	0.03905

Table 5-4: Optimized impeller measurements

n°	$Diam1[mm]$	$Diam2[mm]$	$Diam3[mm]$	$Tick1[mm]$	$Tick2[mm]$	$Tick3[mm]$	$Tick5[mm]$	$Tick6[mm]$	$Diam3[mm]$
133.3	80.05	80.05	32.4	15.85	9.5	45.2	9.2	9	80.05
133.3	80	80	32.4	15.6	9.65	45.45	9.35	9.1	80.1
133.25	80.05	80.05	32.45	15.8	9.65	45.4	9.2	9	79.95
133.25	80.1	80.1	32.6	15.9	9.55	45.35	9.25	9.05	80
133.3	79.95	79.95	32.35	15.75	9.65	45.3	9.35	9	80
133.15	80.05	80.05	32.45	15.75	9.65	45.25	9.4	9.05	80.05
133.3	79.95	79.95	32.6	15.8	9.6	45.3	9.2	9	79.95
133.15	80	80	32.4	15.9	9.65	45.3	9.25	9	80
133.3	80.05	80.05	32.45	15.8	9.7	45.4	9.2	9.1	80.1
133.2	80	80	32.3	15.8	9.65	45.25	9.25	9.05	80
<i>average</i>	133.25	80.02	32.44	15.795	9.625	45.32	9.265	9.035	80.02
<i>std. dev.</i>	0.05916	0.04583	0.09165	0.0820	0.0559	0.0748	0.07089	0.03905	0.05099

The average values of Table 5-3 and Table 5-4 are in agreement with each other showing a maximum discrepancy of 2.9% for “Tick5”, which anyway does not affect the experiments, hence the averages respect the CAD models. Moreover, the contained deviations for both the impellers reveal the uniformity of the geometries and the reliability of the manufacturing process.

5.2.3 Validation Results

Figure 5.6 presents the wet performance of both baseline and optimized impellers. Numerical calculations, computed using the volute illustrated in Figure 3.3b and Figure 3.4, show larger head coefficients compared to the experiments.

The deltas shown in Figure 5.6. are computed as $\psi_{CFD} - \psi_{EXP}$. From the analysis of their trends it appears that the numerical overestimation is a constant off-set along the considered flow coefficients regime, with only a minor increase of $\Delta\psi = 0.02$ for the optimized case around $\phi/\phi_{design} = 1.4$, therefore at high flow rates. It is also possible to notice that being very close, the delta trends show an existing consistency between the baseline and the optimized geometry data. The coherence of the baseline and optimized trends is of fundamental importance. Indeed, the coherence means that the simulations correctly capture the fundamental physics of the problem, thus validating the numerical framework. The constant off-set then can be scaled to obtain the values from the experiments.

Moreover, it is known from previous studies, [27], that CFD usually underestimates losses in pumps. Juckelandt et al. [27], for instance, study the effect of smooth and rough walls on pump performance prediction and find that the major loss contributions derive from the volute and the impeller side chambers flow. The latter where not included in the present work, to simplify the geometry. Moreover, the calculations do not include the leakage path in the impeller and therefore do not account for the leakage and windage losses. These two contributions are important because the flow exiting those passages is a low energy flow which interacts with the through-flow causing exchange of momentum hence hydrodynamic losses.

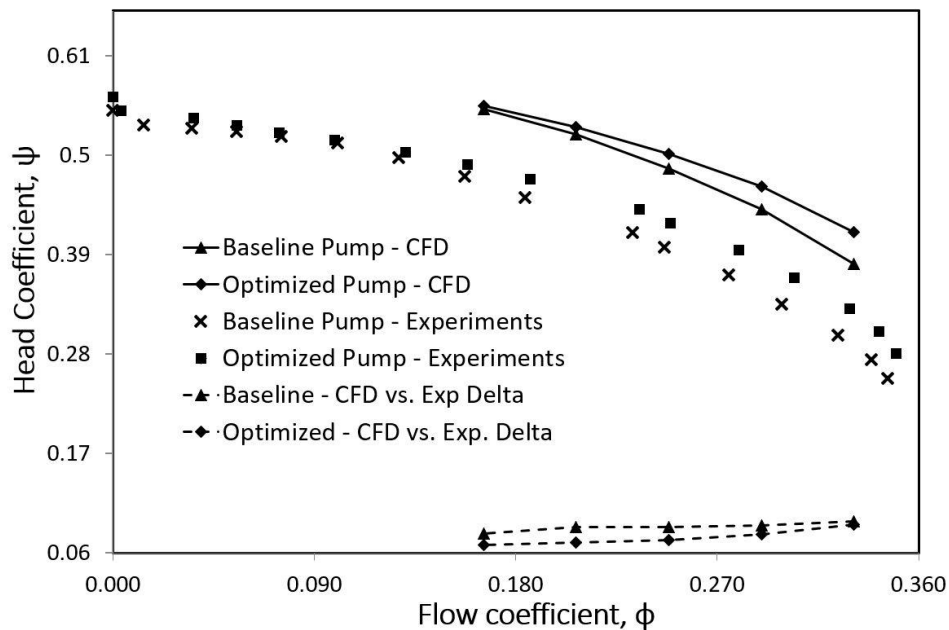


Figure 5.6: Wet performance comparison between experiments and computations. A constant offset is present between the baseline and optimized design, validating the optimization framework.

From Figure 5.6, it can be also noticed that the constraint over the head-capacity curve is effective especially around the design flow coefficient, $\varphi = 0.207$, or at lower values. At design flow coefficient, the optimized pump head coefficient is 1.5% higher than the one from the baseline pump.

Figure 5.7 shows the measured and computed pump cavitating performance. The experiments confirm the extension of the operational range under cavitation for the impeller containing the optimized splitter blades.

The calculations, however, underestimate the head drop-off point by 10% and indicate a smaller performance improvement compared to the test-rig measurements. There is also a difference in the slope of the curves at cavitation breakdown that can be due to the approximation introduced by the time-averaged RANS equations used in the simulations in a region where, as mentioned, the flow is highly non-stationary.

The experimental curves of Figure 5.7 are the results of ten separate experiments, five for the baseline pump and five for the optimized geometry, and they show high dispersion of the data. The reasons for the variability are intrinsic to the non-stationary flow field condition at cavitation drop-off, resulting into an unstable head coefficient output. Considering the dispersion of the data and the numerical approximations, including the use of the simplified outlet and the one passage simulation, it can be said that, similarly to the wetted performance measurements, the differences in performance are coherent between baseline and optimized pump and the numerical computations are confirmed.

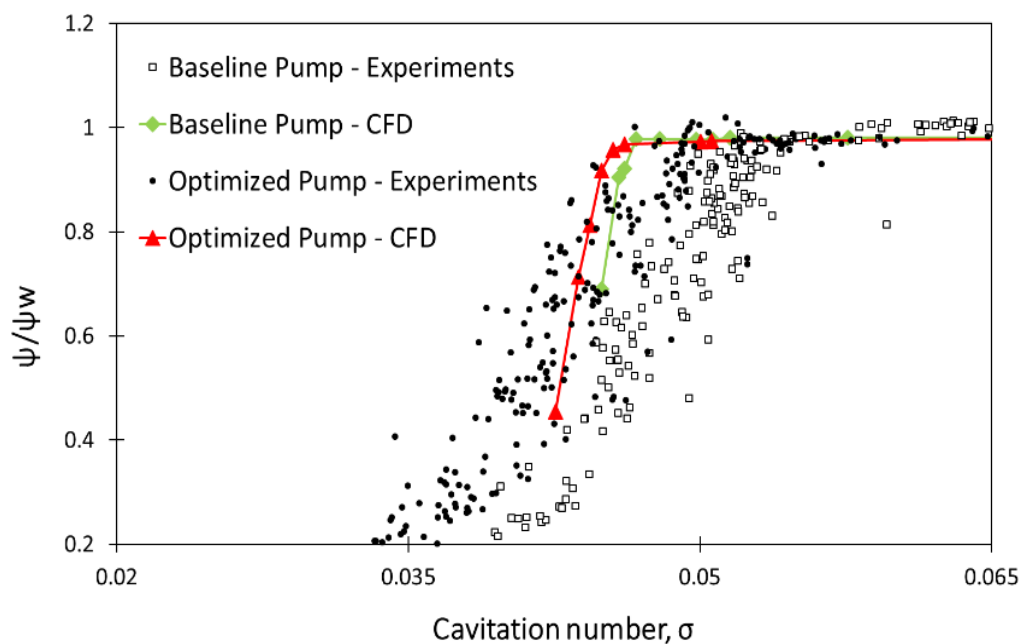


Figure 5.7: Cavitating performance comparison between experiments and computations. Experimental measurements indicate a larger improvement of operating range than computations.

Figure 5.8 is also a clear confirmation of the hypotheses formulated in Section 4.3: the optimized pump yields a 5.3% increase in head rise coefficient at the optimized cavitation number which eventually leads to a 2.2% reduced drop-off cavitation number or, alternatively, to a 2.2% extension of the operative range with cavitation.

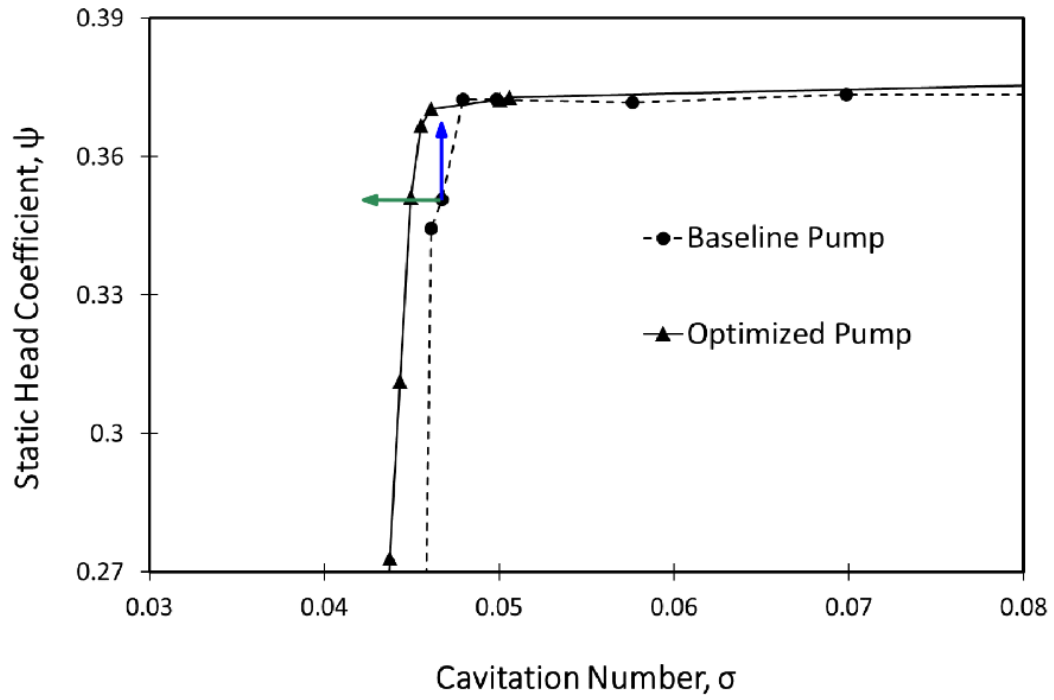


Figure 5.8: Simulated cavitating performance, comparison between optimized and baseline pumps. The head coefficient increase (blue arrow) at the optimized cavitation number generates an extension of the operative range (green arrow).

6 Characterization of the Performance Gain

6.1 Cavitation analysis

Figure 6.1 presents the comparison of cavity size between baseline and optimized geometries.

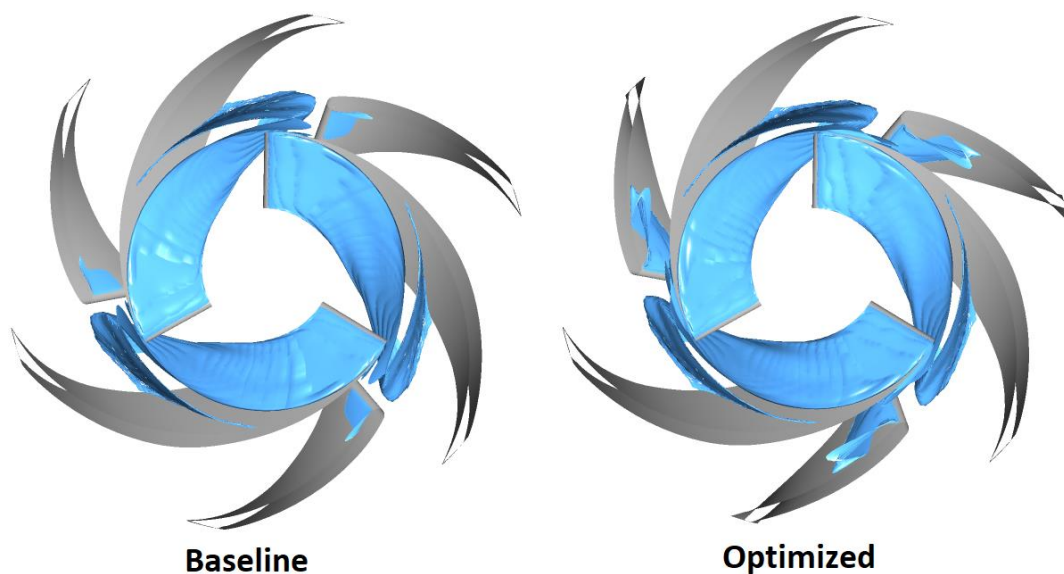


Figure 6.1: Comparison of 1% vapour volume fraction isosurface between baseline and optimized designs.

The isosurfaces are taken, in both cases, at the optimized cavitation number, corresponding to a 5% drop of the head coefficient for the baseline geometry. It is therefore expected to find an extended blade cavity. The bubble formed on the main blade suction side, extends up to the impeller inlet throat, causing a major depletion of the pressure rise. The mechanism leading to the increased losses is to be found in what discussed in sec. 2.1.4., the exchange of momentum between vapour cavities and through-flow. The extension of the blade cavity is similar also in the optimized case, which, however, does not show the same reduction of performance and, instead, shows an increased cavity size at the leading edge of the splitter close to shroud. The overall amount of cavitation present in the impeller is, however, slightly diminished in the optimized case (-0.38%, equal to a reduction of 0.023 cm^3) due to a reduction of the cavity on the main blade suction side.

Nevertheless, it appears that cavity reduction does not represent the main cause of the cavitating performance improvement.

The key role of a splitter blade, indeed, is considered in literature to be the reduction of the blade blockage at the impeller inlet thus reducing over-speeds at the main blades leading edge, consequently increasing the minimum pressure in that region hence diminishing the extension of cavities. The addition of splitter blades to a full-length blades configuration has therefore an evident effect on the blade cavity from the main blade suction side, reducing its

size. The OIT research, which led to the current baseline impeller represents a clear example with Figure 3.5 showing major reductions of the critical cavitation number, up to 70%.

6.2 Flow field analysis

As reported by Brennen [2], total pressure represents, for an incompressible fluid, the total mechanical energy per unit volume of fluid. The total pressure difference across the pump gives a fundamental measure of the mechanical energy imparted to the fluid. It can be, therefore, useful to look at the development of the total pressure rise within the impeller, with the goal of finding indications on the mechanism leading to the improvement of performance for the optimized pump.

The averaged streamwise distributions of total pressure, normalized with the maximum value, are shown in Figure 6.3. The distributions are obtained as a circumferential average by mass at constant streamwise position. The procedure is a standard of CFX “Inlet to Outlet Turbo Charts”. The inlet to outlet line of the impeller is streamwise divided into points accordingly to the sampling number indicated. For each point, the mass flow averaged is taken on areas of constant streamwise location. For this study, 285 sampling points have been used to obtain the desired accuracy.

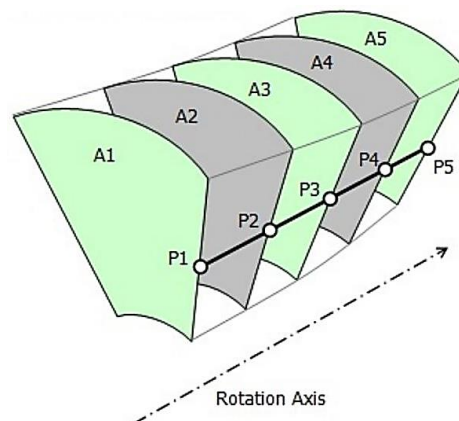


Figure 6.2: Explanation of the circumferential average by mass performed by CFX Inlet to Outlet Turbo Chart. Image from [22].

Total pressure losses from Figure 6.3 are larger for the optimized design in the first part of the passage and up to about 60% of streamwise coordinate. However, the presence of the optimized splitter blades reduces losses leading to a net increase in total pressure of 5% at the exit of the component.

The distributions presented in Figure 6.3, identify a streamline position, approximately coincident with the optimized splitter leading edge, where the trend of total pressure changes and the optimized impeller recovers the gap with the baseline geometry.

In order to understand the performance gain of the optimized pump, it is necessary to clarify where and why the recover happens. To this end, the hub and shroud regions are investigated.

Figure 6.4 presents the total pressure distribution along a streamline placed close to hub between main blade pressure side and splitter blade suction side, while Figure 6.5 compares the total pressure distributions along a streamline at the shroud for both baseline and optimized impellers.

The comparison of the two figures highlights different trends at hub and shroud. In the latter case, the baseline and optimized total pressure distributions are one on top of the other for the entire length of the splitter blade.

The total pressure distributions along the hub streamlines, instead, present a trend similar to that found in Figure 6.3. The similarity lies in the optimized distribution. The total pressure recovers to the level of the baseline impeller and then it outperforms it in the same way it does

for the averaged plot. This indicates that the mechanism driving the optimized impeller's improved performance can reside in the hub region, which is therefore further analyzed.

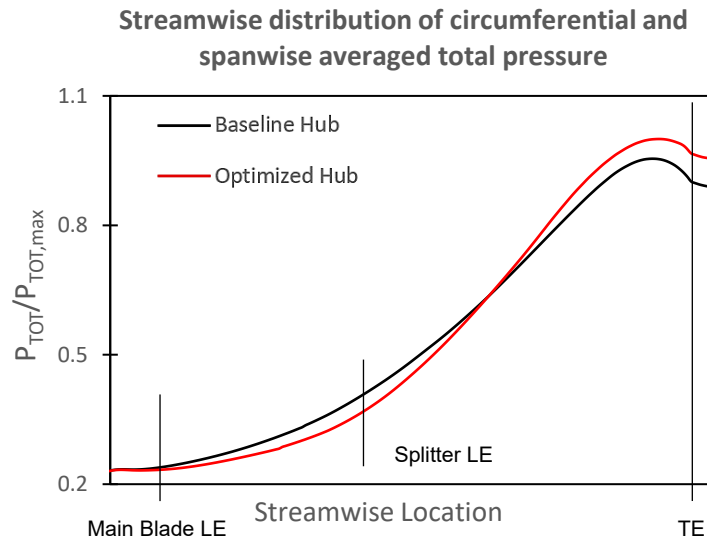


Figure 6.3: The optimized impeller starts to outperform the baseline impeller starting approximately from the splitter LE.

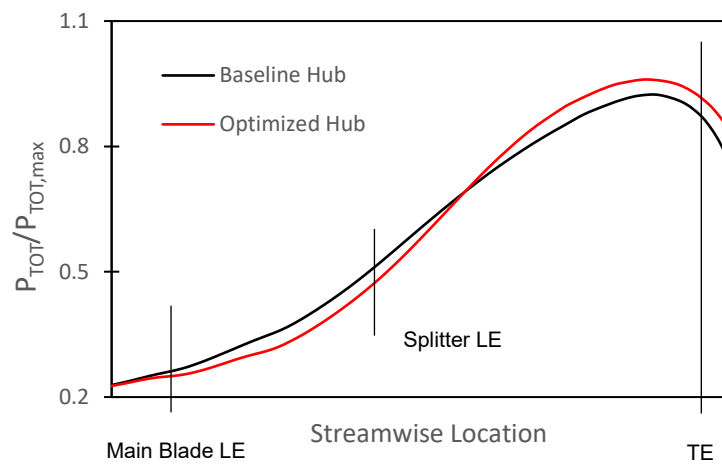


Figure 6.4: Total pressure distribution along a streamline close to hub. The trend is similar to the streamwise averaged of Figure 6.3.

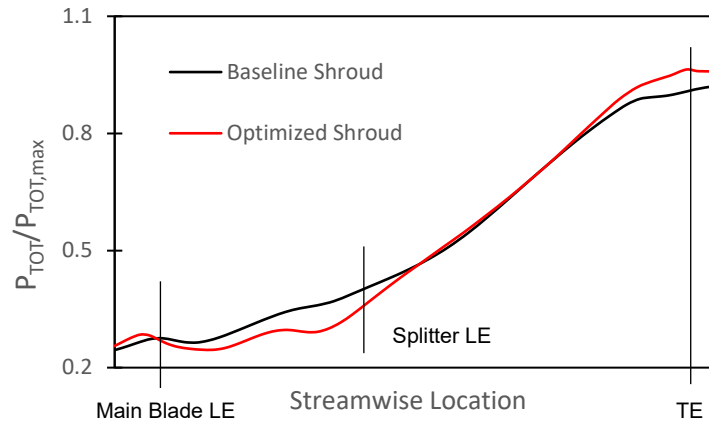


Figure 6.5: Total pressure distribution along a streamline close to shroud. The optimized impeller performs as the baseline one almost throughout the entire passage.

Focusing on the region previously identified, the flow field highlights the presence of a zone of separated flow close to main blade pressure side in the baseline impeller. The optimized splitter shape removes the separation in that region as shown by Figure 6.6 and Figure 6.7.

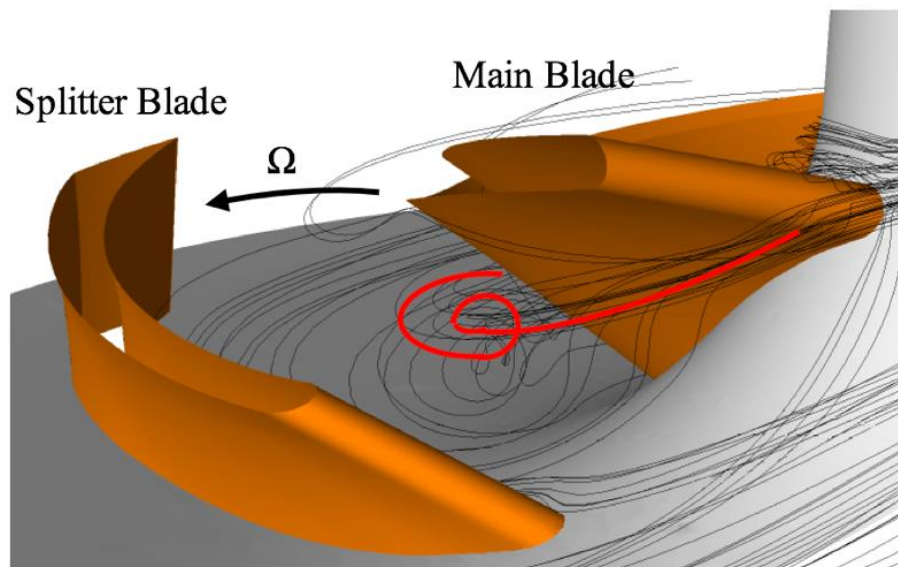


Figure 6.6: View from the impeller inlet of the baseline case. Streamlines departing from the leading edge separate from the wall after few fractions of the main blade meridional length.

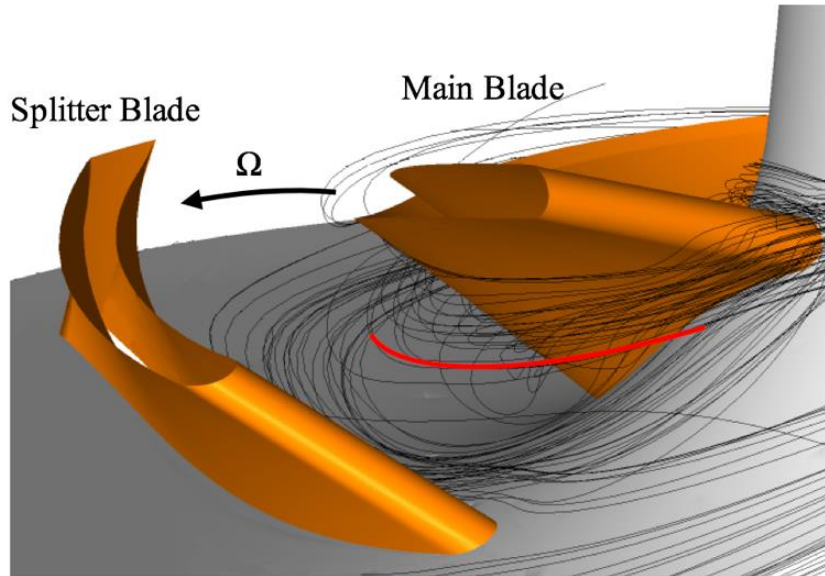


Figure 6.7: View from the impeller inlet of the optimized case. Streamlines departing from the leading edge, smoothly follow the main blade pressure surface.

Flow separation is found in this region mainly caused by the interaction of the body forces acting in the blade passage. This influence is further explained. A fluid element at a given point along a streamline is subjected to several body forces. A schematic representation of the different contributions is given in Figure 6.8.

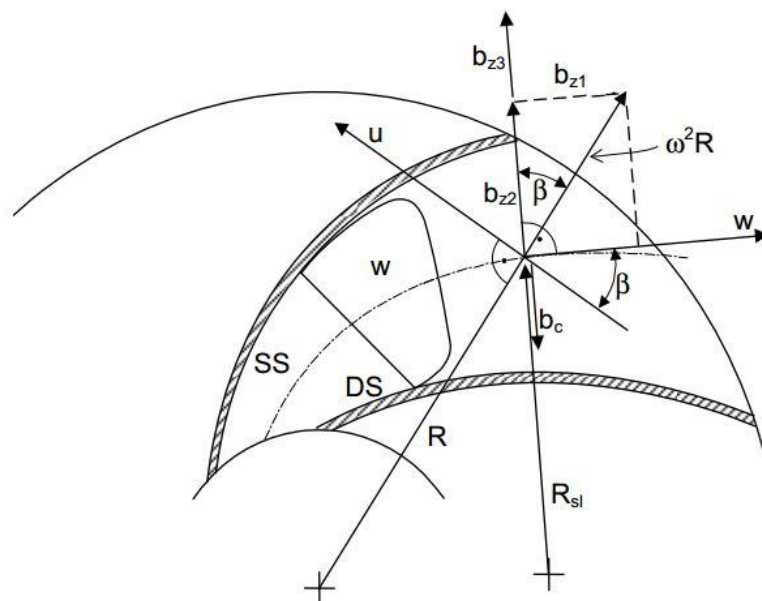


Figure 6.8: Body forces acting on a particle of fluid at a given point along a streamline. Figure from [3].

In Figure 6.8 the body forces are named in the following way: b_{z1} and b_{z2} are the component of the centrifugal acceleration acting in the direction of w and normal to w respectively, b_{z3} is the acceleration due to streamline curvature and b_c is the Coriolis acceleration. The blade pressure side is indicated DS and R_{sl} defines the local radius of the curved path. Those accelerations which are perpendicular to the direction of the flow are the most influencing on creating secondary flow in the blade-to-blade direction. When the Coriolis force predominates over the b_{z2} and b_{z3} contributions, the flow is deflected towards the pressure side of the blade. To satisfy the continuity, it then flows back to the

suctions side, creating a Coriolis induced secondary flow. Figure 6.9, referring to a simple rotating quadratic section, is useful to understand the behavior of the described secondary flow. In a similar way the streamline from Figure 6.6 is curved towards the pressure side and then deviated in the opposite direction.

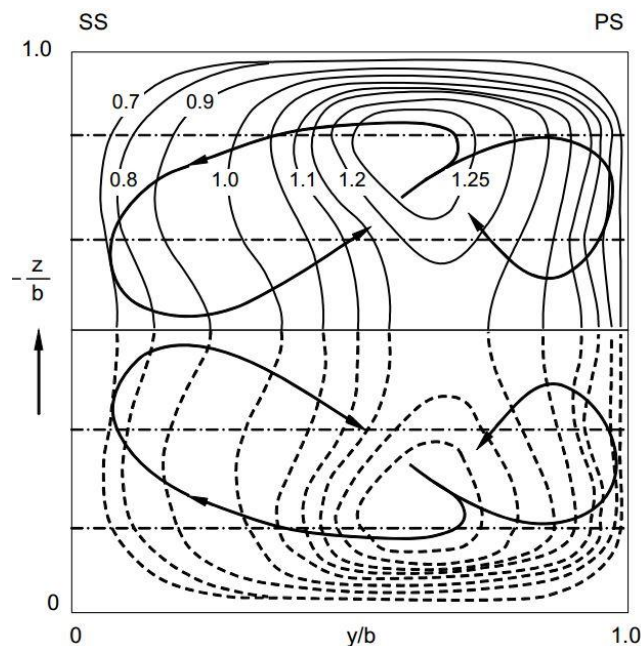


Figure 6.9: Secondary flow trajectory in a rotating channel, from [3].

The separation is therefore the results of the secondary flow created by the predominance of the Coriolis acceleration.

The mechanism, instead, leading to the removal is the following. The optimized splitters are closer to the main blade pressure side reducing the throat area and increasing the relative velocity component, w . Being b_{z3} proportional to the square of w , as follows:

$$b_{z3} = \frac{w^2}{R_{sl}}$$

the body force due to the streamline curvature balance the Coriolis effect, hence reducing the secondary flow and avoiding the flow separation.

The removal of the recirculating region is the origin of the performance improvement found for the optimized pump, however the final mechanism leading to the improved pressure rise has to be further investigated.

Figure 6.10 and Figure 6.11 show velocity streamlines at midspan and 20% span to highlight the different flow fields between baseline and optimized case. The region of separated flow can be clearly distinguished in the baseline impeller at 20% of the span. In the optimized case, instead, the flow nicely follows the blade direction. The two major vortices present in both cases towards the end of the main blade suction sides represents the region downstream of the cavity bubble shedding from the main blade leading edge. There is no change in topology between baseline and optimized impeller because the cavity size does not change as found in Section 6.1.

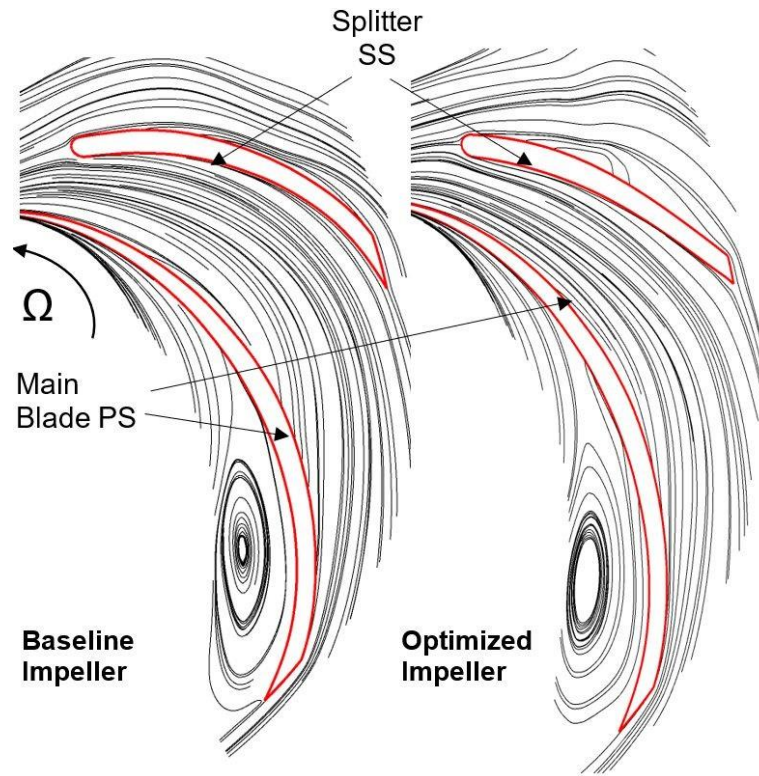


Figure 6.10: Streamlines of relative velocity at *midspan*. Between main blade pressure and splitter suction side, the reduction in flow turning is appreciable.

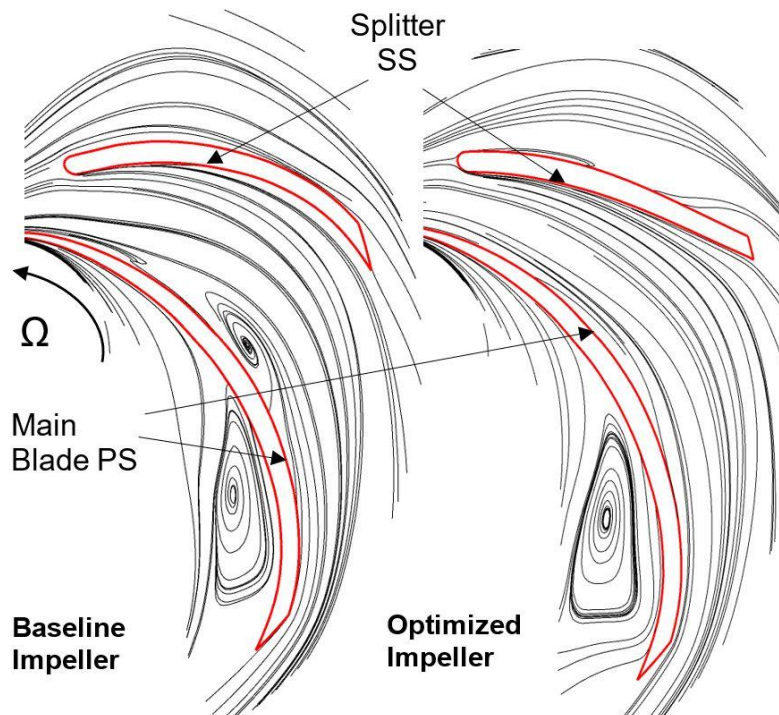


Figure 6.11: Streamlines of relative velocity at *20% span*. Separation on the pressure side of the main blade is caused by the collapse of the cavity generating from main blade suction side.

Figure 6.11 shows that the separation region causes a deviation of the streamlines from the blade geometry curvature, which is only partially recovers downstream of the region. Therefore, the separated flow reduces the blade congruency of the flow at the trailing edge. Consequently, the key contribution of the optimized splitter to the performance improvement can be expressed as the reduction of the slip $(1 - \gamma)$, or an increase of the slip factor γ . Referring to Figure 6.12 **Error! Reference source not found.** and sec. 2.1.2, ideally the velocity at the trailing edge c'_2 would follow the blade profile, having a circumferential projection equal to $c_{2\infty}$, but in real case the projection is lower and related to the ideal velocity by the following equation:

$$c_{2u\infty} - c_{2u} = (1 - \gamma)u_2$$

Therefore, ideally $\gamma = 1$ indicates blade congruent flow, while in real case $\gamma < 1$ always.

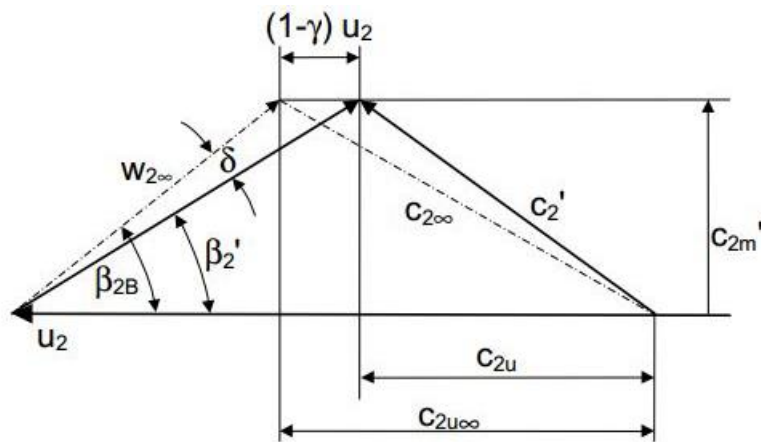


Figure 6.12: Example of velocity triangle at the impeller outlet, from [3].

The circumferential velocity component is linked to the work output, hence to the head coefficient, from the Euler's equation:

$$\rho Q (c_{2u}r_2 - c_{1u}r_1) = M + M_\tau$$

which can be modified to extract the specific work of the impeller:

$$Y_{th} = c_{2u}u_2 - c_{1u}u_1$$

By increasing c_{2u} , keeping constant all the other terms, the specific work increases. Therefore, a reduction of the slip leads to an increase of the delivered head.

Out of the ideal case, the flow within the blade passage always has a certain value of the slip factor because the streamlines at the trailing edge tend to deviate from the blade geometry. The complex equilibrium of forces acting on the flow inside the rotating blade passage, among which are the Coriolis acceleration, the centrifugal acceleration and the acceleration due to streamline curvature, creates the mechanisms leading to the slip. Gülich affirms that "with backward curved blades, the slip factor is to a large extent created in the triangular section at the impeller outlet" [3] downstream of the throat indicated with a red line in Figure 6.13. Within this region the mechanisms generating the flow deviation is the vanishing of the pressure difference between pressure and suction sides guaranteed up to that point by the blades and the consequent adaption of the streamline curvature and the velocity distributions to the free flow condition.

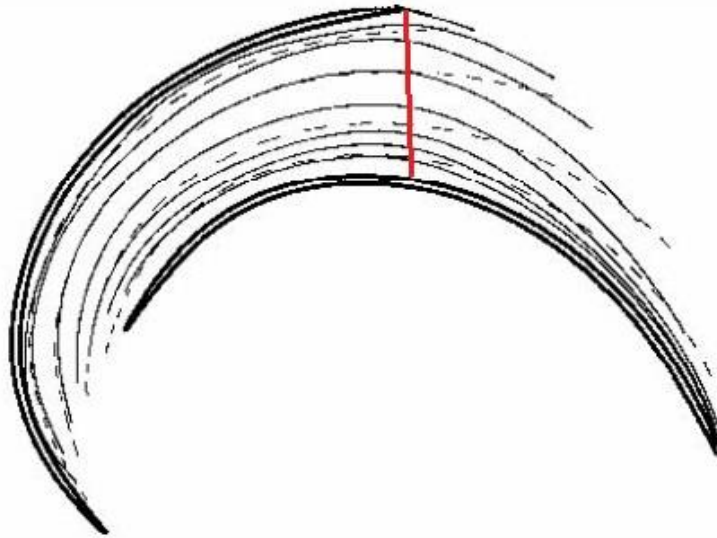


Figure 6.13: Deviation of streamlines of relative flow from the blade geometry just downstream of the throat (red line). Blade-congruent path is dashed. Figure from [3].

The previous observations lead to the conclusion that a certain degree of flow deviation from the blade geometry, or slip ($1 - \gamma$), always exists within a pump impeller and it has a direct impact on the work coefficient, through the decrease of the velocity component c_{2u} , one of the terms of the Euler's equation. Therefore, any improvement on the flow blade-congruency is an improvement on the head coefficient of the pump.

In the end, this is the effect of the optimized splitter on the pump cavitating performance, with Figure 6.14 showing the effective 5% increase of the average c_{2u} at the impeller trailing edge.

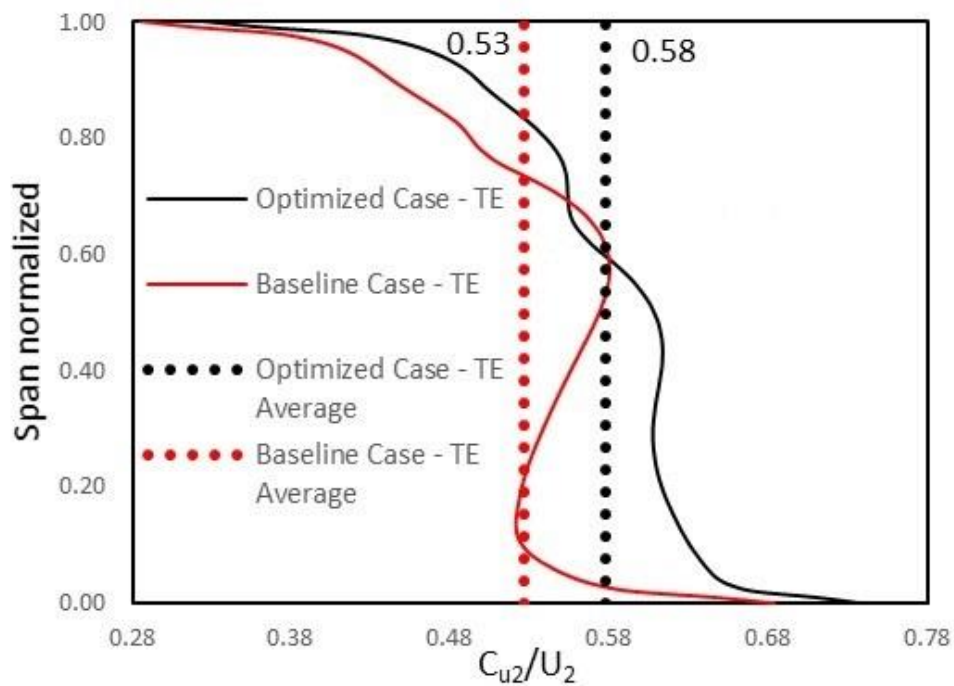


Figure 6.14: Spanwise distribution of the averaged circumferential component of the absolute velocity at the impeller trailing edge.

6.3 Influence of the blade outlet angle

In Section 5 it has been illustrated that the design change, occurred during the optimization, involves the two outlet blade angles of the splitter. In particular, both at hub and shroud, the angles are increased which, looking at the velocity triangles of Figure 6.12, can lead to an increase of the velocity component c_{2u} .

Therefore, it is necessary to check the relevance of the variation of β_{2B} compared to the removal of the flow separation, on the final performance improvement.

To do so, a 1D analysis on ideal velocities is conducted to assess the contribution of the geometry change at the splitter trailing edge. The analysis is called “1D” because it is an analytical study of velocity triangle at the trailing edge. Blade outlet angles are extracted from the CAD models of the main blade and of the optimized and baseline splitters for several span locations, namely 0%, 20%, 40%, 50%, 60%, 80% and 100% of the span. Referring to Figure 6.15, the c_{2u} component is computed with the following formula:

$$\frac{c_{2u}}{u_2} = 1 - \frac{\varphi_2}{\tan \beta_{2B}}$$

where φ_2 is computed from the CFD results of both optimized and baseline cases.

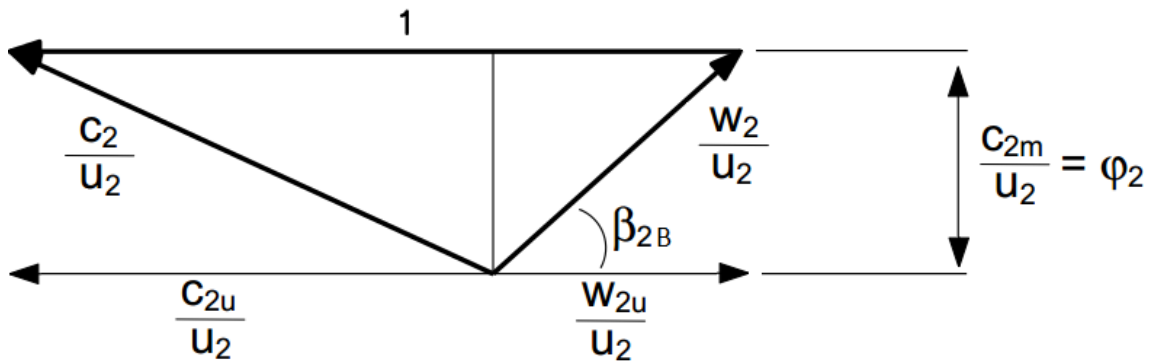


Figure 6.15: Reference configuration used for the 1D analysis.

The formula is applied at the main blade and splitter blade trailing edges, therefore for each span location two values of c_{2u} are found. An average is then computed to obtain one c_{2u} averaged value at each span location. Finally, $\overline{c_{2u}/u_2}$ is calculated to have a spanwise distribution of the velocity ratio. The same procedure is applied for both baseline and optimized geometry. In the end, two curves similar to those of Figure 6.14 are created and the averages of the two trends are computed to be compared to the data obtained from CFD.

Figure 6.16 presents the final results, with the CFD curves containing the same values of those presented in Figure 6.14 but just for the span locations investigated in the ideal 1D case. Looking at the 1D analysis curves, as expected the optimized impeller presents higher values of the ratio compared to the baseline case close to the hub where the blade angle is increased by 65.8%. At about 60% of the span the two curves overlap and stay on top of each other until around 80% of the span where the optimized impeller presents a lower ratio with respect to the baseline, a trend which is confirm up until reaching the shroud. Being the shroud blade angle of the optimized splitter increased as well, this may seem an anomaly, however it is explicable with the slightly different φ_2 between the two cases.

Focusing on the overall averages, optimized impeller shows a higher c_{2u}/u_2 ratio compared to baseline. This finding confirms the positive influence of the outlet blade angle

modification on the performance improvement. Nevertheless, comparing the overall variation of the 1D analysis with that of the CFD, it becomes clear that the geometry influence is contained. In fact, Figure 6.14 and Figure 6.16 show a 4.5% c_{2u}/u_2 increase between baseline and optimized impeller, while the contribution to be solely attributed to the outlet blade angle modifications of the optimized splitter, found by the 1D analysis, is about 0.7%. Therefore, it is possible to conclude that, excluding the effect of the blade angle increase at the trailing edge, the optimized splitter blade shape determines a 3.8% increase, Figure 6.17, of the circumferential component of the absolute velocity through the removal of a separation region close to main blade suction side which enhances the flow blade-congruency, eventually leading to a reduction of the slip ($1 - \gamma$).

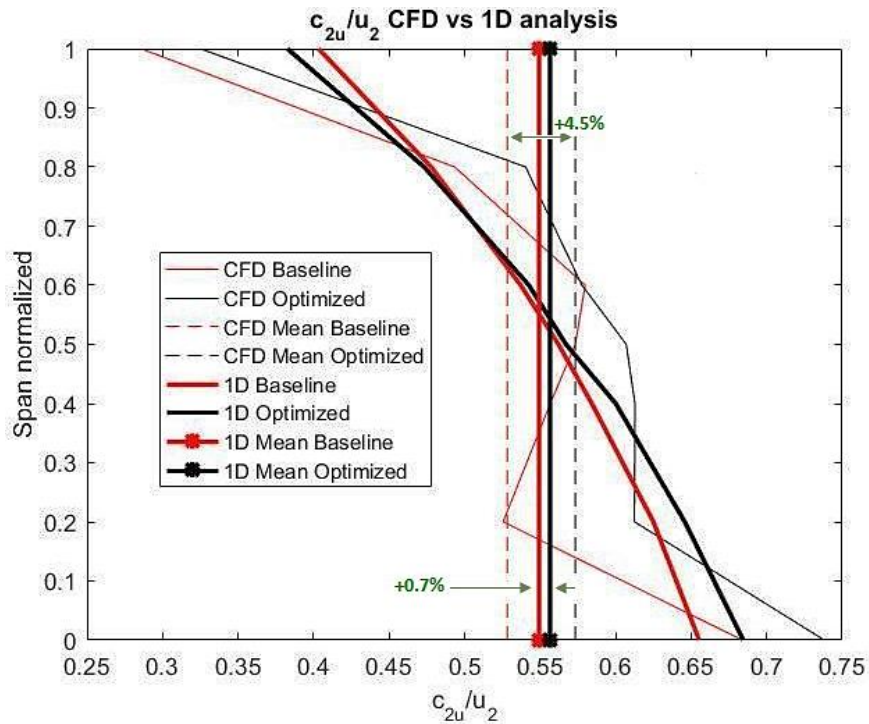


Figure 6.16: Spanwise distribution of the circumferential component of the absolute velocity. Comparison between the CFD and the 1D analysis results.

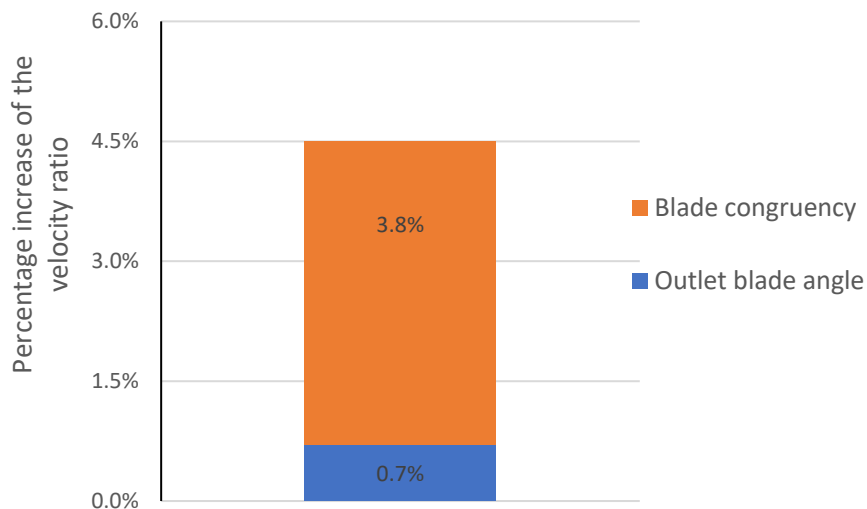


Figure 6.17: Schematic representation of the weights of the two contributions to the performance improvement

7 Conclusions and Recommendations

7.1 Conclusions

The objective of this thesis has been the development of an optimization framework for the design of splitter blades which improve the cavitating performance of the baseline pump. The framework has been validated through comparison with experimental measurements and a simple, but effective, optimization strategy has been devised to reach the objective while containing the computational costs.

The many outcomes can be summarized as follows:

- What is the gain of performance of the pump achievable with a splitter shape optimization, in terms of operative range under cavitation?

The optimum design experimentally tested yields a 4.7% extension of the operative range under cavitation while maintaining the head-capacity curve within 2% of the baseline geometry. However, the optimal splitter shape has no significant impact on cavitation. Indeed, the analysis of the flow field reveals that the optimal splitter blade shape removes flow separation close to the main blade pressure side, leading to reduced flow slip at the trailing edge. The consequent increase of c_{2u} generates the increased head rise at the optimized σ , which postpones cavitation breakdown.

- What are the most important parameters for splitter design?

This project confirms, as found in literature, that the circumferential position and the blade angle distributions are the most influencing design parameters for splitter blades. However, due to the mechanism of the performance improvement, the real impact on cavitation of those parameters could not be thoroughly assessed.

- Is the optimization framework a valuable means for splitter design?

The outcome of the thesis reveals that a framework based on design of experiments methods and surrogate-based optimization where multi-phase simulations are included, is able to identify the mutual interactions of the design parameters on the objective function, thus determining a trade-off optimal shape.

7.2 Recommendations for Future Works

Although the results of the research are promising and the optimization framework has been demonstrated to be effective, improvements can be adopted in some areas.

Starting from the geometry creation, ideally, the best way to act would be to build the pump using one of the specific tools already implemented in Workbench, e.g. Vista CPD, and then connect them with Design Modeler. The BladeGen Import Wizard, in fact, is not a versatile tool. Therefore, for other geometries it is likely that its capabilities would not be sufficient to recreate the CAD model.

Another aspect is the creation of the parameters. In case future studies will require more design freedom, the ideal solution would be to create the turbomachinery components inside BladeGen or Vista CPD, the parameters on a third part CAD software outside Workbench and then use Design Modeler as a platform to insert the geometry and the parametrization inside the optimization loop.

Moreover, the results of the optimization done within this project lead to a performance improvement which is not directly dependant of an improved cavitation condition on the impeller. Future studies should apply the optimization framework to other components of the pump which have more influence on cavitation such as the main blade leading edge region or the inducer. In this way, the effectiveness of this framework on improving the cavitating condition of a particular component could be assessed in a more precise manner and a much larger improvement of cavitating performance can be expected.

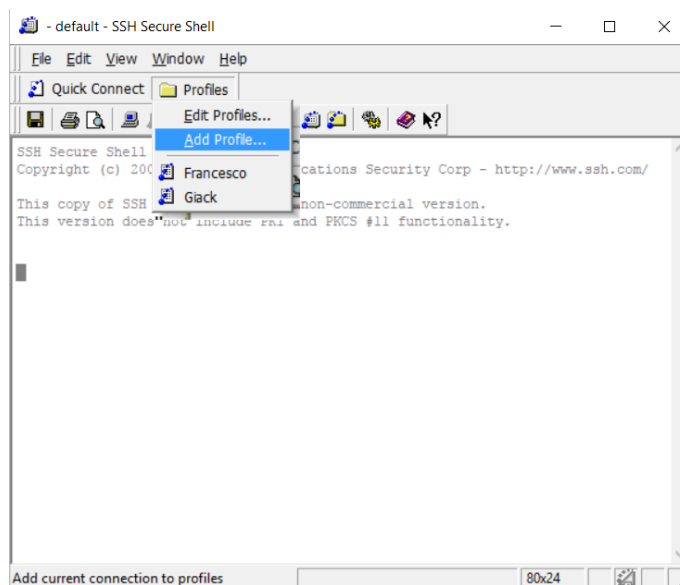
In the end, with the possibility of working with a greater computational power, some of the assumption and simplification of this project could be eliminated to further improved the precision against the experimental data.

APPENDIX – A

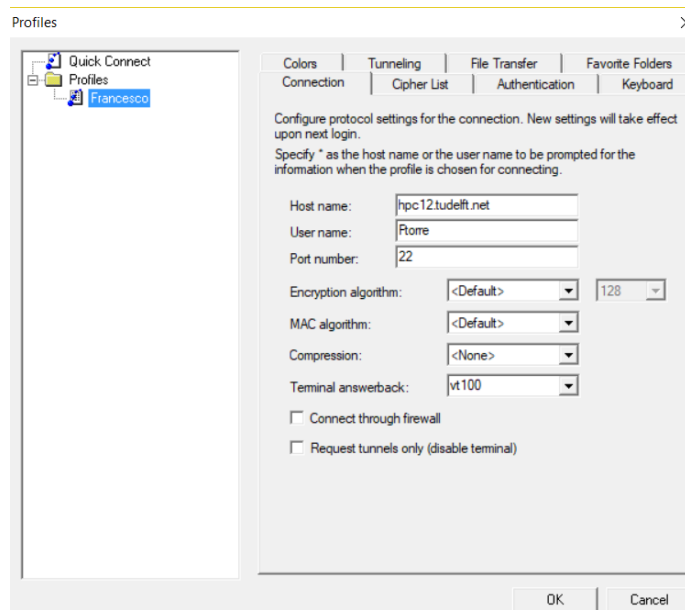
The following instructions are meant to guide a future user throughout the steps to reach a successful run of the optimization loop on the University cluster.

First step is to request an account for the cluster and to log in. There are several programs to be used for accessing the cluster, one of them is SSH Secure Shell, illustrated in the following.

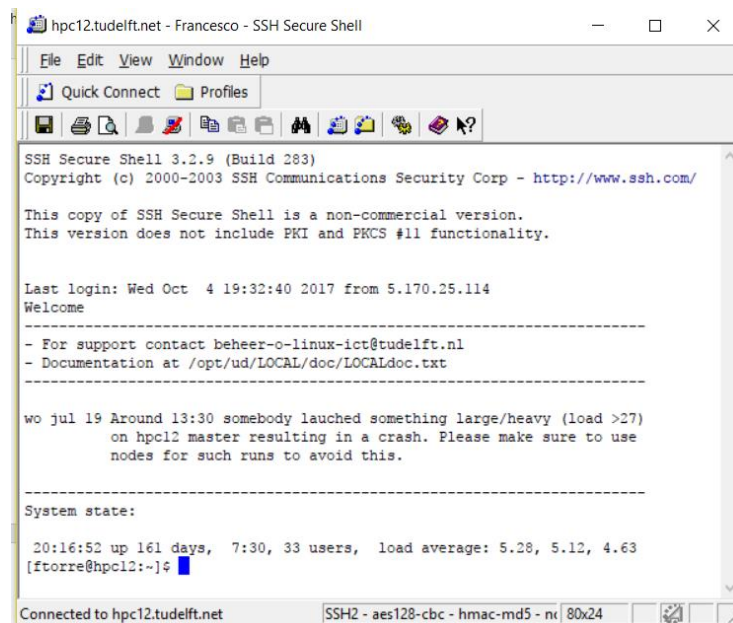
Once the account has been approved, open SSH and click on “Add Profile”.



Then, in the “Connection” tab, fill in the “Host name”, “User name” and “Port number” as presented below, obviously inserting the correct username.




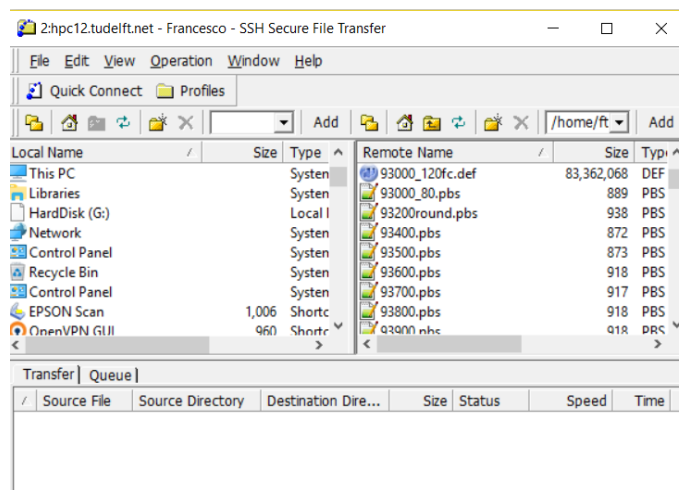
Then click on “Ok” and confirm the changes. Now it is possible to access the cluster. In the home page of SSH click on “Profile” and select the one created before (in the example “Francesco”). Insert the netID password. A window like the one below will appear.



This is the main command window of SSH. All the possible input commands are found in the cluster guide which usually is received attached to the account confirmation email. Nevertheless, the main ones are:

- LOCALnodestatus.pl* to check the status of the nodes and see which ones are available
- qstat* to see the list of the launched simulations including those in waiting to be started
- qsub filename.pbs* to launch a .pbs file (described later), hence a simulation
- qstat -u username* to check the status of the simulations launched by the user
- qdel simulationnumber* to cancel one of the simulations launched by the user, with the number being found using the “qstat” command

By clicking on  another window opens which has the local computer desktop on the left side and the user folder on the right side.



The user can upload files in the cluster by dragging them from the left to the right.

To launch a simulation is conceptually very easy. The simulation starting file and the .pbs file are basically the only two things needed. Both of them have to be uploaded in the user folder on the cluster. A .pbs file is the file containing all the information needed from the cluster to correctly start the simulation. Basically, the user has to input the number of processors he wants to use, the type of processors and the name of the starting file. There are different .pbs format depending on the program used and some examples can be found on the cluster guide. In the following the specific .pbs file for CFX and Workbench will be discussed.

After the creation of the optimization loop on Workbench, two alternatives are available for the actual execution of the simulations:

1. To load and run the entire loop on the cluster;
2. To load each single design point definition file on the cluster and download every result file.

The first option is feasible if your total simulation time for the entire loop is below the limit wall-time of the cluster (which at the moment is 36 hours) and if no use is done of any software external to Workbench (e.g. SolidWorks) or if the external software used is installed in the cluster. For the case of this thesis, it was not possible to do as such because of the wall-time constraint, therefore detailed guidelines are not included in the following about this procedure.

Nevertheless, during the first attempts, the .pbs file to run a Workbench loop on the cluster has been devised. It commands the cluster to execute the "journal.wbjn" file which is created using the recording options inside Workbench. The actions recorded inside the journal are the creation of the design points and the start of the of the project update.

An example of the journal is the following:

```
# encoding: utf-8
# Release 17.1
SetScriptVersion(Version="17.1.127")
designPoint1 = Parameters.GetDesignPoint(Name="23")
designPoint2 = Parameters.GetDesignPoint(Name="24")
designPoint3 = Parameters.GetDesignPoint(Name="25")
designPoint4 = Parameters.GetDesignPoint(Name="26")
designPoint5 = Parameters.GetDesignPoint(Name="27")
designPoint6 = Parameters.GetDesignPoint(Name="28")
designPoint7 = Parameters.GetDesignPoint(Name="29")
designPoint8 = Parameters.GetDesignPoint(Name="30")
backgroundSession1 = UpdateAllDesignPoints(DesignPoints=[designPoint1,
designPoint2, designPoint3, designPoint4, designPoint5, designPoint6, designPoint7,
designPoint8])
Save(Overwrite=True)
```

The actual .pbs file is the one which follows:

```
#!/bin/bash
# Prescribe computational resources
#PBS -l nodes=1:ppn=32:typef
# Prescribe computation name (appears in qstat)
#PBS -N simulation_name

# change the working directory
WORK_DIR="$PBS_O_WORKDIR"
cd $WORK_DIR

# load the module with the ansys software
module load ansys/17.1

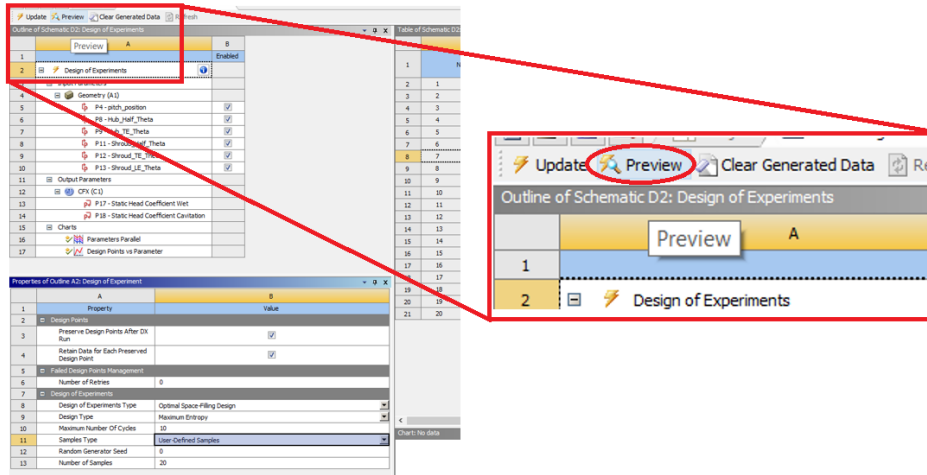
procs_per_host=32

runwb2 -R /home/username/folder_containing_the_journal/journal.wbjn -B -F
/home/username/WorkbenchProject.wbpj
```

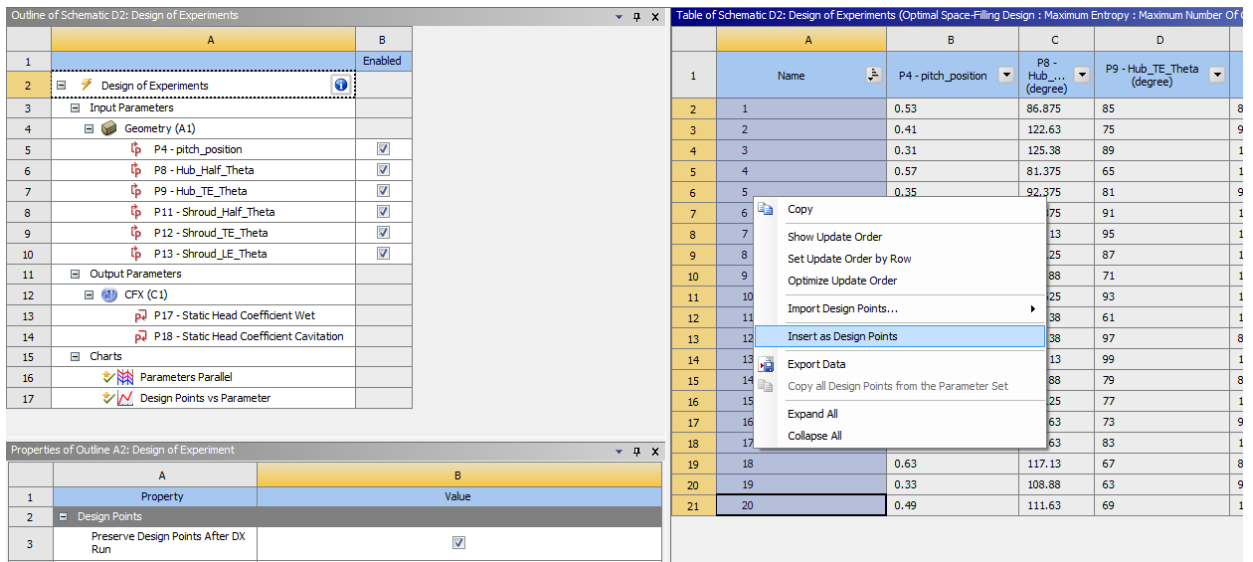
Going back to the numbered list, the second case is the one occurred for the present work. The manual run of each single design point makes it possible to complete the Workbench loop even if the cluster wall-time is not enough or some external software has to be used. In fact, the CFX input files are created locally, then uploaded and computed on the cluster and the results downloaded and analyzed again locally. After the extraction of the output parameters, the Workbench loop can be recreated by “artificially” adding the simulation outcomes in the Optimizer tab.

Therefore, the first step is to create the .def file with CFX pre. To create the .def file do as follows:

- 1) In the “Design of Experiments” tab, select the type of Design of Experiments and then click on “Preview” on the top-left side:



2) The created Design Points will appear on the right. Select all of them and right click, then choose “Insert as Design Points”:



3) All the Design Points are now visible inside the “Parameters Manager” tab. First, click on “Retain”:

	A	B	C	D	E	F	G	H	I	J	K
1	Name	P4	P8	P9	P11	P12	P13	P...	P18 -	<input checked="" type="checkbox"/> Ret...	Retained Data
2	Units		d...	d...	d...	de...	de...				
3	DP 0 (Current)	0.5	101.93	75.977	102.94	76.154	130.05	⚡	⚡	<input checked="" type="checkbox"/>	⚡
4	DP 22	0.4746	89.803	78.676	95.065	76.068	124.1	⚡	⚡	<input checked="" type="checkbox"/>	⚡
5	DP 23	0.53	86.875	85	83.75	74.625	130.63	⚡	⚡	<input checked="" type="checkbox"/>	⚡
6	DP 24	0.41	122.63	75	98.75	96.075	102.63	⚡	⚡	<input checked="" type="checkbox"/>	⚡
7	DP 25	0.31	125.38	89	121.25	76.575	114.88	⚡	⚡	<input checked="" type="checkbox"/>	⚡
8	DP 26	0.57	81.375	65	103.75	90.225	113.13	⚡	⚡	<input checked="" type="checkbox"/>	⚡
9	DP 27	0.35	92.375	81	91.25	72.675	104.38	⚡	⚡	<input checked="" type="checkbox"/>	⚡
10	DP 28	0.69	97.875	91	118.75	84.375	127.13	⚡	⚡	<input checked="" type="checkbox"/>	⚡
11	DP 29	0.47	128.13	95	101.25	88.275	132.38	⚡	⚡	<input checked="" type="checkbox"/>	⚡
12	DP 30	0.55	95.125	87	126.25	80.475	100.88	⚡	⚡	<input checked="" type="checkbox"/>	⚡
13	DP 31	0.59	119.88	71	111.25	64.875	134.13	⚡	⚡	<input checked="" type="checkbox"/>	⚡
14	DP 32	0.37	89.625	93	106.25	98.025	120.13	⚡	⚡	<input checked="" type="checkbox"/>	⚡
15	DP 33	0.43	114.38	61	116.25	66.825	106.13	⚡	⚡	<input checked="" type="checkbox"/>	⚡
16	DP 34	0.61	103.38	97	86.25	86.325	107.88	⚡	⚡	<input checked="" type="checkbox"/>	⚡
17	DP 35	0.51	106.13	99	108.75	60.975	118.38	⚡	⚡	<input checked="" type="checkbox"/>	⚡
18	DP 36	0.45	130.88	79	81.25	68.775	116.63	⚡	⚡	<input checked="" type="checkbox"/>	⚡
19	DP 37	0.39	84.125	77	123.75	70.725	125.38	⚡	⚡	<input checked="" type="checkbox"/>	⚡

Chart: No data

4) Now that all of them are selected to be “Retained Data”, when right-clicking on each of them, the option “Set as Current” is available:

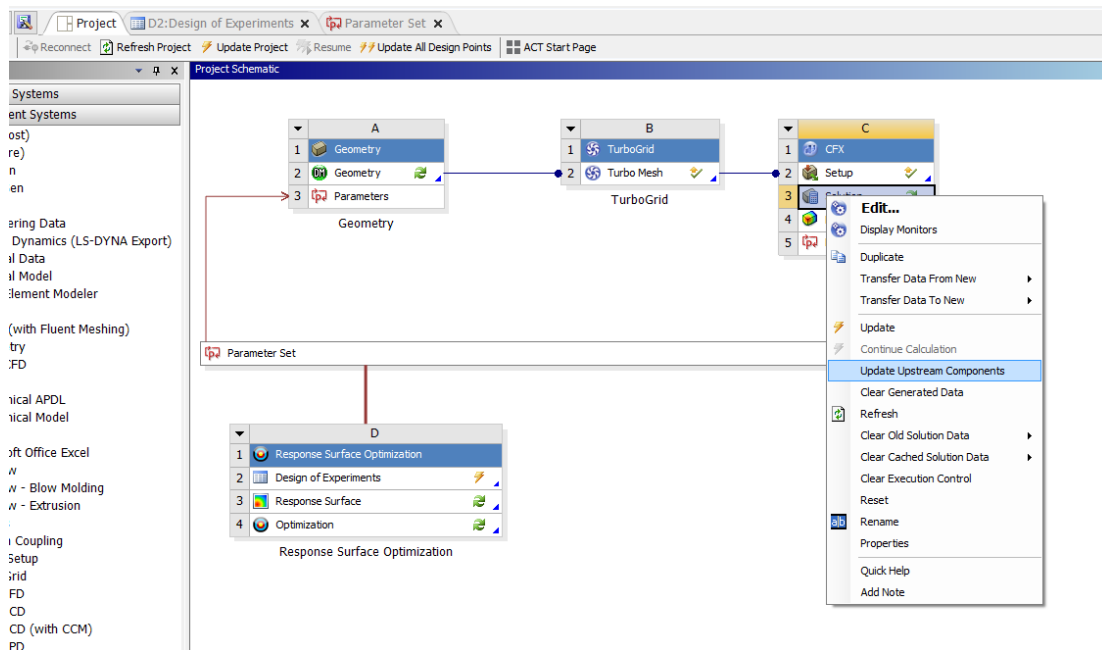
Table of Design Points											
	A	B	C	D	E	F	G	H	I	J	K
1	Name	P4	P8	P9	P11	P12	P13	P...	P18 -	<input checked="" type="checkbox"/> Ret...	Retained Data
2	Units		d...	d...	d...	de...	de...				
3	DP 0 (Current)	0.5	101.93	75.977	102.94	76.154	130.05	⚡	⚡	<input checked="" type="checkbox"/>	⚡
4	DP 22	0.4746	89.803	78.676	95.065	76.068	124.1	⚡	⚡	<input checked="" type="checkbox"/>	⚡
5	DP 23	0.53	86.875	85	83.75	74.625	130.63	⚡	⚡	<input checked="" type="checkbox"/>	⚡
6	DP 24	0.41	122.63	75	98.75	96.075	102.63	⚡	⚡	<input checked="" type="checkbox"/>	⚡
7	DP 25	0.31	125.38	89	121.25	76.575	114.88	⚡	⚡	<input checked="" type="checkbox"/>	⚡
8	DP 26	0.57	81.375	65	103.75	90.225	113.13	⚡	⚡	<input checked="" type="checkbox"/>	⚡
9	DP 27	0.35	92.375	81	91.25	72.675	104.38	⚡	⚡	<input checked="" type="checkbox"/>	⚡
10	DP 28	0.69	97.875	91	118.75	84.375	127.13	⚡	⚡	<input checked="" type="checkbox"/>	⚡
11	DP 29	0.47	128.13	95	101.25	88.275	132.38	⚡	⚡	<input checked="" type="checkbox"/>	⚡
12	DP 30	0.55	95.125	87	126.25	80.475	100.88	⚡	⚡	<input checked="" type="checkbox"/>	⚡
13	DP 31	0.59	119.88	71	111.25	64.875	134.13	⚡	⚡	<input checked="" type="checkbox"/>	⚡
14	DP 32	0.37	89.625	93	106.25	98.025	120.13	⚡	⚡	<input checked="" type="checkbox"/>	⚡
15	DP 33	0.43	114.38	61	116.25	66.825	106.13	⚡	⚡	<input checked="" type="checkbox"/>	⚡
16	DP 34	0.61	103.38	97	86.25	86.325	107.88	⚡	⚡	<input checked="" type="checkbox"/>	⚡
17	DP 35	0.51	106.13	99	108.75	60.975	118.38	⚡	⚡	<input checked="" type="checkbox"/>	⚡
18	DP 36	0.45	130.88	79	81.25	68.775	116.63	⚡	⚡	<input checked="" type="checkbox"/>	⚡
19	DP 37	0.39	84.125	77	123.75	70.725	125.38	⚡	⚡	<input checked="" type="checkbox"/>	⚡

Context menu for DP 23:

- Copy
- Show Update Order
- Set Update Order by Row
- Optimize Update Order
- Delete Design Point
- Set as Current**
- Copy inputs to Current
- Duplicate Design Point
- Export Selected Design Points
- Update Selected Design Points
- Export Data
- Copy Design Points to

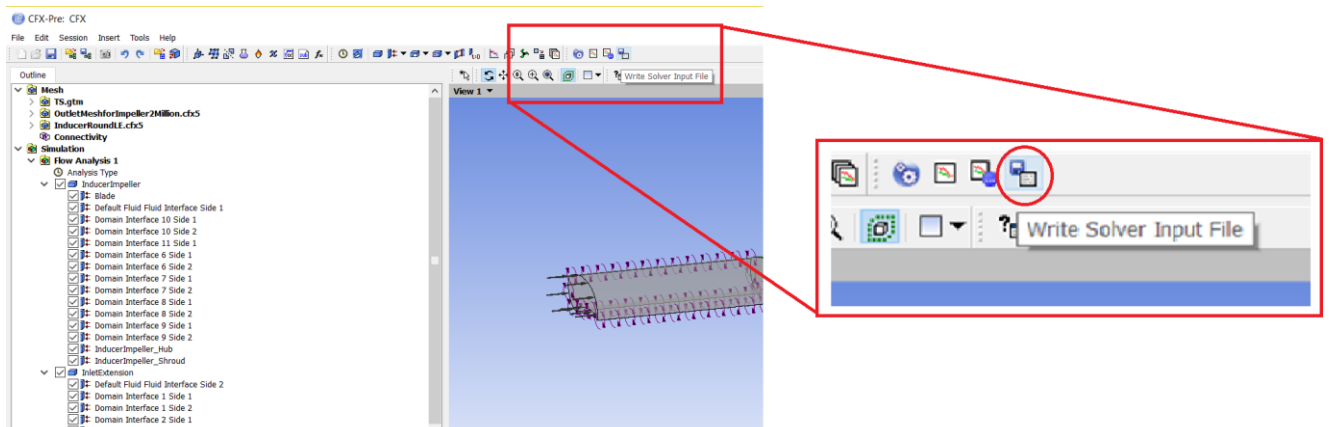
From this step on, the same procedure has to be repeated for each Design Points. Click on “Set as Current” and wait until the program finishes loading.

5) Go in “Project”, select the CFX-Solver tab, right-click on it and choose “Update Upstream Components”. The geometry, mesh and CFX settings will be uploaded.



6) When Workbench stops updating, the main project folder will contain a sub-folder named after the updated design point and inside it a sub-folder called “CFX” which contains another folder called “CFX”. Inside this last one, a CFX.cfx file will be present.

7) Open CFX-Pre as external from Workbench and read the CFX.cfx of before. Because it is opened outside Workbench, the option “Write solver input file” is available. Select it and save the file where desired.



8) Upload the .def file on the cluster.

After having uploaded it on the cluster, the .pbs file can be written as follows:

```
#!/bin/bash
```

```

# Prescribe computational resources
#PBS -l nodes=1:ppn=32:typeg
# Prescribe computation name (appears in qstat)
#PBS -N cand3compopt

# define the location of the definitions file
DEF=/home/username/directory_of_DEF_file_on_cluster/filename.def
# define the location of the initialization file
# (leave empty [also no spaces] when not specified)
INI=

cd $PBS_O_WORKDIR

# load the module with the ansys software
module load ansys/17.1

# get list of processors
PAR=$(sed -e '{:q;N;s/^\n/,/g;t q}' ${PBS_NODEFILE})

# Choose the correct startup sequence
if [ "X${INI}" = "X" ]
then
  echo "cfx5solve -batch -def ${DEF} -par-dist ${PAR}"
  cfx5solve -batch -def ${DEF} -par-dist ${PAR}
else
  echo "cfx5solve -batch -def ${DEF} -ini ${INI} -par-dist ${PAR}"
  cfx5solve -batch -def ${DEF} -cont-from-file ${INI} -par-dist ${PAR}
fi

```

where the type (*typeg*) and number of processors (*ppn*) have to be selected accordingly to the availability of the cluster. To launch the simulation, just use the command *qsub* explained before, followed by the name of the .pbs file.

Once the .res files are downloaded, the output parameters can be extracted. At the end of the process, to make Workbench understand the results of the optimization, the design points need to be collected all together in one file containing input and output parameters following a specific grammar. The file has to have the .csv format and has to look like the following one:

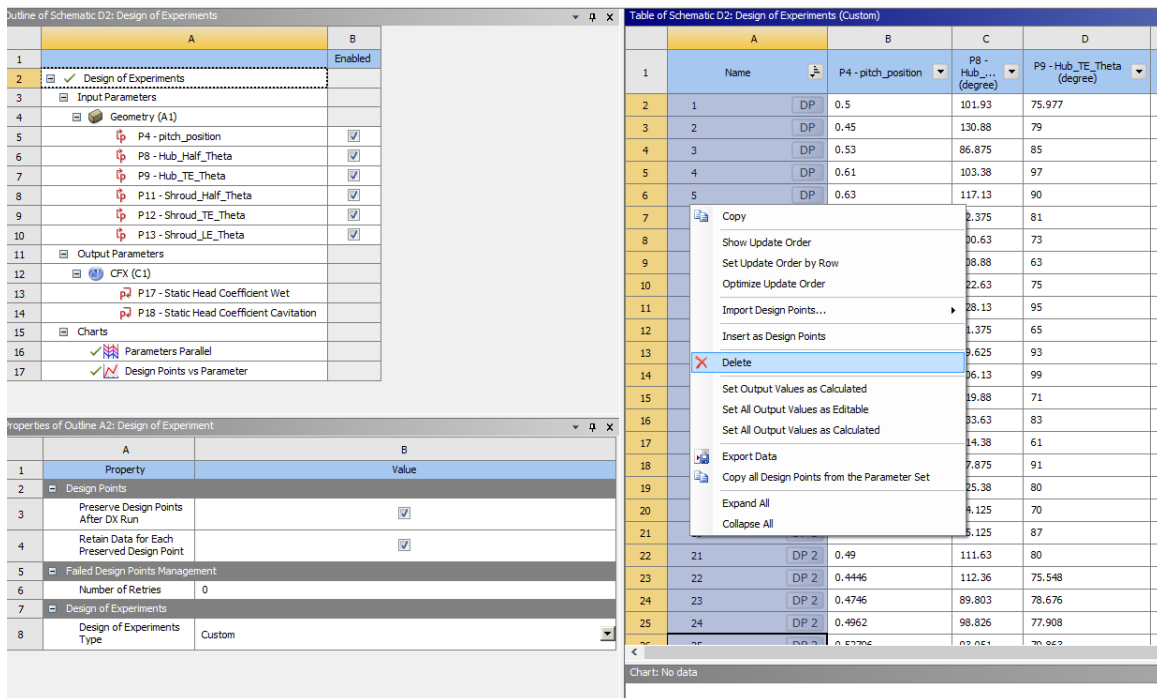
```
Name,P4,P8,P9,P11,P12,P13,P17,P18
```

DP 1,0.50,101.934,75.976789,102.94254,76.154462,130.04786,0.387117,0.3629
 DP 2,0.45,130.875,79,81.25,66.75,116.625,0.362092,0.359289
 DP 3,0.53,86.875,85,83.75,71.25,130.625,0.402829,0.368915
 DP 4,0.61,103.375,97,86.25,80.25,107.875,0.378151,0.354073
 DP 5,0.63,117.125,90,88.75,84.75,123.625,0.397137,0.350614
 DP 6,0.35,92.375,81,91.25,69.75,125,0.365667,0.358868

.
 .
 .

where “P4”, “P8” etc. are the codes automatically given by Workbench to the input and output parameters.

With the .csv file being created, open the Design of Experiments tab in the Workbench Project, select the “Custom” Design of Experiments Type, select on the right all the design points and delete them:



Then right-click on the blank entry which appears in place of the deleted design points and select the .csv from “Import Design Points”. If the .csv file has been written correctly, the freshly computed design points will appear showing also the output parameters. From there, all the subsequent optimization steps can be done, including refining points which will just be extra-single simulations on the cluster and relative updates of the .csv file.

Outline of Schematic D2: Design of Experiments

	A	B
1		Enabled
2	Design of Experiments	
3	Input Parameters	
4	Geometry (A1)	
5	P4 - pitch_position	<input checked="" type="checkbox"/>
6	P8 - Hub_Half_Theta	<input checked="" type="checkbox"/>
7	P9 - Hub_TE_Theta	<input checked="" type="checkbox"/>
8	P11 - Shroud_Half_Theta	<input checked="" type="checkbox"/>
9	P12 - Shroud_TE_Theta	<input checked="" type="checkbox"/>
10	P13 - Shroud_LE_Theta	<input checked="" type="checkbox"/>
11	Output Parameters	
12	CFX (C1)	
13	P17 - Static Head Coefficient Wet	
14	P18 - Static Head Coefficient Cavitation	
15	Charts	
16	Parameters Parallel	<input checked="" type="checkbox"/>
17	Design Points vs Parameter	<input checked="" type="checkbox"/>

Properties of Outline A2: Design of Experiment

	A	B
1	Property	Value
2	Design Points	
3	Preserve Design Points After DX Run	<input checked="" type="checkbox"/>
4	Retain Data for Each Preserved Design Point	<input checked="" type="checkbox"/>
5	Failed Design Points Management	
6	Number of Retries	0
7	Design of Experiments	
8	Design of Experiments Type	Custom

Table of Schematic D2: Design of Experiments (Custom)

	A	B	C	D	E
1	Name	P4 - pitch_position	P8 - Hub,... (degree)	P9 - Hub_TE_Theta (degree)	P11 - Shroud_Half_Theta (degree)

New Design Point

- Copy
- Show Update Order
- Import Design Points...
 - Browse...
 - 1 G:\...\DesignPointLog_Opt5_Step1.csv
 - 2 F:\Opt7\DesignPointLog_Op17.csv
 - 3 F:\Opt8\DesignPointLog_Op18.csv
 - 4 G:\...\DesignPointLog_Opt5.csv
- Set All Output Values as Editable
- Set All Output Values as Calculated
- Copy all Design Points from the Parameter Set
- Expand All
- Collapse All

Bibliography

- [1] H. Mårtensson, S. Andersson, S. Trollheden and S. Brodin, "Rocket Engines: Turbomachinery," NATO - Science and Technology Organization , 2007.
- [2] C. Brennen, "Hydrodynamics of Pumps", Oxford: Concepts ETI Inc. and Oxford University Press, 1994.
- [3] J. Gülich, "Centrifugal Pumps", Springer-Verlag Berlin Heidelberg 2008, 2010. Second Edition.
- [4] H. Chen, X. Huang, K. Shi and al., "A Computational Fluid Dynamics Study of Circumferential Groove Casing Treatment in a Transonic Axial Compressor," *ASME, Journal of Turbomachinery*, vol. 138, no. 5, 2013.
- [5] D. Japikse, W. D. Marscher and R. B. Furst, "Centrifugal Pump Design and Performance", White River Junction, Vermont: Concepts NREC, 2006.
- [6] R. B. Furst, "Liquid rocket engine centrifugal flow turbopumps," NASA SP-8109, NTIS N74-28961, 1973.
- [7] J. Onoue, A. Okamoto, M. Hayakawa and Y. Kawata, "Improvement of suction performance of general industrial centrifugal pump," in *AICFM The 13th Asian International Conference on Fluid Machinery*, Tokyo, 7th-10th September 2015.
- [8] Y. L. Zhang, S. Q. Yuan, J. F. Zhang, Y. N. Feng and J. X. Lu, "Numerical investigation of the effects of splitterblades on the cavitation performance of a centrifugal pump," in *IOP Conference Series: Earth and Environmental Science v22*, 2014.
- [9] W. Yang, R. Xiao, F. Wang and Y. Wu, "Influence of Splitter Blades on the Cavitation Performance of a Double Suction Centrifugal Pump," *Advances in Mechanical Engineering*, vol. V2014, 2014.
- [10] M. Gölcü and Y. Pancar, "Investigation of performance characteristics in a pump impeller with low blade discharge angle," *World Pumps*, vol. 2005, no. 468, pp. 32-40, 2005.
- [11] M. Gölcü, Y. Pancar and Y. Sekmen, "Energy saving in a deep well pump with splitter blade," *Energy Conversion and Management*, vol. 47, no. 5, pp. 638-651, 2005.
- [12] M. Gölcü, N. Usta and Y. Pancar, "Effects of splitter blades on deep well pump performance," *Journal of Energy Resources Technology*, vol. 129, no. 3, pp. 169-176, 2007.
- [13] B. L. Cui, Z. C. Zhu, J. C. Zhang and Y. Chen, "Flow simulation and experimental study of low-specific-speed high-speed complex centrifugal impellers," *Chinese Journal of Chemical Engineering*, vol. 14, no. 4, pp. 435-441, 2006.
- [14] B. Cui, Y. Lin and Y. Jin, "Numerical simulation of flow in centrifugal pump with complex impeller," *Journal of Thermal Science*, vol. 20, no. 1, pp. 47-52, 2011.
- [15] H. Chen, W. Liu and W. Jian, "Impellers of low specific speed centrifugal pump based on the draughting technology," in *25th IAHR Symposium on Hydraulic Machinery and Systems*, Timisoara, Romania, 20th–24th September 2010.
- [16] G. Kergourlay, M. Younsi, F. Bakir and R. Rey, "Influence of splitter blades on the flow field of a centrifugal pump: Test-analysis comparison," *International Journal of Rotating Machinery*, 2007.
- [17] G. Cavazzini, G. Pavesi, A. Santolin, G. Ardizzon and R. Lorenzi, "Using splitter blades to improve suction performance of centrifugal impeller pumps," *Proceedings*

of the Institution of Mechanical Engineers Part A: Journal of Power and Energy, vol. 229, no. 3, p. 309–332, 2015.

- [18] H. Miyamoto, Y. Nakashima and H. Ohba, "Effects of splitter blades on the flows and characteristics in centrifugal impellers," *JSME Int J, Ser. 2: Fluid Eng. Heat Transfer Power Combustion Thermo Physical Properties*, vol. 32(2), pp. 238-246, 1992.
- [19] M. Gölcü, "Artificial neural network based modeling of performance characteristics of deep well pumps with splitter blades," *Energy Conversion and Management*, vol. 47, no. 18-19, pp. 3333-3343, 2006.
- [20] C. Clark, G. Pullan, E. Curtis and F. Goenaga, "Secondary Flow Control in Low Aspect Ratio Vanes Using Splitters," *ASME Turbo Expo: Power for Land, Sea, and Air, Volume 2B: Turbomachinery*, 2016.
- [21] Y. Kawata, "Cooperative Research in Turbomachinery - Collaboration between OIT and TUDelft," Seminar at the Embassy of Netherlands in Tokyo, 2016.
- [22] Ansys Academic Research, Theory Manual, vol. Release 17.1, Canonsburg, PA: ANSYS, Inc., 2011.
- [23] A. Giunta, S. Wojtkiewicz and M. Eldred, "Overview of Modern Design of Experiments Methods for Computational Simulations," in *Aerospace Sciences Meetings*, 41st Aerospace Sciences Meeting and Exhibit.
- [24] M. R. Facer and H. G. Muller, "Nonparametric estimation of the location of a maximum in a response surface," *Journal of Multivariate Analysis*, vol. 87, pp. 191-217, 2003.
- [25] C. M. Anderson-Cook and K. Prewit, "Some Guidelines For Using Nonparametric Methods For Modeling Data From Response Surface Designs," *Journal of Modern Applied Statistical Methods*, vol. 4, no. 1, pp. 106-119, 2005.
- [26] K. Ashihara and A. Goto, "Study on pump impeller with splitter blades designed by 3-D inverse design method," in *Proceedings of the ASME fluids engineering division*, 2000.
- [27] K. Juckelandt, S. Bleeck and F.-H. Wurm, "ANALYSIS OF LOSSES IN CENTRIFUGAL PUMPS WITH LOW SPECIFIC SPEED WITH SMOOTH AND ROUGH WALLS," in *11th European Conference on Turbomachinery Fluid dynamics & Thermodynamics*, Madrid, Spain, 2015.